CHALMERS
UNIVERSITY OF TECHNOLOGY

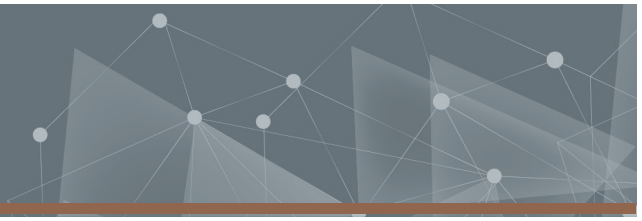

Design and Optimization of a Subsea Drive System with a Long step-out

Master's thesis in Master Programme MPEPO

Anton Apelberg & Tom Ekman

DEPARTMENT OF ELECTRICAL POWER ENGINEERING
CHALMERS UNIVERSITY OF TECHNOLOGY
Gothenburg, Sweden 2025
www.chalmers.se

Master's thesis 2025

Design and Optimization of a Subsea Drive System with a Long Step-out

Anton Apelberg
Tom Ekman

CHALMERS
UNIVERSITY OF TECHNOLOGY

Department of Electrical Power Engineering
Division of Electric Power Systems
Chalmers University of Technology
Gothenburg, Sweden 2025

Design and Optimization of a Subsea Drive System with a Long Step-out
Anton Apelberg, Tom Ekman

Supervisor: Dimitrios Stellas, Senior Electrical Engineer
Examiner: Peiyuan Chen, Department of Electric Power Engineering

Master's Thesis 2025
Department of Electrical Power Engineering
Division of Electrical Power Systems
Chalmers University of Technology
SE-412 96 Gothenburg
Telephone +46 31 772 1000

Typeset in LaTeX
Gothenburg, Sweden 2025

Design and Optimization of a Subsea Drive System with a Long Step-out
Anton Apelberg, Tom Ekman
Department of Electrical Power Engineering
Chalmers University of Technology

Abstract

Subsea power transmission systems are essential for enabling offshore oil and gas operations, particularly as exploration extends into ultra-deep waters requiring long-distance electrical supply. The increasing demand for reliable and efficient subsea drive systems over extended cable lengths introduces several electrical and control challenges, including voltage drop, power losses, resonance effects, and harmonic distortion.

This thesis develops a comprehensive model of a 150 km subsea AC transmission system using DIgSILENT PowerFactory to analyze steady-state voltage stability, power quality, and dynamic system behavior. The results demonstrate that proper cable sizing and reactive power compensation are crucial for maintaining voltage regulation along the transmission path. An open-loop scalar control strategy is applied to drive an induction motor, successfully achieving the desired steady-state speeds. However, transient oscillations observed during step frequency changes indicate the need for damping or filtering to improve dynamic response.

A sinusoidal pulse width modulation (SPWM) technique is integrated into the inverter model, resulting in balanced, sinusoidal current waveforms at the motor terminals and stable performance during steady-state operation. While some distortion remains at the inverter output, the long subsea cable provides a natural filtering effect before reaching downstream components.

In conclusion, the study confirms that a 150 km subsea AC drive system is technically feasible when supported by appropriate component selection, control design, and harmonic filtering. The findings underscore the importance of coordinated system optimization in achieving reliable and stable long-distance subsea power delivery.

Acknowledgments

We would like to express our most sincere gratitude to the company for granting us the opportunity to explore such a interesting topic. Furthermore, we extend our deepest appreciation to our company supervisors, Dimitrios Stellas and Kristiansen Baricuatro, for their support and guidance throughout the course of this thesis.

Additionally, we would like to express our heartfelt gratitude to our examiner, Peiyuan Chen, Docent in Electronics at the Electric Power Engineering Department of Chalmers University of Technology, for overseeing this MSc thesis. His expertise, guidance, and encouragement proved to be invaluable throughout the research and writing process.

We are also deeply grateful to Magnus Almgren, Principal Engineer at the company, for sharing his expertise on induction motors and for his active interest in the research presented in this thesis.

We extend our thanks to Anton Riström, Engineering Manager, and Andre Kristiansen, Technology Manager in Electric Power Systems at the company, for their commitment and assistance in making this thesis project possible.

Anton Apelberg
Tom Ekman
Göteborg, May 2025

Contents

List of Figures

List of Tables

1 Introduction

Subsea oil and gas operations in ultra-deep waters requires advanced power transmission systems capable of efficiently delivering energy over long distances. This background explores the challenges associated with long step-outs and the importance of accurate modeling to optimize power delivery, minimize losses, and ensure system stability.

1.1 Background

Oil and gas exploration is progressively shifting to more extreme environments, such as ultra-deep water, posing significant challenges for the industry [1]. As exploration ventures into deeper waters and requires longer cable distances, the demand for higher motor performances increases, leading to greater energy consumption and less stability [2]. A fundamental approach to addressing these challenges is through accurate modeling of long step-outs. By simulating the electrical behavior of subsea power transmission, it is possible to optimize system parameters such as voltage levels, cable design, and transformer configurations to enhance efficiency and stability. In this thesis, a model for a 150 km long step-out will be created. In power systems, step-up transformers are used to raise the voltage over long transmission cables, minimizing losses during transmission. Step-down transformers are then used to reduce the voltage to an appropriate level for the motor, ensuring safe and efficient operation [3]. A figure of a generic subsea electric drive system is shown in figure 1 below.

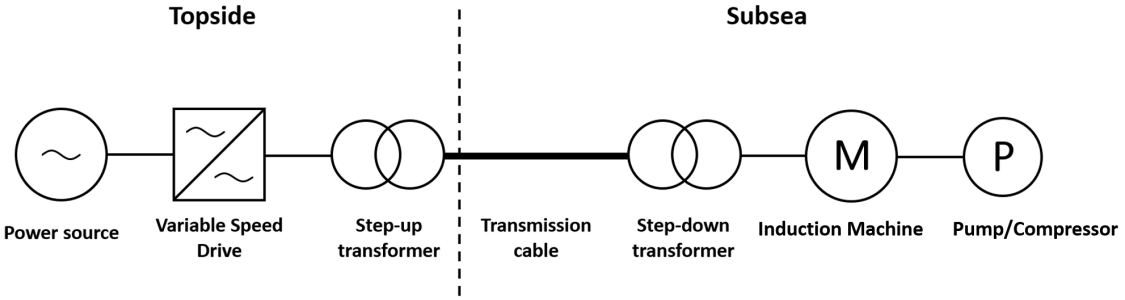

Figure 1: Subsea electric drive system

Induction machines play a big role in subsea technology due to their reliability, robustness, and minimal maintenance needs. They are commonly used in subsea pumps and compressors driving key equipment for oil and gas operations [4]. Their ability to operate efficiently under variable speed conditions, particularly with variable speed drives (VSDs), ensures precise control of speed and torque, optimizing performance under varying loads.

The rugged design of induction motors allows them to endure the extreme pressures and temperatures in deep-water environments [5]. However, as subsea installations extend to longer step-out distances, efficient power transmission becomes a critical challenge. Voltage drops, power losses, and system stability must be carefully analyzed to ensure reliable operation over extended cable lengths.

Long step-outs introduce significant electrical challenges, primarily due to increased cable impedance and capacitive effects, which can lead to voltage instability and transmission losses [6]. Ensuring stable power delivery requires a thorough understanding of how these factors influence the system and how they can be mitigated through proper transformer configurations, reactive compensation, and voltage control strategies.

To address these challenges, modeling long step-out systems is essential for predicting performance and optimizing system design. By simulating power transmission over extended distances, it is possible to develop strategies that minimize losses, improve voltage regulation, and enhance overall system reliability. This thesis aims to develop a model that accurately represents these conditions, providing insights into the optimal design of subsea power systems for long-distance energy transmission.

1.2 Aim

This master's thesis aims to develop a detailed model for analyzing power transmission in long step-out subsea systems. By utilizing DIgSILENT PowerFactory, the project investigates the impact of extended cable lengths and cross-sectional area on system performance and stability. The objective is to provide insights into the electrical behavior of long step-outs and identify strategies to mitigate voltage drops, transmission losses, and instability. The findings will contribute to the optimization of subsea power transmission, ensuring reliable and efficient energy delivery over long distances.

1.3 Scope

This thesis investigates the challenges and limitations associated with power transmission in long step-out subsea systems. The following research questions guide the research:

- How do varying cross-sectional areas impact system performance, stability, and power quality in long step-out subsea power transmission?
- What speed control strategy can be implemented to ensure the motor reaches and maintains the desired operating points of a subsea pump under varying loads?
- What mitigation strategies, such as reactive power compensation, can be implemented to improve power delivery efficiency and system stability in long step-out subsea systems?

Additionally, the work aims to validate the hypothesis that optimized modeling and system design can enhance the reliability of long step-out power transmission. These questions will be analyzed and tested through modeling and simulation in DIgSILENT PowerFactory, providing insights into best practices for designing robust subsea power systems.

1.4 Limitations

This thesis focuses on modeling power transmission over longer cable distances, specifically up to 150 km. However, certain aspects are beyond the scope of this study. The study does not consider insulation design or material selection for the transmission system components, as the focus remains on system performance analysis rather than component-level design. Economic considerations, including cost analysis, are excluded due to limited data availability and the technical nature of this study, which prioritizes electrical performance and system behavior.

2 System Description

This theory section outlines the key components and principles relevant to the subsea power system, including the induction machine, power transmission elements, and the variable speed drive. It also covers cable phenomena and compensation methods needed for stable and efficient operation.

2.1 Induction Machine

The induction machine (IM) is an AC electric motor commonly used in industrial drive applications. It consists of two primary components, the stationary stator and the rotating rotor. The stator houses three-phase windings that receive power from the external supply [7]. In contrast, the rotor is the rotating element and contains either a series of single-bar conductors or windings embedded in slots. These slots feature narrow openings at the rotor's surface, which serve to secure the conductors in place. A visual example of an induction machine is shown in below Figure 2 [8].

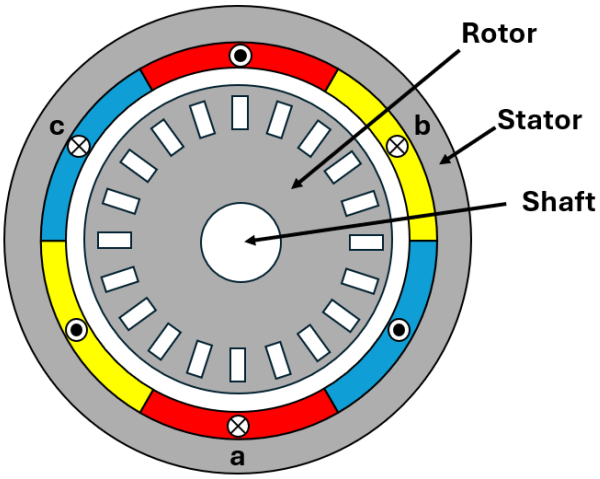

Figure 2: Induction machine three-phase stator coil and rotor on the left and three-phase voltages on the right

The three-phase stator windings produces a rotating field of constant magnitude, which rotates at the speed corresponding to the frequency at the supply and the number of poles in the motor as per Equation 2.1 below.

$$n_{sync} = \frac{120 \cdot f}{p} \tag{2.1}$$

Where n_{sync} is the synchronous speed of the machine in rpm, f is the frequency in hertz of the network and p is the number of poles. As evident from Equation 2.1, an increase in the number of poles results in a decrease in rotational speed. If the produced torque exceeds the stiction torque, the rotor starts to accelerate. Due to the sinusoidal distribution of the flux, a sinusoidal electromotive force (EMF) is induced in the rotor conductors, leading to the flow of current within them. Consequently, currents are present in both the stator and rotor, generating localized fluxes that interact with the excitation flux from the stator. This interaction produces a torque in the rotor, and if this torque exceeds the mechanical load torque, the shaft will begin to rotate until equilibrium is reached, as described by Equation 2.2.

$$J\frac{d\Omega_r}{dt} = T_e - T_L \tag{2.2}$$

Where J is the inertia of the motor, Ω_r is the mechanical speed, T_e is the torque created by the motor and T_L is the mechanical load torque.

The rotor speed cannot match the synchronous speed of the stator; otherwise, no electromotive force (EMF) would be induced, resulting in the absence of current in the rotor and, consequently, no torque generation. The difference in speed between the stator's magnetic field and the rotor is referred to as slip. At the moment of startup, the slip is equal to 1 (or 100%). The formula used to calculate slip is provided in Equation 2.3.

$$s = \frac{n_s - n_r}{n_s} \tag{2.3}$$

Where n_s is the synchronous speed and n_r is the rotor speed [7].

2.1.1 Equivalent Induction Machine Circuit

To further analyze the electrical characteristics of the induction motor, an equivalent circuit model is used. This model is shown in below Figure 3.

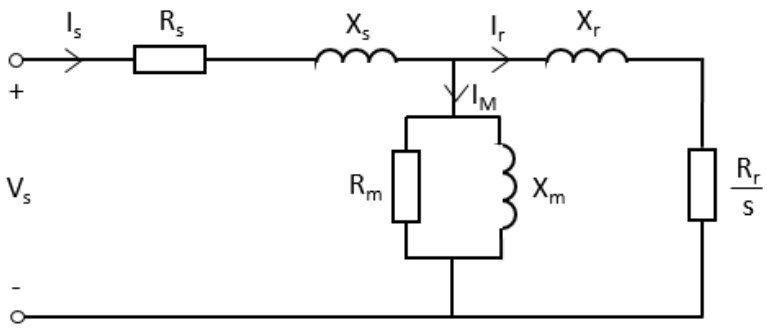

Figure 3: Equivalent circuit of Induction machine

The parameters included in the circuit are as follows

- V_s: Stator voltage
- I_s and I_r: Stator and rotor currents
- R_s and R_r: Stator and rotor resistances
- X_s and X_r: Stator and rotor reactances
- X_m, I_m and R_m: Magnetizing reactance, current and iron core resistance

2.1.2 Thevenin Equivalent Circuit and Torque Calculation

Furthermore, the induction machine equivalent circuit can be used to calculate the rotor current and torque through the use of Thevenin equivalent circuit as per below Figure 4.

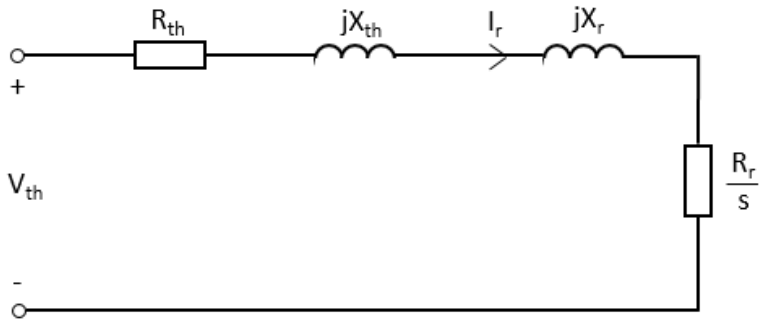

Figure 4: Thevenin equivalent circuit of induction machine

Where V_{th} is the Thevenin voltage, R_{th} is the Thevenin resistance and X_{th} is the Thevenin reactance. The Thevenin voltage is defined with below equation:

$$V_{th} = V_s \cdot \frac{jX_m}{R_s + j(X_s + X_m)} \tag{2.4}$$

The core losses, R_m, are neglected in this case. The corresponding Thevenin impedance is then expressed as:

$$Z_{th} = \frac{jX_m(R_s + jX_s)}{R_s + j(X_s + X_m)} = R_{th} + jX_{th} \tag{2.5}$$

To determine the rotor current, the Thevenin voltage and impedance are utilized:

$$I_r = \frac{V_{th}}{Z_{th} + Z_2} = \frac{V_{th}}{R_{th} + jX_{th} + jX_r + \frac{R_r}{s}} = \frac{V_{th}}{(R_{th} + \frac{R_r}{s}) + j(X_{th} + X_r)} \tag{2.6}$$

The magnitude of the rotor current is then given by:

$$|I_r| = \frac{V_{th}}{\sqrt{(R_{th} + \frac{R_r}{s})^2 + (X_{th} + X_r)^2}} \tag{2.7}$$

With the rotor current now known, the air-gap power can be calculated:

$$P_0 = 3I_r^2 \frac{R_r}{s} = \frac{3V_{th}^2 \frac{R_r}{s}}{(R_{th} + \frac{R_r}{s})^2 + (X_{th} + X_r)^2} \tag{2.8}$$

The torque is determined by the power in the air-gap and the synchronous speed as per below equation:

$$T_e = \frac{P_0}{w_s} = \frac{3V_{th}^2}{(R_{th} + \frac{R_r}{s})^2 + (X_{th} + X_r)^2} \frac{R_r}{s} \frac{1}{w_s} \tag{2.9}$$

By then substituting the slip with 1, the starting torque of the motor can be calculated which is useful for the hand calculations to estimate the torque and current [7].

By substituting the slip with 1, an estimate of the motor's starting torque can be calculated using the steady-state torque equation, which is useful for hand calculations to approximate torque and current [7]. However, this method does not accurately reflect the true starting torque, as it differs from values obtained through electromagnetic transient (EMT) simulations or those provided in datasheets. This discrepancy arises because the steady-state model does not capture dynamic effects present at startup.

2.1.3 Transforming Three-phase system to Two-phase system

The equivalent circuit of an induction machine offers valuable insights for theoretical calculations of torque and current. However, for control applications, the dynamic model is generally preferred. The induction machine model is often described using space vector theory and transformations into a synchronous reference frame, which simplifies the analysis. By selecting the synchronous dq reference frame, where the rotor space vector is aligned with the d-axis, the dynamic equations of the induction motor become similar to that of a separately magnetized DC motor. Making the equations of the induction motor simplified and easier to analyze [9]. The different reference frames can be visualized in Figure 5 below.

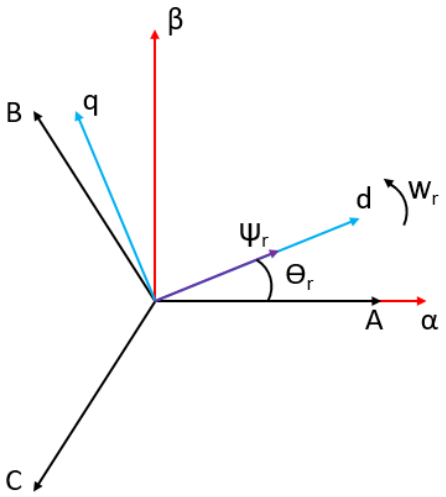

Figure 5: State space vector diagram to convert from three-phase to two-phase system for an induction machine

By assuming that the three-phase stator currents are instantaneous and balanced, the sum of the currents will be equal to zero and this also means the stator current space vector can be defined

as:

$$\bar{i}_s^s = i_{s\alpha} + j i_{s\beta} = \bar{i}_{sa} + \bar{i}_{sb} + \bar{i}_{sc} = k(i_{sa} + a i_{sb} + a^2 i_{sc}) \tag{2.10}$$

Where $i_{s\alpha}$ is the real component of the stator current space vector and $i_{s\beta}$ corresponds to the imaginary component in the stationary frame. $\bar{i}_{sa}, \bar{i}_{sb}$ and $\bar{i}_{sc}$ are the space vectors for the three-phase currents. The variable k is a scaling factor that determines whether the space vector uses peak values, RMS values or other scaling conversions. By putting $k = 1$, amplitude invariant scaling is used where $|\overline{X}^s| = \hat{x}_a = \hat{x}_b = \hat{x}_c$ where $\hat{x}_x$ is the peak phase value. Putting $k = 1/\sqrt{2}$ gives RMS value scaling where instead of peak value, every $x_{x,RMS}$ represents the RMS value of each phase. The simplest and most common choice is setting $k = 2/3$ and it will be used in this thesis. Additionally, a and a^2 are spatial operators that represents the 120°phase shift in a balanced three-phase system, $a = e^{2\pi/3}$ and $a^2 = e^{4\pi/3}$. Finally, by splitting the real and imaginary part of the stator current space vector, the α and β components can be calculated as per below matrix [9]:

$$\begin{bmatrix} i_{s\alpha} \\ i_{s\beta} \\ i_0 \end{bmatrix} = \frac{2}{3} \begin{bmatrix} 1 & -\frac{1}{2} & -\frac{1}{2} \\ 0 & \frac{\sqrt{3}}{2} & -\frac{\sqrt{3}}{2} \\ \frac{1}{2} & \frac{1}{2} & \frac{1}{2} \end{bmatrix} \begin{bmatrix} i_a \\ i_b \\ i_c \end{bmatrix} \tag{2.11}$$

The variable i_0 represents the zero-sequence component which is associated with symmetrical components

$$i_0 = \frac{1}{3}(i_a + i_b + i_c) \tag{2.12}$$

It will be equal to zero under balanced conditions. The space vectors of voltage and magnetic fluxes are defined in a similar way. Furthermore, to express the space vectors from the stationary frame in the rotating frame or dq frame. The quantities have to be multiplied with $e^{j\theta_r}$ where θ_r is the rotor flux angle and it's calculated by:

$$\theta = atan \frac{\psi_{r\beta}}{\psi_{r\alpha}} \tag{2.13}$$

Where $\psi_{r\alpha}$ and $\psi_{r\beta}$ are the rotor flux linkages in the stationary frame. So, to convert the $\alpha\beta$ system to the dq system, the following matrix can be used:

$$\bar{i}_s = i_{sd} + j i_{sq} = \bar{i}_s^s e^{-j\theta} \Rightarrow \begin{bmatrix} i_{sd} \\ i_{sq} \\ i_0 \end{bmatrix} = \begin{bmatrix} cos(\theta) & sin(\theta) & 0 \\ -sin(\theta) & cos(\theta) & 0 \\ 0 & 0 & 1 \end{bmatrix} \begin{bmatrix} i_{s\alpha} \\ i_{s\beta} \\ i_0 \end{bmatrix} \tag{2.14}$$

The conversion from dq frame to $\alpha\beta$ frame is done similarly [9]:

$$\bar{i}_s^s = i_{s\alpha} + j i_{s\beta} = \bar{i}_s^s e^{j\theta} \Rightarrow \begin{bmatrix} i_{s\alpha} \\ i_{s\beta} \\ i_0 \end{bmatrix} = \begin{bmatrix} cos(\theta) & -sin(\theta) & 0 \\ sin(\theta) & cos(\theta) & 0 \\ 0 & 0 & 1 \end{bmatrix} \begin{bmatrix} i_{sd} \\ i_{sq} \\ i_0 \end{bmatrix} \tag{2.15}$$

2.1.4 Dynamic Induction Machine Model Derivation

To derive the dynamic model of the induction machine, the analysis begins with the stator circuit. The portion of the stator voltage that is not dissipated by the stator resistance contributes to the development of flux linkage in the stator winding, expressed as:

$$\overline{u}_s^s = R_s \overline{i}_s^s + \frac{d\overline{\psi}_s^s}{dt} \tag{2.16}$$

Where $\overline{u}_s^s$, $\overline{i}_s^s$ and $\overline{\psi}_s^s$ are space vectors for the stator voltage, current and flux linkage respectively. Furthermore, the rotor voltage has the same relationship. However, for a squirrel cage induction machine, the rotor windings are short circuited, giving $\overline{u}_s^s = 0$:

$$0 = \overline{u}_r^r = R_r \overline{i}_r^r + \frac{d\overline{\psi}_r^r}{dt} \tag{2.17}$$

In order to simplify the model further, the state space vectors located in rotor coordinates will be transformed to stator coordinates by using the rotor position relationship:

$$\frac{d\theta_r}{dt} = w_r \Rightarrow \theta_r = \int w_r dt \tag{2.18}$$

Which can then be used to convert the current and flux linkage from rotor coordinates to stator coordinates as per below equations

$$\overline{i}_r^s = e^{j\theta_r} \overline{i}_r^r, \quad \overline{\psi}_r^s = e^{j\theta_r} \overline{\psi}_r^r \tag{2.19}$$

By then inserting Equation 2.19 into Equation 2.17, the rotor voltage equation becomes:

$$\begin{aligned}
0 &= R_r \bar{i}_r^r + \frac{d\bar{\psi}_r^r}{dt} \\
&= \left\{ \frac{d\bar{\psi}_r^r}{dt} = \frac{d}{dt}\left(\bar{\psi}_r^s e^{-j\theta_r}\right) = \frac{d\bar{\psi}_r^s}{dt} e^{-j\theta_r} - j\omega_r e^{-j\theta_r} \bar{\psi}_r^s \right\} \\
&= R_r \bar{i}_r^s \cancel{e^{-j\theta_r}} + \frac{d\bar{\psi}_r^s}{dt} \cancel{e^{-j\theta_r}} - j\omega_r \cancel{e^{-j\theta_r}} \bar{\psi}_r^s \\
&\Rightarrow 0 = R_r \bar{i}_r^s + \frac{d\bar{\psi}_r^s}{dt} - j\omega_r \bar{\psi}_r^s
\end{aligned} \tag{2.20}$$

The flux linkages in the voltage equations are described by the following relations where $L_s = L_{sl} + L_m$ and $L_r = L_{rl} + L_m$

$$\overline{\psi}_s^s = L_s \overline{i}_s^s + L_m \overline{i}_r^s \tag{2.21}$$

$$\overline{\psi}_r^s = L_r \overline{i}_r^s + L_m \overline{i}_s^s \tag{2.22}$$

By combining above Equations 2.16, 2.20, 2.21 and 2.22, the dynamic T-equivalent circuit can be obtained and it's shown with below equations and Figure 6.

$$\overline{u}_s^s = R_s \overline{i}_s^s + L_{sl} \frac{d\overline{i}_s^s}{dt} + L_m \frac{d\overline{i}_r^s}{dt} \tag{2.23}$$

$$0 = \overline{u}_r^s = R_r \overline{i}_r^s + L_{rl} \frac{d\overline{i}_r^s}{dt} + L_m \frac{d\overline{i}_s^s}{dt} - j w_r \overline{\psi}_r^s \tag{2.24}$$

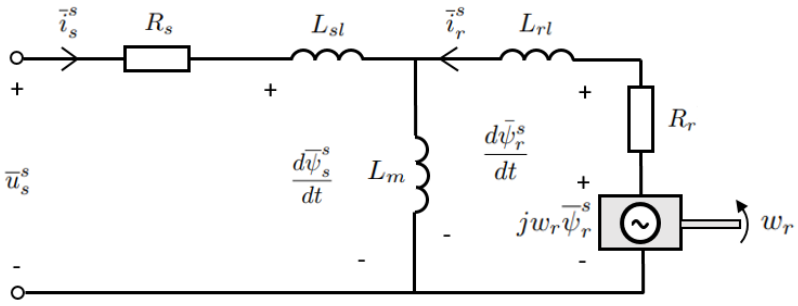

Figure 6: Dynamic model of Induction machine in $\alpha\beta$ coordinates

The Dynamic model can converted to rotating frame or dq frame which rotates with the arbitrary speed, w_1. This is done by using the following equations:

$$\overline{u}_s^s = \overline{u}_s e^{j\theta_1}, \;\; \overline{i}_s^s = \overline{i}_s e^{j\theta_1}, \;\; \overline{\psi}_s^s = \overline{\psi}_s e^{j\theta_1}, \;\; \theta_1 = \int w_1 dt \tag{2.25}$$

Furthermore, by inserting these equations into 2.23 and 2.24 and using the chain rule, the following equations can be derived.

$$\overline{u}_s = R_s \overline{i}_s + \frac{d\overline{\psi}_s}{dt} + j w_1 \overline{\psi}_s \tag{2.26}$$

$$0 = \overline{u}_r = R_r \overline{i}_r + \frac{d\overline{\psi}_r}{dt} + j(w_1 - w_r)\overline{\psi}_r \tag{2.27}$$

The torque produced in the rotating frame model can be calculated as

$$T_e = \frac{P_e}{\Omega_r} = \frac{P_e n_p}{w_r} = \frac{3n_p}{2} Im\left\{ \overline{\psi}_s^{s^*} \bar{i}_s^s \right\} = \frac{3n_p}{2} Im\left\{ \left(\overline{\psi}_s e^{j\theta_1} \right)^* \bar{i}_s e^{j\theta_1} \right\} \tag{2.28}$$

$$= \frac{3n_p}{2} Im\left\{ \overline{\psi}_s^* e^{-j\theta_1} \bar{i}_s e^{j\theta_1} \right\} = \frac{3n_p}{2} Im\left\{ \overline{\psi}_s^* \bar{i}_s \right\} \tag{2.29}$$

Where P_e is the shaft power of the machine [9].

2.2 Power Transmission and Control System

The power system layout for a common subsea application is shown in Figure 1 above and consists of one main topology for supplying the compressor motor including the VSD, transformers and cable. The transformers enable significantly longer cable connections, reaching up over one-hundred kilometers [10]. The transmission system must ensure adequate power delivery while maintaining the required rms line-to-line motor voltage.

2.2.1 Transformer

Transformers are essential for enabling efficient power transmission by adjusting voltage levels throughout the system. Step-up transformers are specifically designed to increase voltage levels, which lowers current and reduces resistive losses over long distances. This is particularly important in subsea environments where space and weight constraints demand compact and efficient power solutions. However, high voltages also increase capacitive charging currents in cables, which must be carefully balanced to avoid overloading components. Selecting appropriate transformer voltage levels is therefore key to maintaining system stability and efficiency. At the receiving end, step-down transformers, or subsea transformers, can be placed on the seabed, and they lower the voltage to levels suitable for equipment such as motors, pumps and compressors, ensuring safe and reliable operation. The equivalent circuit of the transformer used in this project can be shown in Figure 7 below [11].

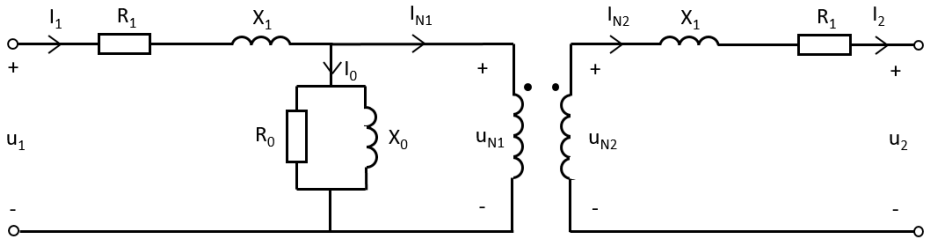

Figure 7: Equivalent circuit of the transformer

The equivalent circuit of the transformer, shown in Figure 7, represents its electrical behavior where the circuit illustrates how voltage, current, resistance, and reactance interact within the transformer. u_1 and u_2 are the primary and secondary side voltages, respectively, while I_1 and I_2 represent the corresponding currents. The no-load current, I_0, splits into the magnetizing current through the magnetizing reactance, X_0, and the eddy current through the resistance, R_0. Additionally, R_1 and X_1 denote the primary and secondary resistance and reactance.

While the equivalent circuit captures the transformer's steady-state electrical behavior, the underlying principle behind voltage induction is explained by Faraday's Law of Electromagnetic Induction. This law states that a time-varying magnetic field induces a voltage in a coil, which is the fundamental mechanism that allows transformers to transfer energy between windings without direct electrical contact [12]. Mathematically, Faraday's Law is expressed as:

$$V = -N\frac{d\phi}{dt} \tag{2.30}$$

where V is the induced voltage, N is the number of turns in the winding and ϕ is the magnetic flux. For estimating the magnetic flux using the voltage and number of windings, Equation 2.30 can be rearranged into the following equation:

$$\phi = -\frac{1}{N}\int V dt \tag{2.31}$$

In addition to the equivalent circuit and Faraday's law, it's important to consider transformer saturation. The core is made of ferromagnetic material, which becomes magnetized when exposed to a magnetic field [13]. As the magnetizing force, H, increases, the flux density B, increases and this happens up to a certain point before the core reaches saturation. This can be illustrated by the B-H hysteresis loop in Figure 8 below.

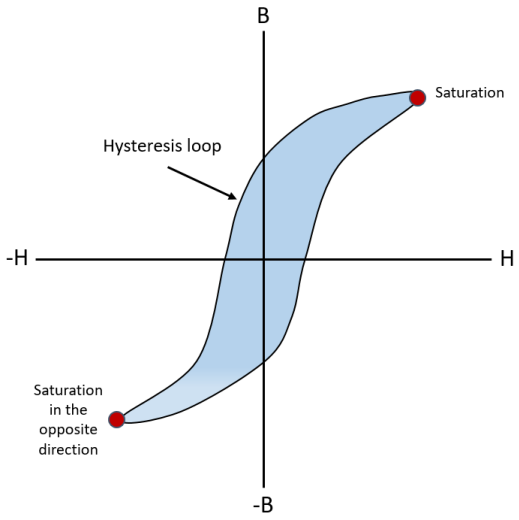

Figure 8: B-H hysteresis loop

Operating close to saturation can lead to distortion, overheating, and reduced efficiency.

2.2.2 Subsea Cable

Cables are a fundamental component for power systems, providing the physical medium for transmitting the electrical energy from the source to the load. In subsea power systems, specialized subsea cables are utilized to deliver power to installations such as pumps and compressors. These cables are designed to withstand harsh marine conditions, including high pressure, corrosion, and

mechanical stress. The length of the cable affects its type and specifications, such as insulation, cross-sectional area, and material composition. Modern medium-voltage submarine cables (up to 52 kV) are typically designed as three-core (3C) cables with XLPE insulation, similar in core construction to land cables [14]. A typical three-core cable used in today's subsea power systems is shown in below Figure 9.

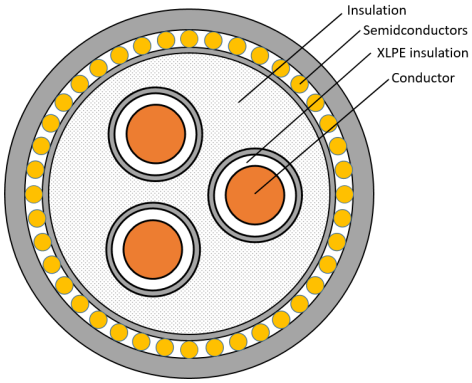

Figure 9: Three-core subsea cable

A wide variety of design options exist for this class of cables. Protective layers can be applied either to each individual core or to all three cores collectively, and a range of screen and sheath configurations is used.

Depending on project requirements, these cables may be manufactured with or without a metallic sheath. Due to the relatively low electric stress in medium-voltage extruded cables, a fully watertight design is not always necessary. An extruded plastic sheath often serves as a reliable water barrier, while embedded water-absorbing materials handle minor moisture ingress.

A common design includes an aluminum laminate for radial water protection, paired with a copper wire screen capable of carrying fault currents. Some three-core cables use non-metallic sheaths made from semi-conductive polymeric materials. In such cases, the capacitive currents from each phase can partially cancel out, improving the cable's ampacity.

Various combinations of sheath, screen, and corrosion protection are used to adapt to specific installation environments. Manufacturers typically employ proprietary designs to meet the diverse technical and environmental demands of submarine power transmission [14].

2.2.3 Cable modelling

There are three primary approaches for modeling transmission lines: the Short, Medium and Long Line Models [15]. These models are originally based on overhead lines, which have significantly lower capacitance than submarine or underground cables. For overhead lines shorter than 80 km, the Short Line Model is often sufficient, as it negelcts shunt capacitance with minimal impact on accuracy. However, for cables, even those under 80 km, this simplification is inadequate due to their much higher capacitance.

For line lengths between 80 km and 240 km, the Medium Line Model, or Pi-model, is normally used. This model effectively represents the cable by lumping the shunt admittances at a few points along the line, forming a π-section. This model captures key effects such as line charging current and capacitive behavior more accurately than the Short Line Model. The π-model accounts for both the

line charging currents and shunt capacitance's, ensuring a more accurate model than the Short Line Model.

In contrast, for lines exceeding 240 km, the Long Line Model becomes necessary. This model treats the electrical parameters—resistance, inductance, capacitance, and conductance—as distributed continuously along the cable, providing improved accuracy in simulating voltage drops, reactive power flow, and transient behavior. In this thesis, the Long Line Model is used to achieve the most accurate results despite it being below 240 km.

2.2.4 Distributed parameter line model derivation

The equivalent circuit for one phase of the Long Line Model is shown in Figure 10 below.

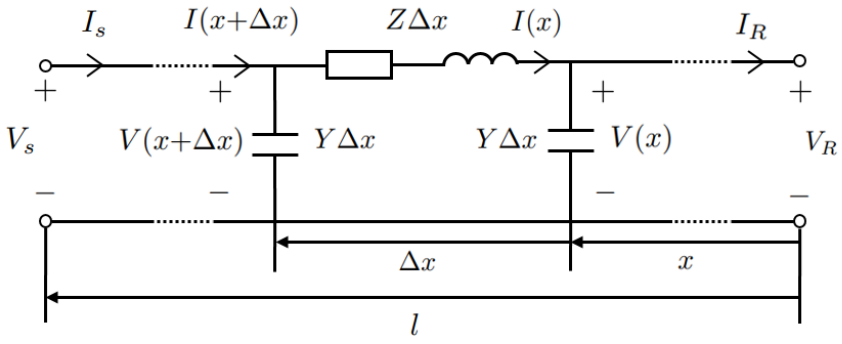

Figure 10: Long Line Model of the Cable

Where the variables are denoted as below

- V_S & V_R: Sending and receiving end voltage.
- I_s & I_R: Sending and receiving end current
- Z & Y: Impedance and admittance per unit length.

In the model, the impedance and shunt capacitance are distributed instead of lumped together and they can be explained with below equations:

$$Z = R + jX \qquad (2.32) \qquad\qquad Y = G + jwC \qquad (2.33)$$

Where R represents the resistance per unit length, X denotes the reactance per unit length, G corresponds to the conductance per unit length, and C signifies the capacitance per unit length. Furthermore the propagation constant of the network can be described by the following equation:

$$\gamma = \alpha + j\beta = \sqrt{ZY} = \sqrt{(R + jwL)(G + jwC)} \qquad (2.34)$$

The variables α and β are attenuation and phase constant respectively. and the characteristic (Surge) impedance of the system is given by the following equation:

$$Z_c = \sqrt{\frac{Z}{Y}} = \sqrt{\frac{R \ + \ jwL}{G \ + \ jwC}} \tag{2.35}$$

To determine the voltages and currents at the sending and receiving ends of the transmission line, it is necessary to solve a set of differential equations. By examining an segment of the transmission line at a distance Δx the Telegrapher's equations describe the voltage drop and current leakage as follows:

$$V(x,t) - V(x+\Delta x,t) = -(R+jwL)\Delta x I(x,t) \tag{2.36}$$
$$I(x,t) - I(x+\Delta x,t) = -(G+jwC)\Delta x V(x+\Delta x,t) \tag{2.37}$$

By then dividing the above equations with Δx and then taking the limit as $\Delta x \rightarrow 0$, partial differential equations are acquired as per below.

$$\frac{\partial V(x,t)}{\partial x} = -(R+jwL)I(x,t) \tag{2.38}$$
$$\frac{\partial I(x,t)}{\partial x} = -(G+jwC)V(x,t) \tag{2.39}$$

For sinusodial steady state analysis, $V(x,t) = Re\{V(x)e^{jwt}\}$ and $I(x,t) = Re\{I(x)e^{jwt}\}$ are used so the time dependence is removed which leaves the following equations:

$$\frac{dV(x)}{dx} = -ZI(x) \tag{2.40}$$
$$\frac{dI(x)}{dx} = -YV(x) \tag{2.41}$$

To solve these equations, they are both differentiated with respect to x into second order differential equations and decoupled by substituting $\frac{dV(x)}{dx}$ and $\frac{dI(x)}{dx}$ with $-ZI(x)$ and $-YV(x)$ respectively, as well as inserting Equation 2.34:

$$\frac{d^2V(x)}{dx^2} = -Z\frac{dI(x)}{dx} = -Z(-YV(x)) = ZYV(x) = \gamma^2 V(x) \tag{2.42}$$

$$\frac{d^2I(x)}{dx^2} = -Y\frac{dV(x)}{dx} = -Y(-ZI(x)) = ZYI(x) = \gamma^2 I(x) \tag{2.43}$$

Knowing the surge impedance and propagation constant, the voltage and current at distance x from the receiving end can be calculated by the following equations:

$$V(x) = cosh(\gamma x)\cdot V_R \ + \ Z_c sinh(\gamma x)\cdot I_R \tag{2.44}$$

$$I(x) = \frac{1}{Z_c} sinh(\gamma x)\cdot V_R \ + \ cosh(\gamma x)\cdot I_R \tag{2.45}$$

From these equations, the transmission matrix can be derived where:

$$V_S = A \cdot V_R + B \cdot I_R \tag{2.46}$$

$$I_S = C \cdot V_R + D \cdot I_R \tag{2.47}$$

$$\begin{bmatrix} V_S \\ I_S \end{bmatrix} = \begin{bmatrix} A & B \\ C & D \end{bmatrix} \begin{bmatrix} V_R \\ I_R \end{bmatrix} \Rightarrow \begin{bmatrix} V_R \\ I_R \end{bmatrix} = \begin{bmatrix} D & -B \\ -C & A \end{bmatrix} \begin{bmatrix} V_S \\ I_S \end{bmatrix} \tag{2.48}$$

Combining the equations 2.44 and 2.45 with equations 2.46 and 2.47, the variables A, B, C and D can be calculated and the transmission matrices then becomes:

$$\begin{bmatrix} V_S \\ I_S \end{bmatrix} = \begin{bmatrix} cosh(\gamma x) & Z_c sinh(\gamma x) \\ \frac{1}{Z_c} sinh(\gamma x) & cosh(\gamma x) \end{bmatrix} \begin{bmatrix} V_R \\ I_R \end{bmatrix} \Rightarrow \begin{bmatrix} V_R \\ I_R \end{bmatrix} = \begin{bmatrix} cosh(\gamma x) & -Z_c sinh(\gamma x) \\ -\frac{1}{Z_c} sinh(\gamma x) & cosh(\gamma x) \end{bmatrix} \begin{bmatrix} V_S \\ I_S \end{bmatrix} \tag{2.49}$$

Utilizing the derived transmission matrices and corresponding equations, the voltage and current at any given point along the transmission line can be accurately calculated for both the receiving and sending ends. By using these matrices and equations, it becomes possible to model the behavior of the transmission line over its entire length, accounting for the effects of the distributed parameters such as resistance, inductance, capacitance, and conductance. These calculations provide a more detailed analysis of the voltage and current profiles at any location on the line compared to the short and medium line model, improving the evaluation of power flow, impedance characteristics, and the impact of any transient or steady-state conditions [16].

2.2.5 Load Model

The motor drives a subsea pump as shown in Figure 1 and the pump can be modeled as a load model. To describe the pump load behavior, the following general load equation is introduced:

$$T_{pump} = k\omega^2 \tag{2.50}$$

where T_{pump} is the pump torque, k is a pump constant, and ω represents the rotational speed. The quadratic relationship reflects the typical behavior of a pump load, where torque increases with the square of speed. Figure 11 illustrates the load torque characteristic of the pump [17].

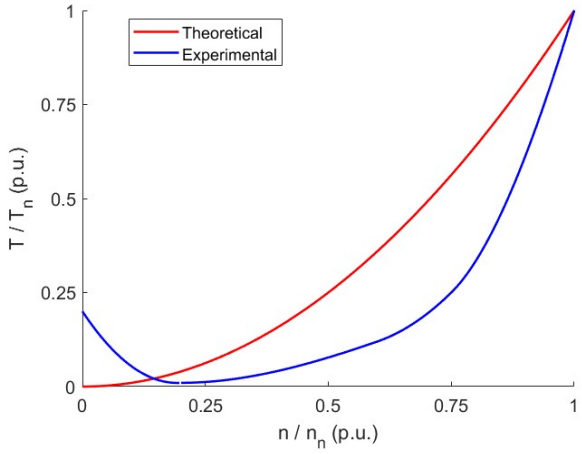

Figure 11: Load torque characteristic curve of pump

The theoretical torque increases with the square of the speed, following an ideal parabolic trend. The experimental curve shows the actual torque, which deviates from the theoretical curve, especially at lower speeds due to mechanical and hydraulic inefficiencies. At very low speeds, actual torque is higher than theoretical, reflecting real-world startup resistance. As speed increases, the curves converge near nominal speed. This illustrates how real pumps require more torque at low speeds than predicted by theory.

2.2.6 Variable Speed Drive

The Variable Speed Drive (VSD) is a key component in modern power systems, enabling precise control of motor speed and torque to match process demands. In subsea applications, where long transmission distances and dynamic load conditions are common, VSDs play a crucial role in ensuring stable and efficient operation. This section outlines the theoretical background and control principles of VSDs relevant to the thesis, with focus on Voltage over frequency (V/f) control and its suitability for long step-out scenarios.

2.2.7 Voltage/frequency control

V/f control is a scalar control method used in variable speed drives to regulate the speed of induction motors by maintaining a constant V/f ratio. This ensures that the output voltage is proportional to the frequency, maintaining a constant motor magnetic flux [18]. V/f scalar control is the primary method for controlling induction motors and is especially suitable for subsea applications with long step-outs due to its simplicity. As an open-loop method, it does not require rotor position measurement or estimation.

In section 2.1.1, figure 3 shows the steady-state equivalent circuit, where the stator resistance (R_s) is assumed to be zero, and the stator leakage inductance (L_s) is combined with the rotor leakage inductance (L_r). The magnetizing inductance is placed before the total leakage inductance and represents the air gap flux ($L = L_s + L_r$). The stator voltage to frequency ratio provides a useful approximation for the magnetizing current responsible for producing the air gap flux. This relationship is fundamental to V/f control and can be described using the following phasor equation:

$$I_m = \frac{V_s}{j\omega L_m} \tag{2.51}$$

If the induction motor is operating within the linear region of the magnetic characteristic, the magnetizing inductance L_m can be considered constant. Under this assumption, the magnetizing current and flux linkage are related by:

$$I_m = \frac{\Phi_m}{L_m} \tag{2.52}$$

Considering the stator voltage and electrical frequency, the magnetizing current can alternatively be expressed as:

$$I_m = \frac{V_s}{(2\pi f)L_m} \tag{2.53}$$

Rearranging this expression gives the air gap flux as a function of voltage and frequency:

$$\Phi_m = \frac{V_s}{f} \tag{2.54}$$

Where V_s and f is the nominal stator voltage and frequency. An example of a typical V/f characteristic curve is presented in Figure 12 below.

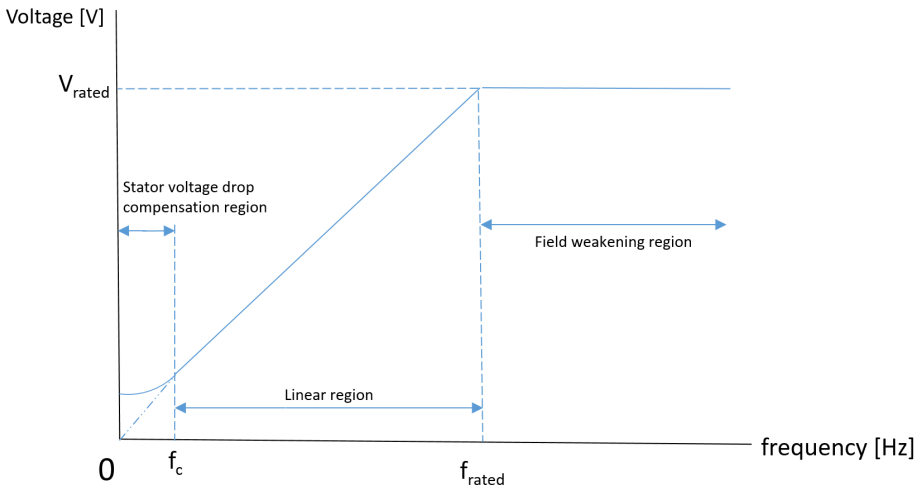

Figure 12: Stator voltage versus frequency profile under V/f control

At low frequencies, a certain voltage is required to compensate for the voltage drop across the stator resistans (R_s) in Figure 3, which can't be ignored [19]. To maintain proper motor performance, the stator voltage must be increased, making the V/f profile non-linear in this region. The cutoff frequency (f_c) and the corresponding stator voltages can be determined analytically using the steady-state equivalent circuit with $R_S \neq 0$. In the linear region the constant V/f relationship is maintained, ensuring a stable air gap flux. This region is crucial for maintaining efficient torque production and steady motor operation. At frequencies higher than the rated value, maintaining a constant V/f ratio is no longer feasible because the stator voltage is limited to its rated value to prevent insulation breakdown in the stator windings. As a result, the air gap flux decreases, leading to a

corresponding reduction in developed torque. This operating range is known as the field-weakening region, where the constant V/f principle is intentionally violated to avoid excessive voltage stress on the motor.

In subsea applications with long step-outs, additional factors such as capacitive charging currents and voltage drops further influence the V/f profile, requiring careful tuning to maintain efficiency. Because the stator flux stays constant under variations in supply frequency, the torque produced by an AC induction motor is mainly influenced by the slip speed. By adjusting the slip, it is possible to control both the motor's torque and rotational speed, provided the system operates within the constant voltage-to-frequency ratio framework.

2.2.8 Power Electronic Converter

In subsea power systems, the term "topside" refers to components situated above water, typically installed on offshore oil platforms. Electric power is generally supplied either by onboard generators or via subsea cables connected to an onshore power station. To effectively control the induction motor located on the seabed, it is essential to precisely adjust both the frequency and voltage from their initial levels to the rated values. This regulation is achieved through the use of a VSD installed topside and a basic VSD configuration is shown in Figure 13 below [7].

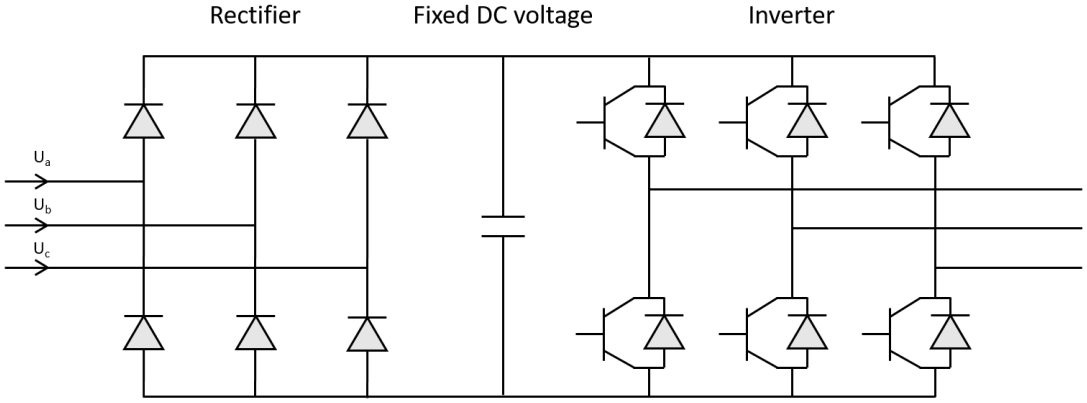

Figure 13: Variable Frequency Drive

The frequency converter is a power electronic device designed to generate an output voltage with variable amplitude and frequency, which is essential for controlling the speed and torque of an induction machine. It typically comprises three main components: a three-phase rectifier, a direct current (DC) link and an inverter. Most frequency converters operate as AC-AC converters, where the alternating current (AC) input is transformed into an AC output through intermediate DC processing. The capacitor within the DC link is used to smoothen the rectified DC voltage by reducing ripple and ensuring a stable and stiff input for the inverter stage. This DC voltage is then converted to AC output voltage using the inverter's active switching elements [7].

2.2.9 Sinusoidal Pulse Width Modulation

To achieve a variable output voltage and frequency, a technique known as Sinusodial Pulse Width Modulation (SPWM) is often used. In this method, a modulator is connected to the gate terminals of the Insulated Gate Bipolar Transistors (IGBTs) in the inverter. The duty cycle, which defines the width of the output pulses, ranges between 0 and 1 and is determined based on the phase voltage reference $v_{x,\text{ref}}$ and the DC-link voltage V_{DC}, according to the following expression [20]:

$$d_x = 0.5 + \frac{v_{x,\text{ref}}}{V_{DC}} \tag{2.55}$$

The calculated duty cycles are then compared to a high-frequency carrier waveform. This comparison modulates the width of the output pulses s_x, thereby enabling control of both voltage and frequency through PWM as per below equation and Figure 14:

$$s_x = \begin{cases} 1 & if \quad d_x \geq \ carrier \ \ wave \\ 0 & if \quad d_x < \ carrier \ \ wave \end{cases} \tag{2.56}$$

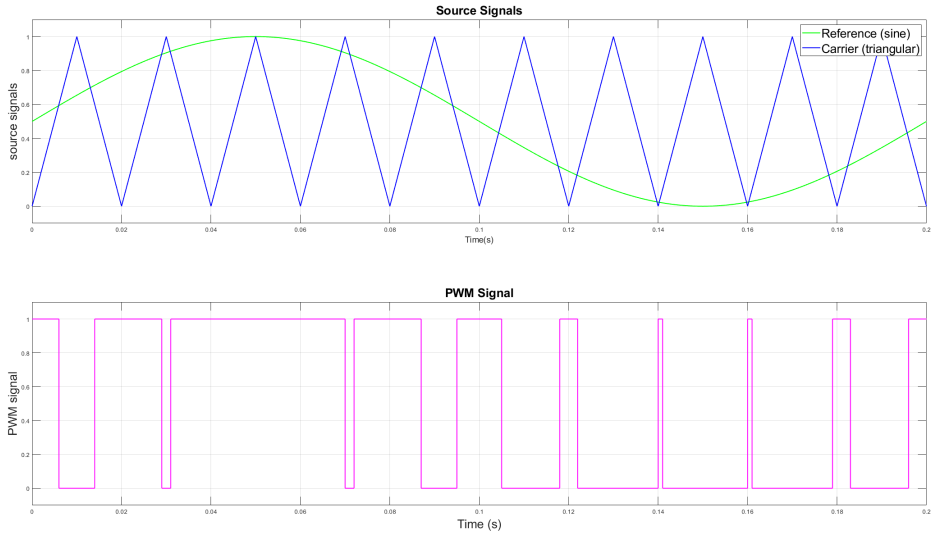

Figure 14: Pulse Width Modulation

The highest voltage the inverter can create is when the phase voltage peak value is equal to half the DC voltage:

$$|u^s|_{max} = \frac{V_{DC}}{2} \tag{2.57}$$

If the phase voltages are increased more, overmodulation is reached where the inverter stops switching during a part of the period. Leading to a less soft rotation. However, it's possible to have a higher voltage while also avoiding overmodulation by subtracting the zero-sequence component as per below:

$$v'_{a,ref} = v_{a,ref} - v_0 \tag{2.58}$$

$$v'_{b,ref} = v_{b,ref} - v_0 \quad \text{where} \quad v_0 = \frac{\max(v_{a,ref}, v_{b,ref}, v_{c,ref}) + \min(v_{a,ref}, v_{b,ref}, v_{c,ref})}{2} \tag{2.59}$$

$$v'_{c,ref} = v_{c,ref} - v_0 \tag{2.60}$$

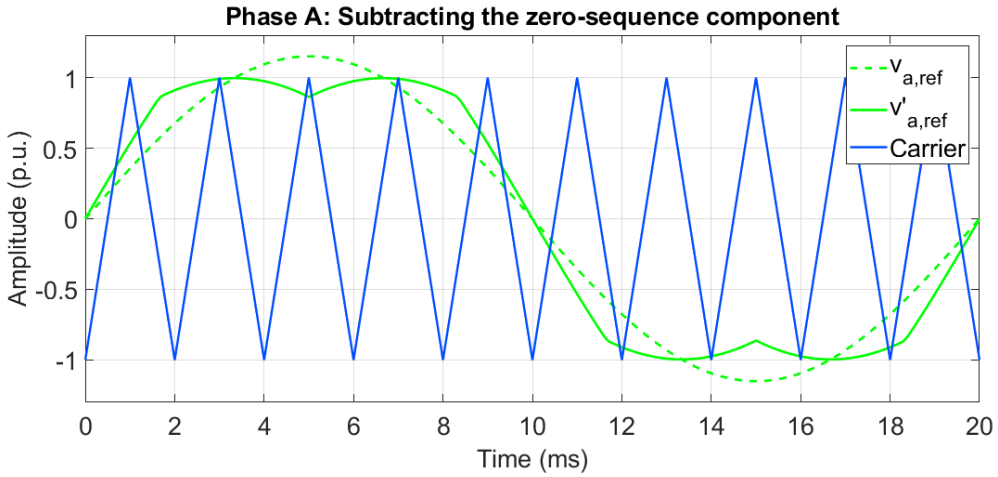

Figure 15: Subtraction of zero-sequence component for phase A

In this configuration, the maximum voltage that the inverter can generate occurs when the peak line-to-line voltage equals the DC-link voltage [20]. Under this condition, the maximum magnitude of the voltage vector in the stationary reference frame is given by:

$$\hat{u}_{l-l,max} = V_{DC} \rightarrow |u^s|_{max} = \frac{V_{DC}}{\sqrt{3}} \tag{2.61}$$

Furthermore, the load does not experience the zero-sequence voltage component v_0, as its neutral point is floating. As a result, the load is only influenced by the line-to-line voltages, in which the zero-sequence component is absent [20].

2.2.10 Harmonics

When an induction motor is started using a PWM inverter through a long transmission cable, its insulation system is subjected to significant electrical stress. The high dv/dt voltage pulses generated at the inverter output produce cable charging currents, which causes additional stress on the insulation system [21]. Additionally, voltage reflections are inevitable in the cable due to the stepwise nature of PWM signals, potentially resulting in voltage peaks up to twice the input voltage [22].

To mitigate harmonic distortion, the switching frequency can be selected high enough to allow the harmonics to be effectively attenuated by a relatively small output filter in the VSD. Sinewave filters are commonly employed to mitigate these effects by introducing a series inductance, which consequently shifts the resonance frequencies of the transmission system to a lower frequency range. Several filter configurations are available, including L filters, LC filters, and LCL filters, with the L filter being the most commonly implemented due to its non-resonant characteristics [23].

An alternative approach to reduce switching harmonics is the application of multilevel inverters, which shift the harmonic spectrum to higher frequencies, making them easier to filter [24]. However, in this thesis, a three-phase two-level inverter will be analyzed in PowerFactory, assuming a constant DC-link voltage for the simulation models.

2.2.11 Inverter Switching Frequency

When choosing the switching frequency for the PWM inverter, there are several important factors that needs to be considered. One of the main trade-offs is the current ripple and switching losses. If the switching frequency is kept low, the inverter generates more ripple in the current waveform. This is because the switching intervals are longer, allowing the current to fluctuate more before the next switching event occurs. On the positive side, lower switching frequencies also mean that the power electronics switch less frequently, which reduces switching losses and improves efficiency.

On the other hand, increasing the switching frequency reduces the amount of current ripple. The faster switching allows the current waveform to be more tightly controlled, resulting in smoother output. However, this comes with a cost in the form of higher switching losses. Each time the inverter switches, there is energy dissipated in the form of heat, and at high frequencies, these losses add up quickly. Therefore, there is always a compromise between improving current quality and minimizing power losses [25]. To illustrate the selection of the switching frequency, a frequency modulation index m_f is defined as

$$m_f = \frac{f_{sw}}{f_1} \tag{2.62}$$

Where f_{sw} is the switching frequency and f_1 is the fundamental frequency. Furthermore, It is recommended that for a small m_f ($m_f \leq 21$), synchronous PWM should be applied. This is because maintaining synchronous operation helps to prevent the occurrence of subharmonics. In this scenario, m_f must remain an integer value throughout the entire motor start-up process to avoid any low-frequency harmonic distortion. Consequently, the switching frequency f_{sw} needs to be adjusted simultaneously as the motor speed increases in order to maintain m_f as a constant value [25].

On the other hand, when m_f is large ($m_f > 21$), the use of synchronous PWM is no longer necessary. This is due to the natural reduction of subharmonics as m_f increases, allowing for more flexibility in switching strategies without the need for synchronous adjustment.

2.3 Transmission Challenges

Long transmission cables, particularly in high-voltage AC systems, present significant challenges due to their increased capacitance. As cable length increases, so does its capacitive charging effect, which leads to higher reactive power generation. This phenomenon may cause excessive voltage rise along the cable and at the receiving end, potentially exceeding operational limits and reducing overall power transfer efficiency. Additionally, the increased capacitive charging current can lead to higher losses, placing additional strain on the power system and requiring compensation measures. To mitigate these effects, shunt reactors are commonly used to absorb excess reactive power and stabilize voltage levels. Without adequate compensation, the system risks inefficient power transmission, voltage instability, and potential damage to equipment, making capacitance management a critical factor in long-distance power transmission.

2.3.1 Ferranti Effect

The Ferranti effect is a phenomenon in long transmission cables where the receiving-end voltage exceeds the sending-end voltage, particularly under no-load or light-load conditions [26]. A no-load test is essential when testing the power system to evaluate its behavior under minimal or zero load conditions. This helps identify key electrical characteristics and potential issues before the system is subjected to full operational loads. The Ferranti effect occurs due to the high capacitance of long cables, which causes excessive reactive power generation and a voltage rise along the cable. In

AC systems, this effect becomes more pronounced as cable length, frequency and operating voltage increase. A simplified π-model for the Ferranti effect for long AC transmission lines can be shown in Figure 16 below.

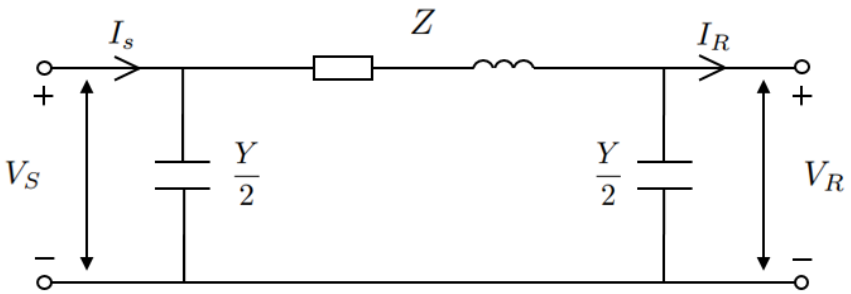

Figure 16: π-model for a transmission cable

The Ferranti effect is particularly relevant in this project due to the long length of the subsea cable. With low current flow, the voltage drop caused by resistance is minimal, while the cable's capacitance continues to charge, leading to an unintended voltage rise along the line. This can cause overvoltage at the receiving end, potentially exceeding equipment voltage ratings and compromising system stability. To manage this, proper compensation, such as shunt reactors, are required to mitigate the effect during operation.

2.3.2 Reactive Power Compensation

Reactive power compensation is vital for maintaining voltage stability, reducing losses, and improving efficiency, especially in long-distance and subsea transmission systems. Shunt reactors are commonly used to absorb excess reactive power caused by cable capacitance, preventing over-voltages under low or no-load conditions [27]. This is particularly important in high-voltage subsea applications, where motor loads are sensitive to voltage fluctuations [28].

By providing inductive compensation, shunt reactors help control voltage rise and reduce the reactive load on topside components including the VSD and step-up transformer [29]. Although variable shunt reactors can allow dynamic adjustment [30], this project assumes constant full-load operation. Therefore, a fixed inductance reactor with a constant inductance is selected for simplicity, despite the continued presence of the Ferranti effect.

3 Methodology

The method section outlines the approach used to model, simulate, and verify the power system. First, PowerFactory is introduced as the primary simulation tool. Then, a basic power system is constructed using a PQ load representation. Next, motor parameters are estimated to ensure accurate system behavior. The power system design is then validated with the motor model before integrating a variable speed drive. Finally, the entire system is simulated, assessing its performance under operational conditions before proceeding to the results analysis.

3.1 PowerFactory

PowerFactory is a widely used power system analysis software developed by DIgSILENT, designed for modeling, simulation, and optimization of electrical networks. It supports various analyses, including power transmission, power distribution, industrial systems, power generation, distributed generation and renewables, making it a valuable tool for power system engineers [31]. Load flow simulations in PowerFactory help evaluate system performance by calculating voltage profiles, power losses, and reactive power distribution under different operating conditions [32]. These simulations are essential for designing and optimizing power networks, ensuring efficient operation, and maintaining stability, particularly in complex systems such as offshore grids and long-distance cable networks.

3.2 Basic Power System using a PQ-load

To establish a foundational power system model, the network is initially constructed using a power source, transformers, a long-distance subsea cable, and a simple PQ-load. This setup allows for a preliminary analysis of the system's electrical behavior before integrating a motor model and ultimately a VSD.

The PQ-load represents the fixed active (P) and reactive (Q) power demand of the motor at the stator terminals, simplifying load flow analysis. This fixed demand makes it particularly useful for sizing equipment such as transformers and cables. The PQ-load also enables straightforward power flow analysis and voltage stability assessments under steady-state conditions, allowing for easier evaluation of transformer capacity. Proper transformer sizing ensures it operates within safe limits, preventing overloading, reducing losses, and maintaining voltage stability. The designed power system using a PQ-load in PowerFactory is shown in Figure 17.

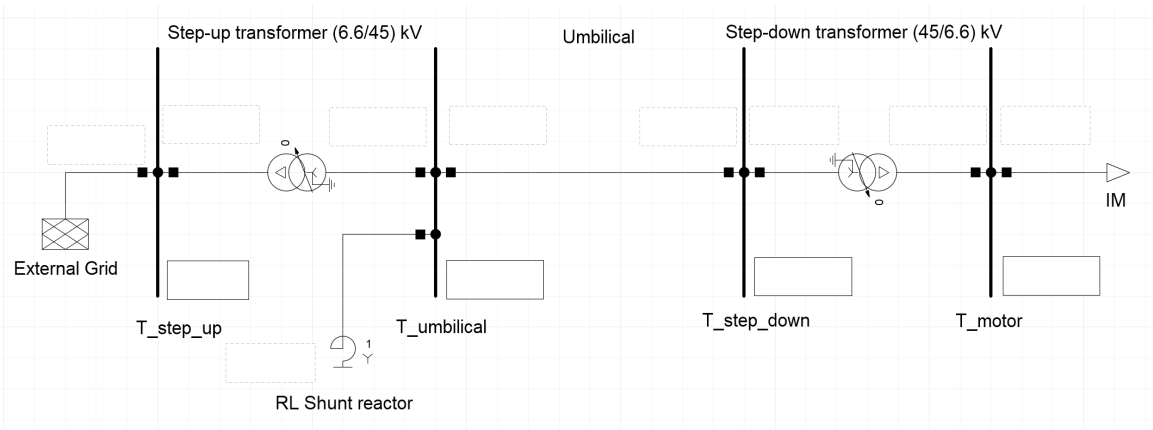

Figure 17: Power System using a PQ-load

Comparing Figure 17 with Figure 1, the VSD, which is represented by the external grid, along with the step-up transformer are located topside, meaning they are installed above the water sur-

face on land or a platform, while the rest of the power system are subsea. The introduced shunt compensator helps to maintain voltage stability and manage reactive power flow within the system, ensuring efficient operation of the transformers and cable. Without it, the system could experience excessive voltage drops and higher losses, potentially leading to poor power quality and inefficient performance.

The transformer parameters are scaled using common scaling relationships in transformers shown in Table 1 [33]. For this scaling, frequency, magnetic flux density, current density and basic insulation levels are all assumed to be constant. A standard transformer was selected as reference and then using the scale relationships, the new transformer was parameterized. These relations are generally valid within typical medium-to-high voltage power transformer ranges, ranging approximately from a few MVA up to several hundred MVA, and voltage levels up to a few hundred kV—where design practices remain relatively consistent.

One notable trend observed in the scaling is the decrease in per-unit short-circuit impedance with increasing power rating. This occurs because larger transformers are designed to minimize voltage drop and losses under load, which leads to lower impedance values relative to their higher base power. However, it's important to note that these trends may not hold for distribution transformers or for very large special-purpose transformers, where design constraints can differ significantly.

Table 1: Transformer Reference Scaling Relationships

Scaled Parameter	**Relationship to kVA Rating**
No-load losses, P_0	$(kVA_1/kVA_0)^{3/4}$
Load losses, P_k	$(kVA_1/kVA_0)^{3/4}$
Relative short-circuit voltage, e_z	$(kVA_1/kVA_0)^{-1/4}$
Relative resistance voltage drop, e_r	$(kVA_1/kVA_0)^{-1/4}$

In real-world applications, it's uncommon for all of the listed parameters to remain constant, even within narrow operating ranges. However, when increasing or decreasing the transformer size, the scaling relationships in Table 1 provide useful approximations for estimating transformer parameters. The final design parameters for the step-up and subsea transformers are shown in Table 2 below.

Table 2: Transformer parameters

	Step-up	**Step-down (subsea)**
Rated Power [MVA]	12.5	12.5
Rated Frequency [Hz]	50	50
Rated primary voltage [kV]	6.6	45
Rated secondary voltage [kV]	45	6.6
Resistance voltage, er [%]	0.9	0.9
Impedance voltage, ez [%]	8.4	8.4

These transformer parameters will serve as the standard configuration for all subsequent simulations and analyses throughout the thesis. By maintaining consistent transformer ratings, the system's performance can be evaluated under different conditions without introducing variations in transformer behavior. This ensures comparability between different simulation stages.

Shunt reactors are primarily designed for topside applications and have not been extensively tested for subsea use [34]. Therefore, the reactor is placed topside, on the high voltage side of the top-

side transformer, at the beginning of the transmission cable. Testing various configurations with one or two shunt reactors showed that the most effective placements were further away from topside. While these setups yielded similar results with slight advantages, practical considerations favor placing the reactor topside to compensate for increased capacitance. While these alternative setups provided slightly improved reactive power compensation, the difference was marginal. From a practical standpoint, placing the reactor topside simplifies installation, monitoring, maintenance, and thermal management. It also avoids the technical and cost challenges of designing equipment for subsea environments, such as pressure resistance, reliability under harsh conditions, and limited accessibility for repair or replacement.

The shunt reactor is sized to ensure that the power factor at the input of the step-up transformer is close to 1 for 100% load, minimizing the need for reactive power compensation and thus optimizing the VSDs power rating (since it only delivers active power, P). Overcompensation can lower system voltage by absorbing excessive reactive power, while undercompensation can cause excessive voltage, reducing system stability. The optimal shunt size for this system, with respect to the VSD power factor, was 13 MVAr. The results from the simulation using a PQ-load are presented in Table 3 below, using a 185 mm² subsea cable as a representative case. While this particular cable size was selected as a reference, the same analysis can be performed for any other cable dimension.

Table 3: Power system simulation using PQ-load for 185 mm^2 cable

	Grid	**Step-up Transf.**	**Cable Input**	**Cable Output**	**Motor Input**
Active Power (MW)	9.572	9.445	9.445	8.320	8.195
Reactive Power (MVAr)	0.981	2.035	14.476	4.418	3.396
Cos(ϕ)	0.995	0.978	0.546	0.883	0.924
Apparent Power (MVA)	9.622	9.622	17.284	9.420	8.871
Current (kA)	0.861	0.127	0.227	0.127	0.854
Voltage (kV)	6.454	44.021	44.021	42.863	5.996
U_n **(kV)**	6.6	6.6/45	45	45	6
U/U_n **(p.u.)**	0.977	0.98	0.98	0.95	1.00

These results validate the system's behavior under idealized PQ-load conditions and provide a benchmark for comparing more detailed and integrated simulations. The shunt reactor compensated approximately 12.44 MVAr for this system. To assess the electrical loading across key components in the system, Table 4 summarizes the percentage loading of the power system components during operation.

Table 4: Power System component loading

Component	**Loading**
Step-up Transformer	79 %
Cable (185 mm^2)	84 %
Step-down Transformer	79 %

The loading distribution confirms that all components operate within their rated capacities, ensuring system stability and power delivery efficiency.

3.3 Motor Parameter Estimations

In this thesis, a generic high-voltage induction motor was selected from the ABB High Voltage Induction Motors technical catalog [35]. While not specifically designed for subsea applications,

the motor is considered adequate for the purposes of this study. The equivalent circuit parameters required for motor EMT steady state analysis and validation of the variable speed drive were not provided in the catalog. Normally, these parameters would be determined through no-load and locked-rotor tests. However, as the physical motor was not available, the parameters were estimated using available catalog data through MATLAB.

3.3.1 Estimation of equivalent circuit parameters

The provided parameters are presented in Table 5.

Table 5: Induction Motor parameters

Parameters	Values
Rated shaft power: P_r	8 MW
Rated voltage: U_s	6000 V
Rated current: I_s	861 A
Rated frequency: f	50 Hz
Synchronous speed: n_s	3000 RPM
Rotor speed: n_r	2988 RPM
Efficiency at 100% load: η	97.5%
Efficiency at 75% load: η	97.6%
Power factor at 100% load: PF	0.92
Power factor at 75% load: PF	0.92
Nominal torque: T_n	25567 Nm
No-load current: I_0	147 A

There are several different methods for estimating the equivalent circuit parameters. However, since the focus in this thesis wasn't to specifically estimate these values, a relatively simple estimation method was chosen [36]. Starting with the given variables and utilizing Equation 2.3, the slip was calculated for 100% load to 0.4%. In addition, by combining multiple estimation methods for the squirrel cage induction motor, various parameters was determined. The proposed sequence for estimating these parameters is as follows [36]:

1. Calculate R_s according to the method proposed by Guimarães'.
2. Estimate P_c and P_{fw} with Lee's method.
3. Determine R_r by using Natarajan-Misra's (NM) method.
4. Calculate remaining parameters X_s, X_r, R_c and X_m using Haque's iterative procedure.

Beginning with Guimarães' method, the stator resistance was calculated using the current and slip for three load points, 100%, 75% and 50% load. However, since only two load points were provided in the technical catalog, the current was assumed to vary linearly. The method is based on the steady-state power balance of an induction machine, where the input power is equal to the sum of the output power, losses in the stator and rotor, and other losses such as core and mechanical losses. Stray load losses are neglected in this analysis. The total losses can thus be represented as the sum of stator copper losses and constant losses. Using this balance, the following expression is derived:

$$3R_sI_s^2 \ + \ P_{const} = P_o\left(\frac{1}{\eta} \ - \ \frac{1}{1-s}\right), \tag{3.1}$$

where P_0 is the output power, η is the efficiency, and s is the slip at the corresponding operating point. The right-hand side of the equation represents the difference between input power (accounting for efficiency) and rotor input power, isolating the combined losses. Furthermore, to find the slip at the different operating points, the following expression was used:

$$s = 0.5\left(1 - \sqrt{1 - 4s_{rated}(1 - s_{rated})\frac{P_o}{P_r}}\right), \tag{3.2}$$

where P_o is the shaft power for each operating point and P_r is the rated shaft power. To then estimate the losses in the machine, several standard percentages were used for the different types of losses. Around 14% of total losses at full-load were due to friction and windage. Stray-load losses were estimated following IEEE Standard 112, which assumes these losses to be 0.9% of the input power. Knowing these losses, the airgap power could be calculated according to below equation:

$$P_{ag} = \frac{P_o + P_{fw} + P_{sll}}{1 - s} \tag{3.3}$$

Where P_{fw} is the friction and windage losses and P_{sll} is the stray load losses. Once the airgap power was known, the core losses could be calculated according to below equation:

$$P_c = P_{in} - P_{ag} - 3R_sI_s^2 \tag{3.4}$$

With all losses known, the rotor resistance was calculated according to Natarajan-Misra's (NM) method as per below equation [36]:

$$P_o\left(\frac{1}{\eta} - 1\right) = 3I_s^2(R_s + R_r) + P_c \ \ \Rightarrow \ \ R_r = P_o\frac{\left(\frac{1}{\eta} - 1\right) - P_c}{3I_s^2} - R_s \tag{3.5}$$

The remaining parameters X_s, X_r, X_m and R_c were all calculated using Haque's iterative method. However, since the stator resistance, rotor resistance and constant losses was already known. The only equation of interest was the total reactance. Both X_s and X_r was chosen to have a fixed ratio of X_s/X_r according to the NEMA rating of the motor. However, due to the rating not being known, this thesis will assume NEMA rating A. This means the reactances was chosen to be $X_s = X_r = 0.5X_{tot}$ [36]. The total reactance was given by the below equation:

$$X_{tot} = X_s + X_r = \sqrt{\left(\frac{V_s}{I_{st}}\right)^2 - (R_s + R_r)^2} \tag{3.6}$$

Where I_{st} is the starting current which for this motor is 5.9 times larger than the nominal value. Furthermore, the rotor induced voltage and rotor current are given by below equations

$$E = V_s - I_s Z_s \tag{3.7}$$

$$I_r = I_s - \frac{E}{Z_m} \tag{3.8}$$

Where V_{ph} is the phase voltage and I_{ph} is the phase current. However, since the value for the magnetizing impedance Z_m is unknown, the rotor current is estimated to $I_r = I_s \cdot PF$. Furthermore, with the induced rotor voltage and rotor current known, the magnetizing reactance was calculated according to the reactive power balance equation below [37]:

$$X_m = \frac{E^2}{V_s I_s sin(\theta) - I_s^2 X_s - I_r^2 X_r} \tag{3.9}$$

The value for θ was calculated from the power factor: $\theta = cos^{-1}(PF)$. Finally the core resistance could be calculated by assuming it to be half the constant losses as per below equation [37]:

$$R_c = \frac{E^2}{0.5 P_c} \tag{3.10}$$

By using all the above equations, the equivalent circuit parameters for the Induction Machine was calculated. The values can be seen in Table 6 below.

Table 6: Equivalent circuit parameters

Parameters	**Values**
Stator resistance: R_s	0.0235 Ω
Rotor resistance: R_r	0.0282 Ω
Stator reactance: X_s	0.59 Ω
Rotor reactance: X_r	0.59 Ω
Magnetizing reactance: X_m	29.579 Ω
Core resistance: R_c	799 Ω

3.3.2 Validation of estimated parameters

Since numerous approximations were made during the estimation of the equivalent circuit parameters, the calculated values may not be entirely accurate. Moreover, no exact reference values were available for direct comparison. Therefore, to assess whether the parameters were reasonable they were inserted into the Induction Machine equivalent circuit, as shown in Figure 3. The corresponding performance values provided in the technical catalog were then derived from the circuit model for validation. The input voltage used in the circuit was the line to line voltage of 6000 V. Moreover, the core resistance was neglected due to the resistance being so high. Impedances for the stator, rotor and magnetizing branch was calculated as per below equations:

$$Z_s = R_s + jX_s \tag{3.11}$$

$$Z_r = \frac{R_r}{s} + jX_r \tag{3.12}$$

$$Z_m = jX_m \tag{3.13}$$

The stator current was then calculated by using the total impedance of the circuit. Moreover, the rotor current was calculated by focusing on the induced voltage at the rotor side and rotor impedance as per below equations:

$$I_s = \left| \frac{V_s}{Z_{total}} \right| = \left| \frac{V_s}{Z_s + Z_{parallel}} \right| = \left| \frac{V_s}{Z_s + \frac{Z_m \cdot Z_r}{Z_m + Z_r}} \right| \tag{3.14}$$

$$I_r = \left| \frac{E}{Z_r} \right| = \left| \frac{V_s - I_s Z_s}{\frac{R_r}{s} + jX_r} \right| = \left| \frac{V_s - I_s(R_s + jX_s)}{\frac{R_r}{s} + jX_r} \right| \tag{3.15}$$

Once the current had been calculated, it was possible to calculate the power factor from the stator current in complex form as per below:

$$I_s = I_s^{real} + jI_s^{imag} \quad \Rightarrow \quad \theta = tan^{-1}\left(\frac{Im(I_s)}{Re(I_s)}\right) \quad \Rightarrow \quad PF = cos(\theta) \tag{3.16}$$

The input power to the equivalent circuit was then calculated by:

$$P_{in} = \sqrt{3} V_s I_s \ \cdot \ PF \tag{3.17}$$

Furthermore, the air-gap power is determined by calculating the total power transferred over from the stator side to the rotor side and is given by below equation:

$$P_{ag} = \sqrt{3} I_r^2 \frac{R_r}{s} \tag{3.18}$$

The losses in the machine was calculated in a similar way as when estimating the equivalent circuit parameters, except the stator and rotor copper losses was also added as per below equations:

$$P_{cu,s} = \sqrt{3} R_s I_s^2 \tag{3.19}$$

$$P_{cu,r} = \sqrt{3} R_r I_r^2 \tag{3.20}$$

Once the copper losses for both stator and rotor was calculated, the total losses could be determined:

$$P_{loss} = P_{cu,s} + P_{cu,r} + P_{core} + P_{sll} + P_{fw} \tag{3.21}$$

Knowing all the losses, air-gap power and input power, it was possible to also calculate the shaft power and the efficiency using the rated slip of 0.4% from the catalog:

$$P_{shaft} = P_{ag}(1 - s) - P_{loss} \tag{3.22}$$

$$\eta = \frac{P_{shaft}}{P_{in}} \tag{3.23}$$

Once the above parameters were known, it was possible to calculate some parameters provided in the catalog. However, to further validate the equivalent circuit parameters, the torque-speed curve for the motor was also plotted to see how the torque varied with slip. By using Equation 2.9 from the Thevenin equivalent circuit, it was possible to determine the torque at different slip. A simple load curve was also added according to equation 2.50. This was added to see where the load line intercepts induction motor curve. The result is shown in below Figure 18.

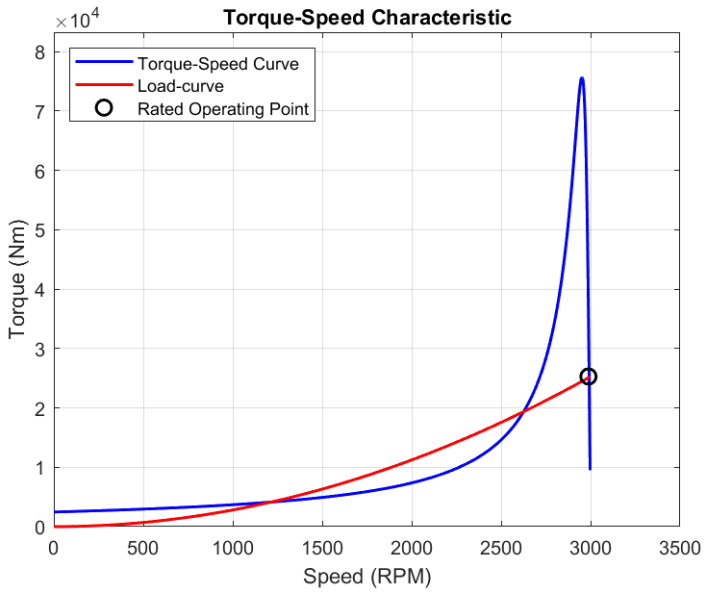

Figure 18: Torque-speed curve including load curve

Using the above Figure 18, it was also possible to determine rated torque, maximum torque and starting torque to further investigate how valid the estimations were. Calculations were also done for the operating point at 75% load to verify whether the efficiency and power factor is similar to the catalog values. The slip was also recalculated using Equation 3.2 to 0.3%. Table 7 shows a summary of all calculated parameters from the equivalent circuit compared to the catalog and how much they deviate.

Table 7: Comparison between catalog values and calculated values

Parameters	**Technical catalog**	**Equivalent circuit**	**Deviation**
Current: I_s	861 A	858.3 A	0.3%
Shaft power: P_{shaft}	8 MW	8.0446 MW	0.5%
Input power: P_{in}	8.205 MW	8.241 MW	0.4%
Efficiency at 100% load: η	97.5%	97.617%	0.12%
Efficiency at 75% load: η	97.6%	97.628%	$\approx 0\%$
Power factor at 100% load: PF	0.92	0.924	0.43%
Power Factor at 75% load: PF	0.92	0.911	1%
Nominal Torque: T_n	25567 Nm	25283 Nm	1.12%
Max Torque/Nom. Torque: T_{max}/T_n	2.8	3	7.1%
Starting Torque: T_s/T_n	0.4	0.15	62.5%

The comparison between catalog values and the calculated values from the equivalent circuit shows a high degree of accuracy across all parameters. Most deviations remain well below 1% except the

starting torque and maximum torque. The starting torque deviates by a large margin, suggesting that something is either wrong with the calculation or estimations. Could, also be because the Thevenin equivalent circuit only takes steady-state into account. Overall, the model can be considered validated for use in further system simulations in steady state.

3.4 Cable AC Resistance Estimation

One key aspect of this analysis is assessing the Ferranti effect, which occurs in long, lightly loaded transmission lines and results in a voltage increase at the receiving end due to the capacitive nature of the cable. Additionally, the current flow, voltage drops, and reactive power compensation requirements are examined to understand how different cable sizes influence system performance. These effects are quantified and compared in the results section. Another important parameter is the AC resistance which can be calculated by first determining the DC resistance using Equation 3.24 below [38].

$$R_{\mathrm{DC}} = \frac{\rho L}{A} \tag{3.24}$$

where ρ is the resistivity of the conductor, L is the conductor length, and A is the cross-sectional area. To estimate the AC resistance, we account for additional losses due to skin and proximity effects. This is shown in Equation 3.25 below.

$$R_{\mathrm{AC}} = R_{\mathrm{DC}}(1 + y_s + y_p) \tag{3.25}$$

where y_s and y_p are the skin and proximity effect correction factors, respectively. The skin effect factor, y_s is calculated using the following equation:

$$y_s = \frac{x_s^4}{192 + 0.8x_s^4} \tag{3.26}$$

and x_s^4 can be calculated using Equation 3.27 below.

$$x_s^4 = \left(\frac{8\pi f_c}{R_{DC}} k_s \cdot 10^{-7}\right)^2 \tag{3.27}$$

For a cable arranged in an equilateral triangular configuration, the skin effect factor is $k_s = 1$. The proximity effect factor is then calculated as follows:

$$y_p = \frac{x_p^4}{192 + 0.8x_p^4} \left(\frac{d_c}{s}\right)^2 \left[0.312 \left(\frac{d_c}{s}\right)^2 + \frac{1.18}{\frac{x_p^4}{192+0.8x_p^4} + 0.27}\right] \tag{3.28}$$

where d_c is the diameter of the conductor and s is the center-to-center distance between the conductor axes where both values are found in the cable datasheet. The factor x_p^4 can be calculated similarly to x_s^4 using Equation 3.29 below.

$$x_p^4 = \left(\frac{8\pi f_c}{R_{DC}} k_p \cdot 10^{-7}\right)^2 \tag{3.29}$$

For a round, stranded, and non-impregnated cable, the proximity effect coefficient is taken as $k_p = 1$. To apply this estimation method, the system is analyzed using four sizes of ABB XLPE submarine three-core cables with a lead sheath, rated for a nominal voltage of 45 kV (max 52 kV) [39]. The relevant parameters including current ratings, MVA ratings, capacitance, inductance, and calculated AC resistance, are listed in Tables 9.

Table 8: Thermal ratings of three-core submarine cables (copper conductor) at 45 kV nominal voltage, 20°, 1m laying depth

Size (mm^2)	**Current rating** (A)	**MVA rating** (MVA)
150	375	28.2
185	420	32.7
240	480	37.4
300	540	42.0

Table 9: ABB XLPE three-core lead sheath cable parameters

Size [mm^2]	**Capacitance** [μF]	**Inductance** [mH]	**AC Resistance** [Ω/km], **20 C°, 50 Hz**
150	0.21	0.40	0.1134
185	0.22	0.39	0.0925
240	0.24	0.37	0.0722
300	0.26	0.36	0.0587

3.5 VSD Design

The control method selected for investigation in this thesis is open-loop voltage over frequency (V/f) control, where both the output voltage and frequency of the VSD are varied proportionally. This method was primarily chosen due to the practical difficulties associated with obtaining feedback from pump motors located on the seabed. The long traveling distance from the sensors located on the seabed will deteriorate the signal and the controller will get more noise. Furthermore, if there's any problems with the sensor, maintenance or replacement is a huge problem. Hence open loop control was preferred since no sensors on the motor are required. To illustrate the behavior of the motor under varying operating conditions, a torque-speed characteristic was simulated for multiple frequencies while maintaining a constant V/f ratio for the motor used in this thesis. The curve was plotted using the torque equation 2.9 from Thevenin equivalent circuit. Where the starting torque for each frequency was calculated by setting the slip to 1:

$$T_{start} = \frac{3V_{th}^2}{(R_{th} + R_r)^2 + (X_{th} + X_r)^2} R_r \frac{1}{w_s} \tag{3.30}$$

The curve is shifted when the frequency is decreased and increased due to the speed as per below Figure 19.

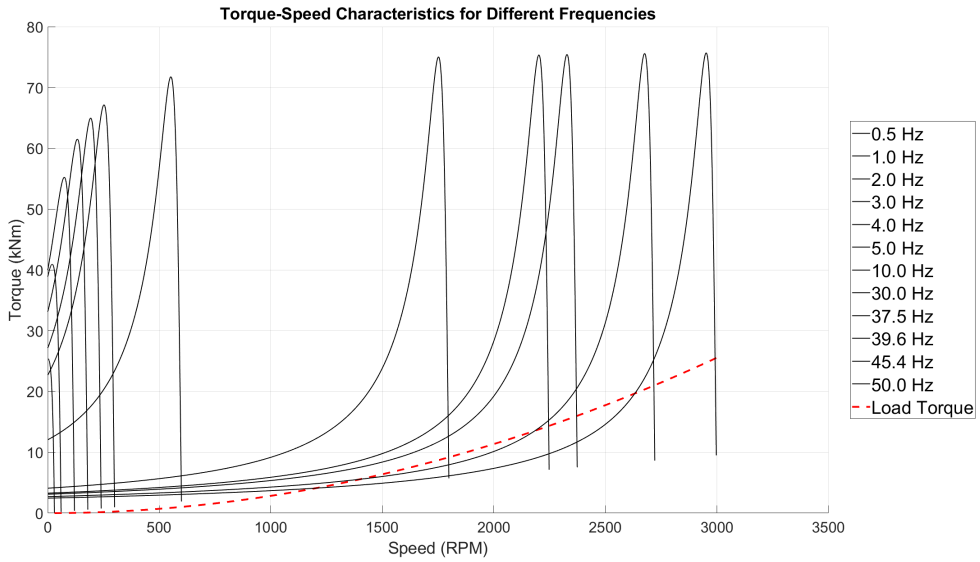

Figure 19: Torque-speed for different frequencies

Where the curve furthest to the right is the nominal torque-speed curve at 50 Hz. The operation points is where the load torque curve intercepts the torque-speed curve for the motor at different frequencies. When the frequency is increased, the curve shifts to the right and when it's decreased, it's shifted to the left. This is the behavior that the control system was designed to replicate.

The open-loop V/f control system is designed to take a reference input, which is usually specified as either the desired frequency or the target rotational speed of the motor. This input acts as the main driver for how the voltage is determined. Using a predefined V/f characteristic, the system calculates the appropriate voltage that matches the input frequency. Typically, this characteristic is linear, meaning that as the frequency increases, the voltage is scaled up proportionally.

To improve performance at very low speeds, the system can also include a voltage boost. This boost helps to overcome the higher electrical resistance experienced during startup or low-speed operation, ensuring that the motor gets enough torque to start smoothly without stalling. This is especially important because, at low frequencies, the motor's impedance is much higher, and it requires extra voltage to generate the needed magnetic flux.

Once the voltage level is determined, it is converted into sinusoidal waveforms. These waveforms are then compared against a high-frequency carrier wave in a PWM (Pulse Width Modulation) modulator. This comparison process generates the PWM signals that control the gate of each transistor in the inverter. The switching action of these transistors allows the inverter to produce AC power with the correct voltage and frequency to drive the motor. The blanking time of the inverter was not considered.

Finally, these modulated voltage and frequency signals are fed into the motor through the VSD, which regulates the power delivery according to the reference settings. This enables the motor to operate smoothly at the specified speed, maintaining the voltage-to-frequency ratio as designed. An example of an open-loop V/f control system can be seen in Figure 20 below, illustrating how each stage of the process is interconnected.

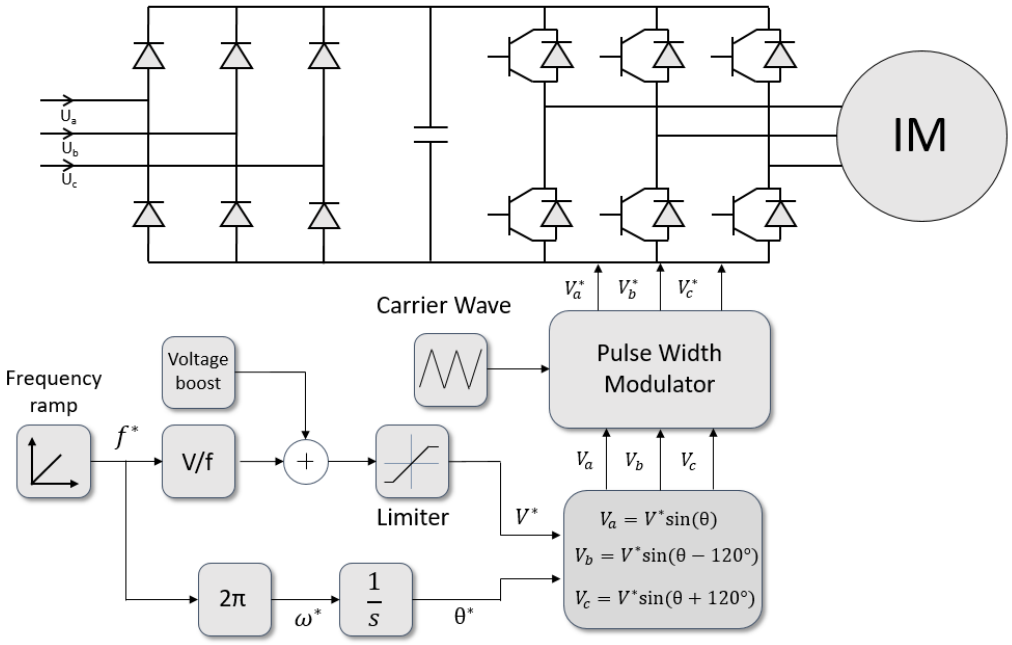

Figure 20: Open loop V/f control block diagram

The Variable Speed Drive model was implemented within the DIgSILENT Simulation Language (DSL) environment. DSL is a language specifically designed for dynamic modeling and control system implementation within power system simulations. It enables the creation of custom models for control loops, power electronics, and various system components by allowing the user to define logic in block-diagrams or code-based form. In this thesis, only steady-state operation will be evaluated hence no ramping function is needed for the frequency and voltage. The input was chosen to only be the frequency that corresponds to the operation point that's being evaluated.

The design of the open-loop V/f control began with the implementation of a custom DSL frame, which is where the control logic was defined. Within this frame, a block diagram representing the control strategy was created. The input of the control system was the desired output frequency as the primary input, from which it calculates the required output voltage using a constant V/f ratio. Additionally, the angular position needed for generating the sinusoidal reference signals was computed by integrating the angular frequency, as shown in Equation 3.31.

$$\theta = \int \omega \, dt = \int 2\pi f \, dt \tag{3.31}$$

To determine the output voltage amplitude of the inverter, the modulation index, P_m, had to be calculated. This index defines the relationship between the fundamental AC output voltage and the DC-link voltage and is important in ensuring the inverter produces the desired output voltage. Using the relationship between line-to-line RMS voltage and the DC-link voltage, the modulation index was derived as follows:

$$V_{LL,\text{rms}} = \sqrt{3} \cdot \frac{V_{ph,\text{peak}}}{\sqrt{2}} = \sqrt{3} \cdot \frac{\frac{V_{DC}}{2} \cdot P_m}{\sqrt{2}} = \frac{\sqrt{3} \cdot P_m V_{DC}}{2\sqrt{2}} \Rightarrow m = \frac{2\sqrt{2} V_{LL,\text{rms}}}{\sqrt{3} V_{DC}} \tag{3.32}$$

Here, V_{DC} refers to the DC-link voltage, and $V_{LL,rms}$ is the line-to-line RMS voltage determined from the V/f relationship. Once the modulation index and the angle θ were determined, the next step was to generate the three-phase sinusoidal signals. These signals represent the control references for each of the three inverter legs. The amplitude of these signals is defined by the modulation index P_m, while their phase angles are offset by 120° to match the standard three-phase distribution. The generated signals are calculated as follows:

$$u_a = \frac{1}{2} + \frac{P_m}{2} \sin(\theta)$$

$$u_b = \frac{1}{2} + \frac{P_m}{2} \sin\left(\theta - \frac{2\pi}{3}\right)$$

$$u_c = \frac{1}{2} + \frac{P_m}{2} \sin\left(\theta + \frac{2\pi}{3}\right)$$

In these equations, the 0.5 offset ensures that the signals oscillate between 0 and 1 instead of -1 and 1. This adjustment was necessary because the inverter logic in PowerFactory interprets the signals based on their absolute magnitude compared to a fixed threshold of 0.5.

The switching logic used for the PWM inverter in PowerFactory is quite simple yet effective. Each control signal u_a, u_b, and u_c is continuously monitored and compared against the threshold of 0.5. When the control signal exceeds 0.5, the inverter connects the corresponding phase leg to the positive side of the DC bus. If the control signal falls below 0.5, the leg switches to the negative side of the DC bus. This logic is represented mathematically as follows:

$$S_a = \begin{cases} 1 & \text{if } u_a > 0.5 \\ 0 & \text{if } u_a \leq 0.5 \end{cases}$$

$$S_b = \begin{cases} 1 & \text{if } u_b > 0.5 \\ 0 & \text{if } u_b \leq 0.5 \end{cases}$$

$$S_c = \begin{cases} 1 & \text{if } u_c > 0.5 \\ 0 & \text{if } u_c \leq 0.5 \end{cases}$$

The sinusoidal nature of u_a, u_b, and u_c ensures that each phase is switching in a coordinated manner, providing a smooth three-phase waveform to the motor. This is what drives the motor efficiently and in synchronization with the desired speed and torque characteristics. This logic is further utilized when Sinusoidal PWM is tested. After the open-loop V/f control structure was established, the model was implemented in PowerFactory as demonstrated in Figure 21.

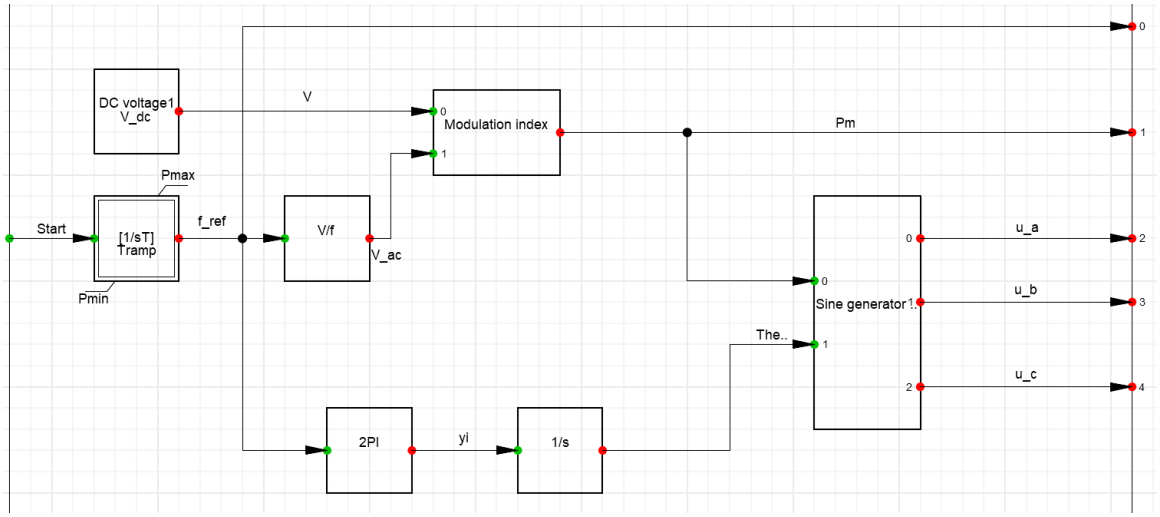

Figure 21: Open-loop V/f control model implemented in DSL

Where each of the blocks were manually created and initialized using DIgSILENT Programming Language (DPL) within each block. The input of the control system is as previously mentioned the desired frequency as well as the DC-voltage to determine the amplitude modulation index. To verify the functionality of the control strategy, an initial test system was created consisting of a DC voltage source, a PWM inverter modeled as a controlled voltage source and an induction motor. This simple setup allowed for validating the response of the control block to dynamic input changes and assessing the correctness of voltage generation. The test system is shown in below Figure 22.

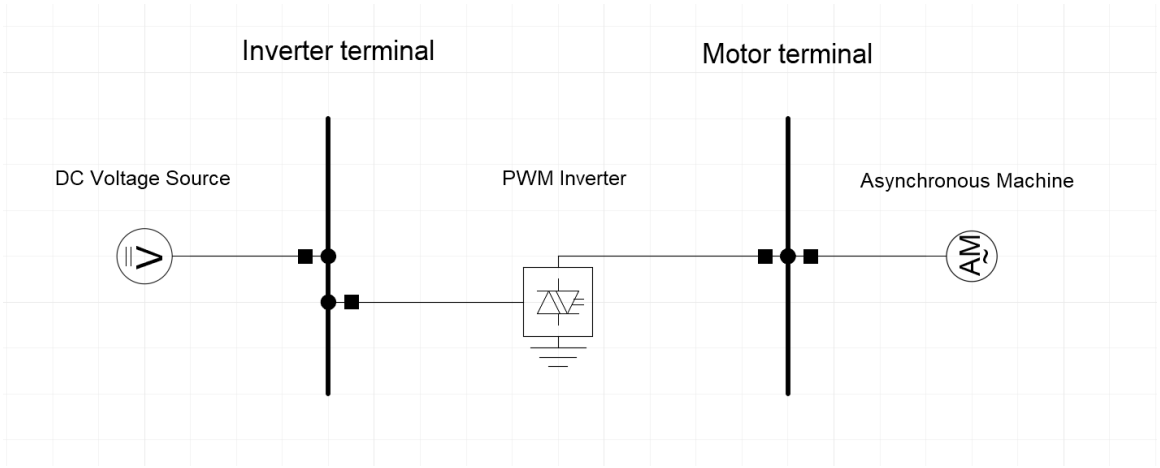

Figure 22: Test setup for the VSD control system

Furthermore, to integrate the developed VSD into the test simulation, a Composite Model Frame was utilized. This framework enables the grouping of multiple dynamic elements, including the PWM inverter, the induction machine, the control system and a load torque model into a single reusable component. These components can be connected in several different ways using the predefined inputs and outputs of the PowerFactory models. The output of the control system that was connected to the inverter was the input frequency, amplitude modulation index as well as the reference voltages to the three legs of the inverter. Moreover, the output of the motor was the speed in radians/s which

was then connected to a custom MDM3 model which was designed according to Equation 2.50 and it's shown in below Figure 23.

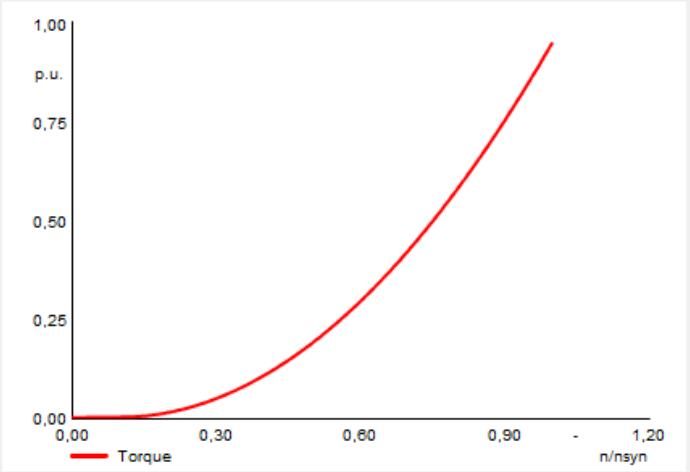

Figure 23: MDM3 Load torque curve

Usually, at low speeds the load torque is higher due to the stiction torque. This is something to be taken into consideration when implementing voltage boost at low speeds and the ramping of the voltage and frequency. However, since the startup of the motor won't be investigated in this thesis, the load torque curve was designed to be purely quadratic. This load torque curve was then fed back to the motor and the complete structure of the composite model is illustrated in Figure 24.

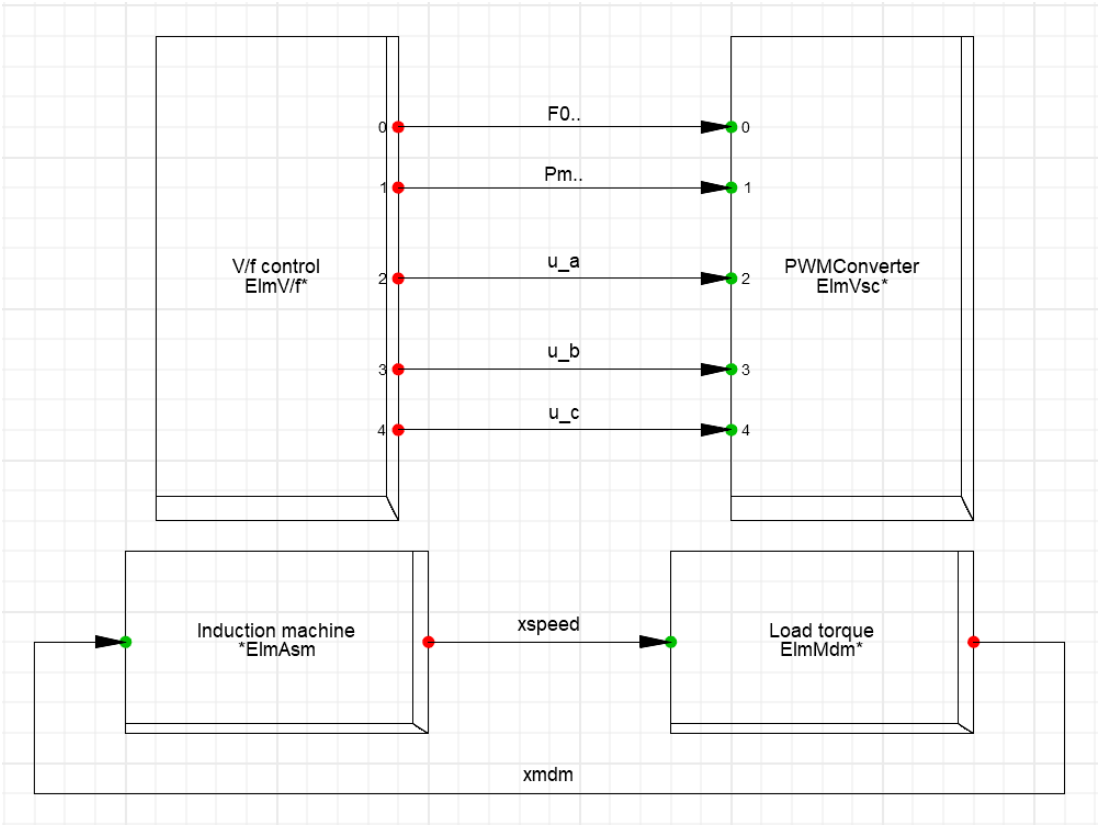

Figure 24: Composite Model Frame for the VSD

By then assigning all the components to a slot in the composite model frame using their respective component name, it was possible to dynamically change the output voltage and frequency of the inverter. While the open-loop V/f control applied the voltage-frequency relationship at the VSD output, the downstream effects of the long cable, transformers, and system impedance introduce additional voltage drops and variations before reaching the motor terminals. These were not corrected within the control system but were instead investigated through system-level simulation at different operating points (100%, 75%, and 50% load). By verifying that the motor terminal voltage and VSD output voltage aligned with the expected V/f profile at each point.

4 Results

This section presents the results from both steady-state load flow analysis and dynamic EMT simulations. The load flow analysis focuses on evaluating system performance across different cable sizes and operating points, while the EMT simulations evaluate motor and inverter performance at various loads.

4.1 Load Flow

Load flow simulations are carried out to analyze how the power system behaves under different cable sizing and loading scenarios. Key electrical parameters such as active and reactive power, voltage, current, and power factor are monitored at various points along the power transmission path—from the VSD to the motor.

4.1.1 Cable sizing simulations

To determine the optimal cable size for system performance, four different cable cross-sections were tested to assess the trade-offs between power losses, voltage regulation, and the Ferranti effect. These simulations were carried out under nominal operation with 50 Hz. The input to the motor is the electric power which is 8.205 MW determined from the motor technical specification. The sizes tested were 150 mm^2, 185 mm^2, 240 mm^2, and 300 mm^2 and their corresponding simulation results are shown in Tables 8 through 11 below.

Table 10: Power system simulation using 150 mm^2 cable

	VSD	**Step-up Transf.**	**Cable Input**	**Cable Output**	**Motor Input**
Active Power (MW)	9.551	9.429	9.429	8.330	8.205
Reactive Power (MVAr)	0.113	1.141	-13.715	4.398	3.386
Cos(ϕ)	1.000	0.993	0.567	0.884	0.924
Apparent Power (MVA)	9.552	9.498	16.644	9.420	8.876
Current (kA)	0.844	0.124	0.217	0.127	0.854
Voltage (kV)	6.535	44.257	44.257	42.878	5.999
U_n **(kV)**	6.6	6.6/45	45	45	6
U/U_n **(p.u.)**	0.99	0.98	0.98	0.95	1.00

From Table 10, it is evident that the expected voltage of 6 kV is achieved at the motor terminals. Additionally, the motor's performance parameters closely align with the values specified for rated operation in Table 5. The power factor at the grid side is notably high, with a value of almost 1, reflecting the effect of the compensating reactor. In contrast, the power factor at the cable input is comparatively low and the negative sign of the reactive power flow at the cable input confirms a net capacitive behavior The voltage at the cable's receiving end drops to 42.878 kV, compared to the sending end voltage of 44.257 kV, reflecting the expected resistive losses along the cable length.

Table 11: Power system simulation using 185 mm^2 cable

	VSD	**Step-up Transf.**	**Cable Input**	**Cable Output**	**Motor Input**
Active Power (MW)	9.399	9.273	9.273	8.330	8.205
Reactive Power (MVAr)	1.068	2.110	-14.251	4.398	3.385
Cos(ϕ)	0.994	0.975	0.545	0.884	0.924
Apparent Power (MVA)	9.459	9.510	17.003	9.420	8.876
Current (kA)	0.857	0.126	0.226	0.127	0.855
Voltage (kV)	6.370	43.488	43.488	42.844	5.994
U_n **(kV)**	6.6	6.6/45	45	45	6
U/U_n **(p.u.)**	0.97	0.97	0.97	0.95	1.00

The 185 mm^2 cable introduces some noticeable changes in the results, particularly concerning reactive power consumption. The motor performance remains consistent with that of the 150 mm^2 cable, achieving the expected 6 kV at the motor terminals, with other parameters matching the rated values for nominal operation. However, the power factor at the grid side, representing the VSD output in these simulations, decreases slightly, from 0.567 to 0.545. This is due to increased reactive power consumption caused by the cable's higher charging capacitance. While the shunt reactor partially compensates for this effect, it is not sized to fully eliminate reactive power, and could theoretically be adjusted to achieve a power factor closer to unity.

The thicker cable also reduces active power losses thanks to its lower resistance. However, the increased capacitance amplifies the Ferranti effect, requiring a larger reactor to maintain voltage stability. This highlights a trade-off in cable sizing: while thicker cables reduce resistive losses, they demand stronger reactive compensation due to their capacitive nature.Table 12 presents the power system parameters for a 240 mm^2 cable.

Table 12: Power system simulation using 240 mm^2 cable

	VSD	**Step-up Transf.**	**Cable Input**	**Cable Output**	**Motor Input**
Active Power (MW)	9.252	9.151	9.151	8.330	8.205
Reactive Power (MVAr)	2.779	3.907	-15.591	4.409	3.385
Cos(ϕ)	0.958	0.920	0.506	0.884	0.924
Apparent Power (MVA)	9.699	9.950	18.078	9.425	8.876
Current (kA)	0.910	0.135	0.245	0.127	0.855
Voltage (kV)	6.150	42.660	42.660	42.841	5.994
U_n **(kV)**	6.6	6.6/45	45	45	6
U/U_n **(p.u.)**	0.93	0.95	0.95	0.95	1.00

Examining the results for the 240 mm^2 cable reveals a continuation of the observed trend, where reactive power consumption increases with the cable's cross-sectional area, most likely due to the higher charging currents. The power factor at the grid side decreases further to 0.958, with a similar reduction observed at the cable input. A key difference compared to the smaller cables is the voltage behavior at the cable's receiving end, where it rises from 42.66 kV to 42.841 kV, driven by the increased capacitance of the cable. The voltage increase can become problematic in lightly loaded or unbalanced systems if not properly compensated. Despite this, the cable still supplies the motor with the correct voltage, and the remaining motor parameters remain consistent with rated values.

Table 13: Power system simulation using 300 mm^2 cable

	Grid	**Step-up Transf.**	**Cable Input**	**Cable Output**	**Motor Input**
Active Power (MW)	9.248	9.082	9.082	8.328	8.205
Reactive Power (MVAr)	4.561	5.846	-17.369	4.412	3.398
Cos(ϕ)	0.897	0.841	0.463	0.884	0.924
Apparent Power (MVA)	10.311	10.801	19.600	9.424	8.881
Current (kA)	0.992	0.147	0.267	0.126	0.846
Voltage (kV)	6.000	42.367	42.367	43.296	6.063
U_n **(kV)**	6.6	6.6/45	45	45	6
U/U_n **(p.u.)**	0.91	0.94	0.94	0.96	1.01

The largest tested cable shows the most prominent Ferranti effect, characterized by significant reactive power consumption and a substantial voltage rise at the cable's receiving end, increasing from 42.367 kV to 43.296 kV. Correspondingly, the power factor at the grid side drops further, mirroring the behavior observed at the cable input and continuing the trend of increased reactive power with larger cable sizes.

Another important consideration is the loading of the components at maximum operating conditions. The objective is to maintain loading levels below 100% to prevent overheating and minimize losses. For larger cable sizes, the rise in reactive power contributes to higher loading on the system components. A recommended target is around 80% loading for transformers, providing a safe margin from the rated apparent power and enhancing reliability. The calculated loading percentages for the various components are presented in Table 14 below.

Table 14: Power system component loading for different cable sizes

Component	**Loading 150 mm^2**	**Loading 185 mm^2**	**Loading 240 mm^2**	**Loading 300 mm^2**
Step-up Transformer	77%	79%	84%	92%
Cable	80%	84%	91%	99%
Step-down Transformer	79%	79%	79%	78%

As mentioned before, when the cross-sectional area increases, the cable loading increases due to the increased reactive power which can be seen from Table 14. Step-up transformer loadings also increase with larger cables due to the effect of the increased reactive power. The step-down transformers remain relatively stable across different cable sizes due it having a constant reactive power for all different cable sizes. A visual representation of voltage and current behavior across different cable lengths for each cable size are presented in Figures 25 and 26 below.

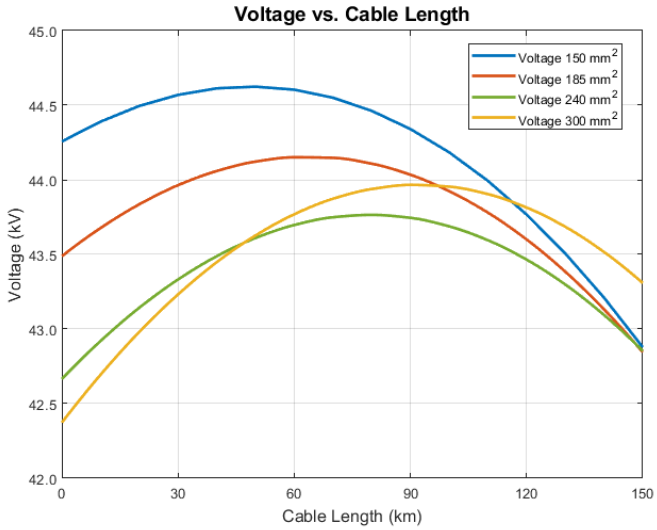

Figure 25: Cable length vs voltage for various cable sizes

Figure 25 shows that the Ferranti effect becomes more pronounced with increasing cable size. For the 240 mm^2 and 300 mm^2 cables, voltage at the receiving end exceeds the sending end voltage, caused by excessive reactive power from the cable capacitance. The sending end (at 0 km) corresponds to the topside grid bus, where the VSD output and the shunt reactor are connected. Furthermore, the voltages for the 150 mm^2 and 185 mm^2 are higher initially at the sending end which is expected due to higher AC resistance. At first glance, this seems counterintuitive, as higher resistance typically results in a larger resistive voltage drop. However, in this case, the voltage at the receiving end remains lower for the smaller cables due to their reduced capacitive charging current. The apparent higher voltage at the sending end is a result of less voltage rise caused by the Ferranti effect, not an actual gain due to resistance. This highlights that the dominant factor here is not resistive voltage drop, but rather the degree of reactive power generated by the cable's capacitance and its effect on voltage profiles.

As the cable length increases the 150 mm^2 voltage initially increases to around 44.6 kV which is rather close to the rated value of 45 kV. At around 50 km it starts to decrease, showing the largest voltage drop out of all the cables. Moreover, the 185 mm^2 cable have a smaller voltage drop and the maximum voltage it reaches is around 44.1 kV which is a larger margin to the rated voltage. To ensure a fair comparison, all cases use the same Thevenin voltage at the grid-side bus and the same MVAr-rated shunt reactor, both connected at the sending end. The observed voltage behavior is therefore attributed entirely to differences in cable resistance and, more significantly, in cable capacitance.

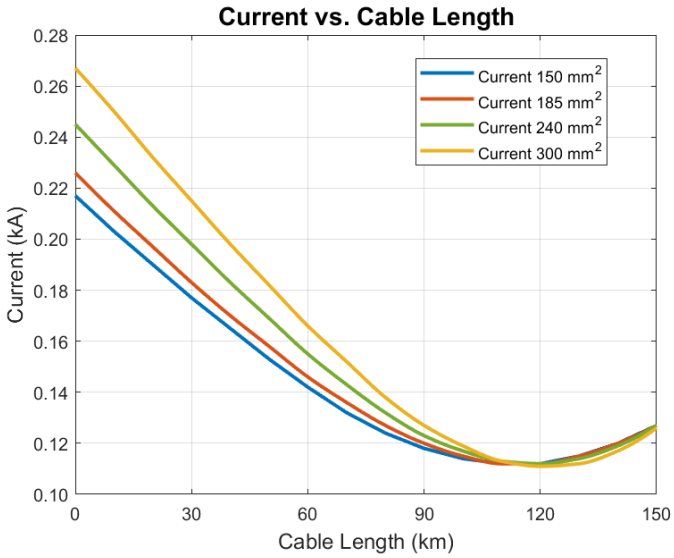

Figure 26: Cable length vs current for various cable sizes

As expected, larger cable sizes at the sending end initially have higher current due to charging and capacitive current components. This is also evident from Figure 26, where the cables with higher cross sectional area at the sending end have higher currents. However, since the capacitance of the cable increases with the cable length, the current profile also varies due to the distributed capacitance of the cables. The variation is more pronounced for larger cables for which the capacitance is higher. This is especially evident for the larger cross sectional areas where the currents at the receiving end are lower or similar to the smaller cables. This is expected due to the capacitive charging effect which causes a voltage rise as per Figure 25.

From this analysis, it is clear that cable sizing presents a trade-off, where the resistance decreases, but the current increases due to the capacitive effects, which results in the losses possibly being higher for larger cables. The results for the 150 mm^2 and 185 mm^2 cables do not exhibit a voltage rise at the receiving end, making them the two most suitable candidates. Both cables maintain voltages that are relatively close to the rated value of 45 kV, with minimal differences between them in terms of voltage and current profiles. However, the 185 mm^2 cable demonstrates the smallest voltage drop while maintaining a good margin to the rated voltage. Therefore, the 185 mm^2 cable was selected as the optimal choice for this system, ensuring stability without significant voltage rise or reactive power challenges.

4.1.2 Operation Under Varying Load Conditions

Since the 185 mm^2 cable was determined to be the optimal size, it will be standardized and consistently used throughout this report from now on. To further evaluate the overall stability of the power system, different load operation points are tested. In addition to the previously simulated 100% load case (Table 11), simulations are conducted for 75% and 50% load conditions. The load points were chosen as representative partial-load scenarios based on fractions of the rated shaft power of the induction motor, which is 8 MW. These conditions allow assessment of the system's performance under realistic variations in operational demand.

To determine the operating frequency corresponding to each load point, the following relationship between shaft power and rotational speed was used, as shown in Equation 4.1.

$$P_{shaft} = T \cdot w = kw^3 \Rightarrow f = \sqrt[3]{\frac{P_{shaft}}{k}} \cdot \frac{1}{2\pi} \tag{4.1}$$

Here, P_{shaft}, is the mechanical shaft power, T is the torque, ω is the angular velocity and k is the pump constant. Using $\omega = 2\pi f$ the frequency can be calculated to be 45.4 Hz for the 75% load and 39.6 Hz for the 50% load.

The entire system seen from the VSD to the motor can be viewed as an impedance which changes with the frequency of the VSD output. However, PowerFactory does not dynamically change the reactances of the transformers and cable when running a Load Flow. This only changes when running simulations in the time-domain. So these had to be manually changed to the calculated frequency for each operation point. Furthermore, the grid frequency was also changed for each instance. The motor frequency was kept constant at its nominal value since there was no visible changes when manually changing it. Hence, it was kept at its nominal value. The results for 75% and 50% load levels are presented in Tables 15 and 16, respectively.

Table 15: Load flow results with VSD at 75% load

	Grid	**Step-up Transf.**	**Cable Input**	**Cable Output**	**Motor Input**
Active Power (MW)	6.835	6.755	6.755	6.128	6.043
Reactive Power (MVAr)	0.035	0.674	-10.524	3.271	2.548
Cos(ϕ)	1.000	0.995	0.540	0.882	0.921
Apparent Power (MVA)	6.835	6.788	12.505	6.946	6.558
Current (kA)	0.682	0.100	0.184	0.104	0.700
Voltage (kV)	5.788	39.170	39.170	38.530	5.412
U/U_n **(p.u.)**	0.88	0.87	0.87	0.86	0.90

Table 16: Load flow results with VSD at 50% load

	VSD	**Step-up Transf.**	**Cable Input**	**Cable Output**	**Motor Input**
Active Power (MW)	4.484	4.437	4.437	4.076	4.025
Reactive Power (MVAr)	0.986	0.535	-6.976	2.239	1.777
Cos(ϕ)	0.977	0.993	0.537	0.876	0.915
Apparent Power (MVA)	4.592	4.469	8.267	4.651	4.400
Current (kA)	0.518	0.075	0.140	0.080	0.537
Voltage (kV)	5.115	34.205	34.205	33.541	4.732
U/U_n **(p.u.)**	0.77	0.76	0.76	0.75	0.79

The results for the varying operating load points presented in Tables 15 and 16 are consistent with theoretical expectations when considering the torque-speed relationship defined in Equation 2.50 and the requirement of constant V/f for the motor. This means that as the mechanical load decreases from 100 % to 75 % and 50 %, both the active and apparent power requirements at the motor input are expected to reduce, as reflected in the simulation data.

For the 75 % load condition in Table 15, a reduction in active power from 8 MW at 100 % load, shown in Table 16, to 6.043 MW is observed at the motor input. Similarly, at 50 % load, the active power further drops to 4.025 MW. This trend is also reflected in the reactive and apparent power values, which decrease accordingly with reduced load conditions.

Moreover, the current and voltage values adapt to the changes in load, with lower current demands observed at the grid and motor input under lighter loading. This behavior confirms that the system scales correctly and maintains operational stability across a range of load conditions.

The variation in power factor (Cos(ϕ)) for the 50% load point is also expected. At reduced loads, reactive power becomes a more significant component relative to active power, slightly lowering the power factor in some parts of the system. However, this can be explained by examining how reactive power behaves in the system. In long cables, reactive power generation is primarily capacitive and approximated by $Q_c \propto V^2 \omega C$, while the inductive component is proportional to $I^2 \omega L$. At partial load, the current decreases significantly, reducing the inductive voltage drop and the associated reactive losses. Moreover, at the motor input, the power factor remains relatively high (above 0.90), indicating efficient operation even at partial loads. To further evaluate the power system att different loads the component loadings are summarized in Table 17.

Table 17: Power system component loading at 75% and 50% system load (185 mm^2 cable)

Component	**Loading at 100%**	**Loading at 75%**	**Loading at 50%**
Step-up Transformer	79%	63%	47%
Cable (185 mm^2)	84%	58%	52%
Step-down Transformer	79%	65%	50%

The results show that the transformer loadings decrease with reduced system load, while the cable experiences a more noticeable drop in loading, especially at 50%. This is primarily due to the lower current associated with reduced active power demand. However, another possible contributing factor is the voltage reduction resulting from V/f control, which lowers the system voltage at partial loads. Since cable reactive power generation is proportional to $V^2 \omega C$, the decreased voltage also reduces reactive power flow, further diminishing cable loading.

Between these two effects, reduced active power flow (affecting current) and lower voltage (affecting reactive power), both contribute meaningfully to the observed drop in cable loading, though the drop in active power typically has a more immediate impact due to its direct influence on current magnitude. Still, the role of reduced voltage in limiting reactive power flow becomes increasingly relevant at lower load points.

4.2 VSD design results

To evaluate how well the control system worked, a steady state Electromagnetic Transients simulation of the induction motor for different frequencies was performed. The setup used for the VSD testing is the same as in Figure 22 where the chosen DC-voltage was 10 kV, so the modulation factor is approximately 1 using Equation 3.32. Since PowerFactory uses the p.u. system for many of the parameters, a summary of all the base values are given in Table 18 below.

Table 18: Base values used for per-unit calculations

Quantity	Symbol	Value	Unit
Base Voltage (line-to-line RMS)	U_{base}	6000	V
Base Frequency	f_{base}	50	Hz
Base Angular Speed	ω_{base}	312.87	rad/s
Base Mechanical Speed	n_{base}	2988	rpm
Base Shaft Power	P_{base}	8	MW
Base Apparent Power	S_{base}	8.918	MVA
Base Reactive Power	Q_{base}	3.418	MVAr
Base Current	I_{base}	861	A
Base Torque	T_{base}	25567	Nm

At 2 seconds a parameter event was added where the nominal frequency was changed to 45.4 Hz with a slope of approximately 2 Hz/s in the input of the DSL model to analyze if the output voltage of the inverter, speed and torque of the induction motor responded as expected. While the value of 2 Hz/s isn't necessarily the most optimal value, it was just chosen to see how the motor responded and to see if the expected values are reached. The results of the EMT simulation is shown below in Figures 27-29.

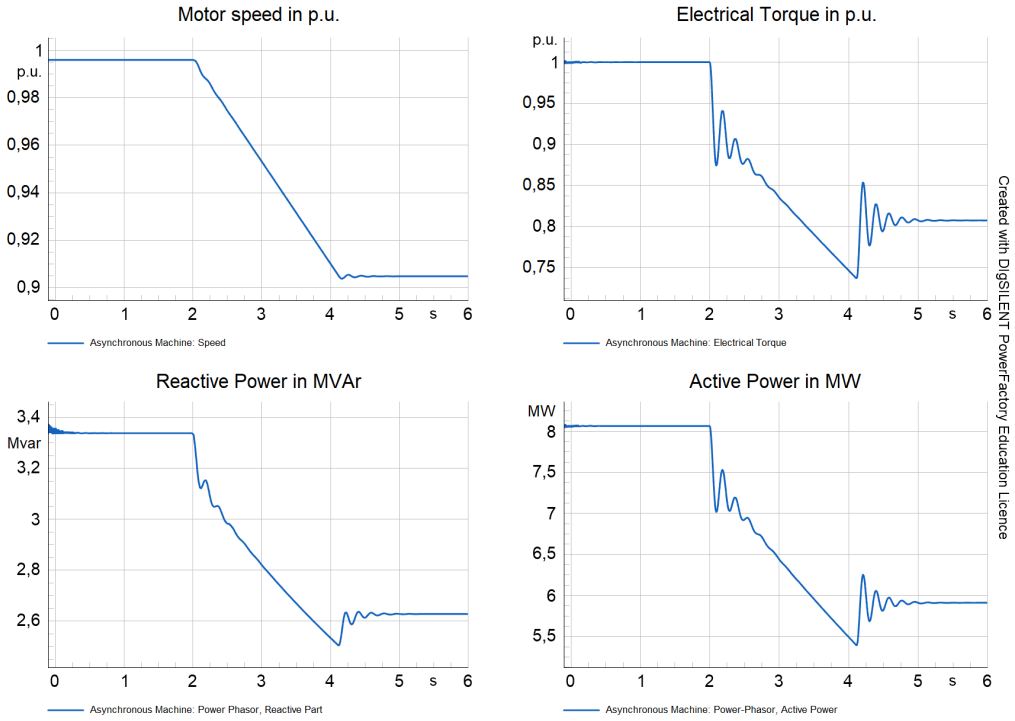

Figure 27: Induction machine speed, torque, active power and reactive power

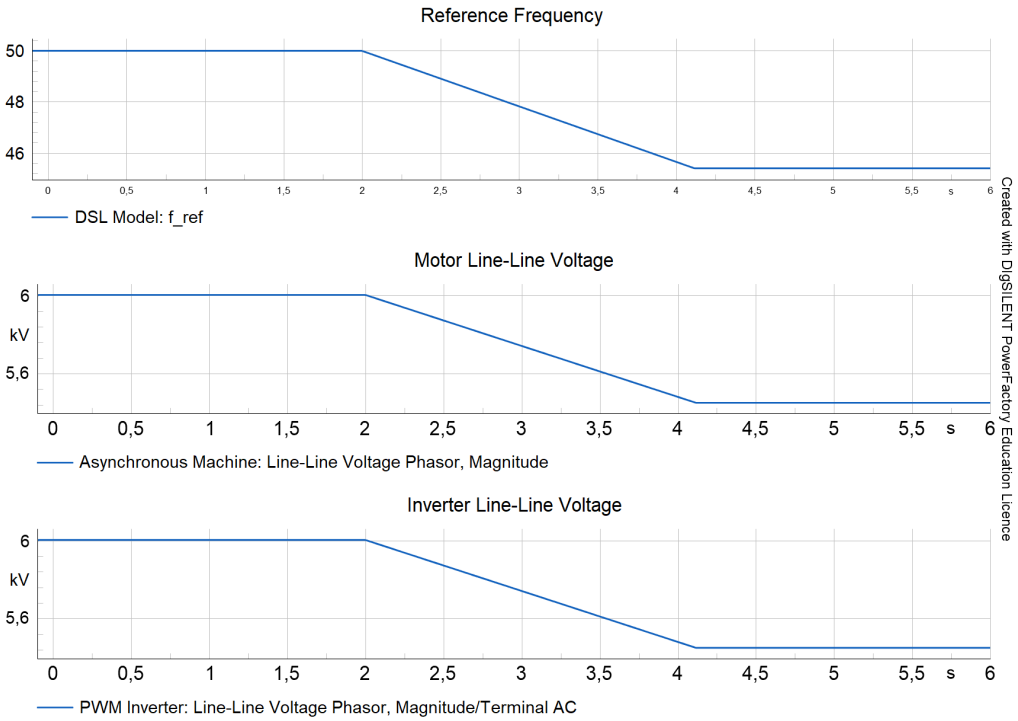

Figure 28: Reference frequency and Line-Line voltages

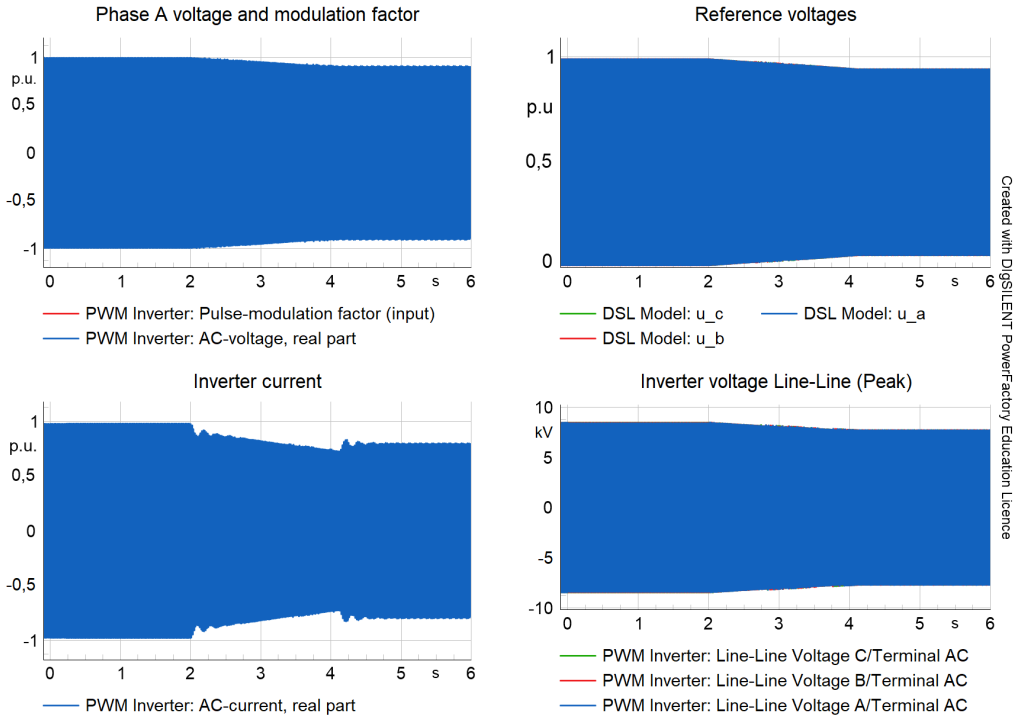

Figure 29: Inverter output voltage, current and control signals

As can be seen from above Figures, at 2 seconds the inverter responds to the frequency change by lowering the modulation factor and voltage. The expected theoretical speed at 45.4 Hz is approximately 0.91 p.u. and torque is expected to be around 0.82 p.u. following the load torque curve operating points. As can be seen by Figure 27, the speed after the frequency step is 0.905 p.u. and the torque is 0.8074 p.u. Which is almost perfectly aligned with the theoretical expectations of 0.908 p.u. for the speed and close to 0.8246 p.u. for the torque. The small deviation could be because of load torque model or the estimated induction machine parameters. Regarding the active power for 45.4 Hz, the expected value is approximately 6 MW as seen in Table 15. The active power of the induction machine as seen from the plot is 5.91 MW which is a little bit lower than expected. The current also decreases as expected after the frequency change. Initially it oscillates and after a while it decreases to approximately 685 A which is a little bit lower than the current seen in Table 15.

The control system behaves as expected in steady-state dynamically, the voltage and frequency changes after the input frequency to the DSL model is changed to 45.4 Hz. The ramping from 50 to 45.4 Hz worked relatively well even though there are some oscillations that are visible. The ramping can be further optimized with damping for the torque oscillations. The current also remains within limits not exceeding 1 p.u.

4.3 EMT simulations at different operating points

The topside VSD is connected to the power system and the resulting schematic is shown in Figure 30 below. However, when the VSD is connected to the power system, conventional load flow analysis cannot be performed due to the dynamic nature of the drive and its control system. This means that just changing the input frequency to the open loop V/f control system won't change anything when doing a load flow simulation. As a result, time-domain simulations are used to capture the motor's steady-state behavior under different loading conditions with the control system. The following subsections present the results of these simulations under various operating load points.

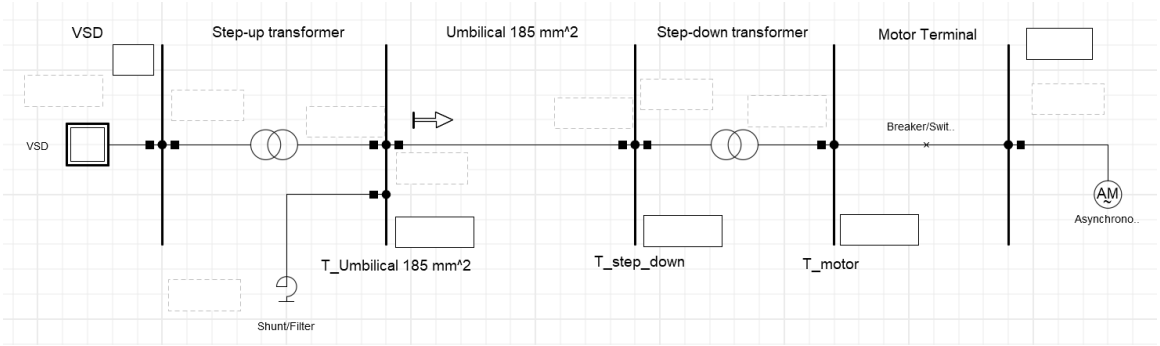

Figure 30: Entire power system including the VSD

4.3.1 100% load steady state

Under the 100% load condition, the system's dynamic response is expected to align with the previously shown load flow results in Table 11. Figure 31 displays the motor voltage and current, showing initial transients and steady-state stabilization during 100% load.

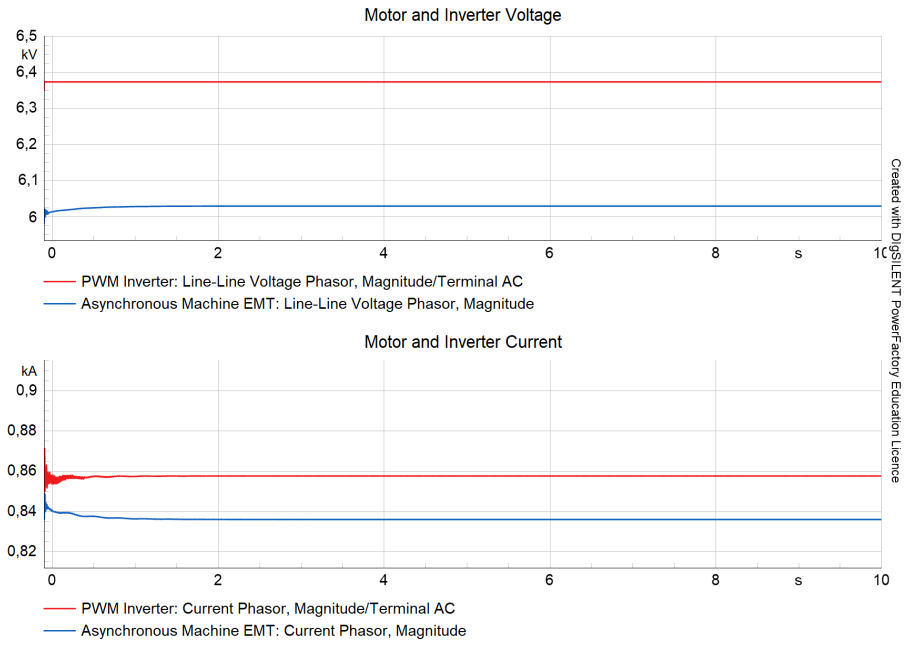

Figure 31: Motor and inverter voltage and current response at 100% load

The motor voltage stabilizes just below 6.03 kV after 1 second with minimal fluctuation, indicating a well-regulated supply under full loading conditions. This also corresponds to the load flow results for 100% load presented in Table 11, with a motor input voltage around 6 kV. The motor current exhibits a brief oscillation and quickly settles just under 0.836 kA. The slightly lower current compared to the 0.855 kA in Table 11 is expected, as the simulation reflects mechanical output power, which results in a lower current than the electrical input used in the load flow analysis. To further illustrate the motor's behavior during steady state, the key dynamic variables are presented graphically. The dynamic responses of the motor are shown in Figure 32 below.

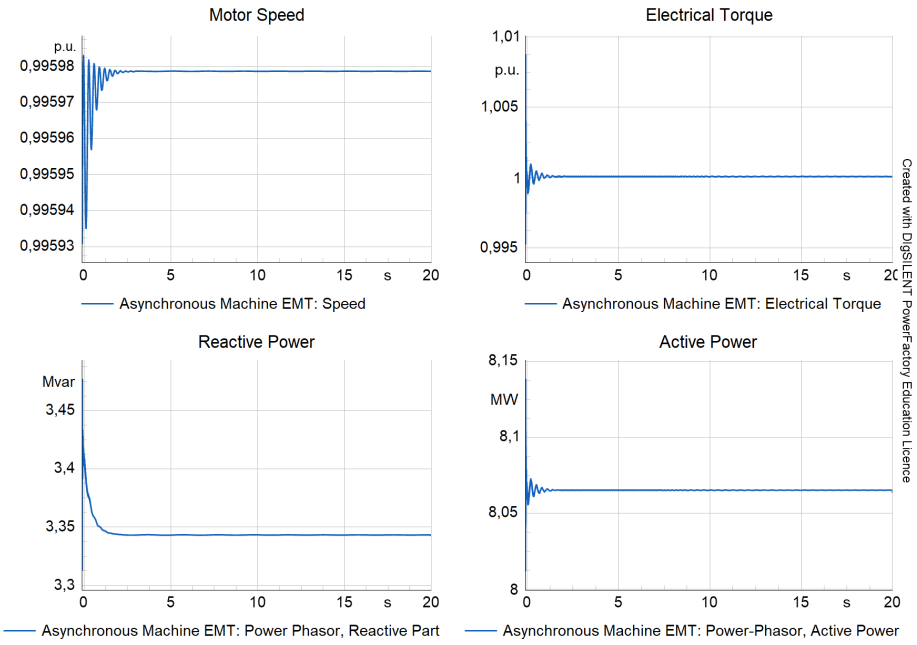

Figure 32: Time-domain simulation at 100% load, showing speed, torque, and power settling after initial transients.

Initially at t = 0, there are some oscillations for all the results, these oscillations are expected even in steady state due to initialization of the PowerFactory models. Once the oscillations has settled, the motor speed remains very close to 1 p.u., confirming that the machine operates near synchronous speed with minimal slip under full load which is consistent with the theoretical expectations. Similar to the speed, the torque response shows a brief period of oscillation similar to the rest of the results, after which it quickly settles at exactly 1.0 p.u. and this indicates that the machine is successfully delivering its rated torque. Furthermore, active power stabilizes at about 8.06 MW, and reactive power settles around 3.34 MVAr, both with minimal transient disturbances. These values also correspond closely to the load flow results in Table 11. Furthermore, the power factor calculated is 0.923 which also aligns with the previous load flow results.

Moreover, to assess the inverter's performance in supplying the rest of the system in steady state, the voltage, current, and reference signals at the inverter output are simulated. The inverter is set as a controlled voltage source to initially simulate ideal conditions similar to the VSD design validation. This is to avoid switching effects and it gives a more clear comparison between the reference signals and system response. The input to the inverter for the 100% load case is 50 Hz and the results of the voltage, current and reference signals are shown in Figure 33.

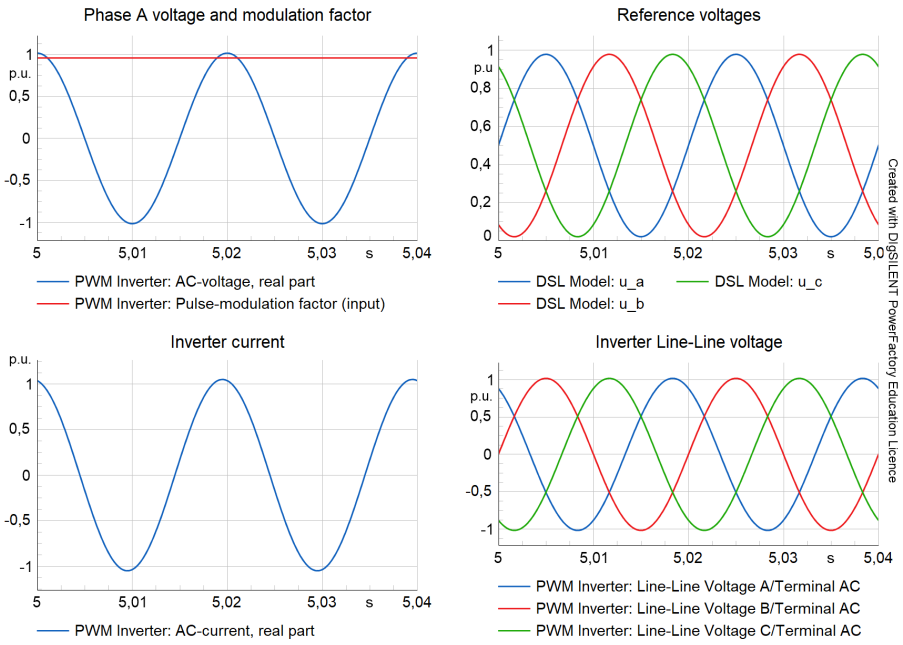

Figure 33: Inverter voltage, current, and reference voltages at 100% load and 50 Hz.

The plots in Figure 33 shows the inverter output voltage real part as a clean, sinusoidal waveform with a stable amplitude. The red line represents the amplitude modulation factor decided by the open loop V/f control system. The voltage plot also shows a period of around 0.02 seconds which yields a frequency of 50 Hz which is appropriate for the 100% load. Furthermore, the output voltage reaches approximately 1 p.u. which is the desired result. Since the inverter is used as a controlled voltage source, there's no distortion or transients. The current waveform is also sinusoidal and steady, indicating a well-regulated current at 100% load. The three-phase reference voltages maintain consistent amplitude and 120° phase separation, validating the correct operation of the modulation control and balanced inverter output.

Furthermore, to investigate how the transformers behave for the different operating points, the magnetic flux is observed. Since V/f control is used, the flux is expected to remain constant for both the step-up transformer and step-down transformer. The subplots in Figure 34 below shows the three-phase magnetizing flux components (A, B, and C) of both the step up and step down transformers. The top graphs display the start of the steady state simulation, while the bottom zoomed-in graphs show detailed flux waveforms between 1.9 and 2.0 seconds.

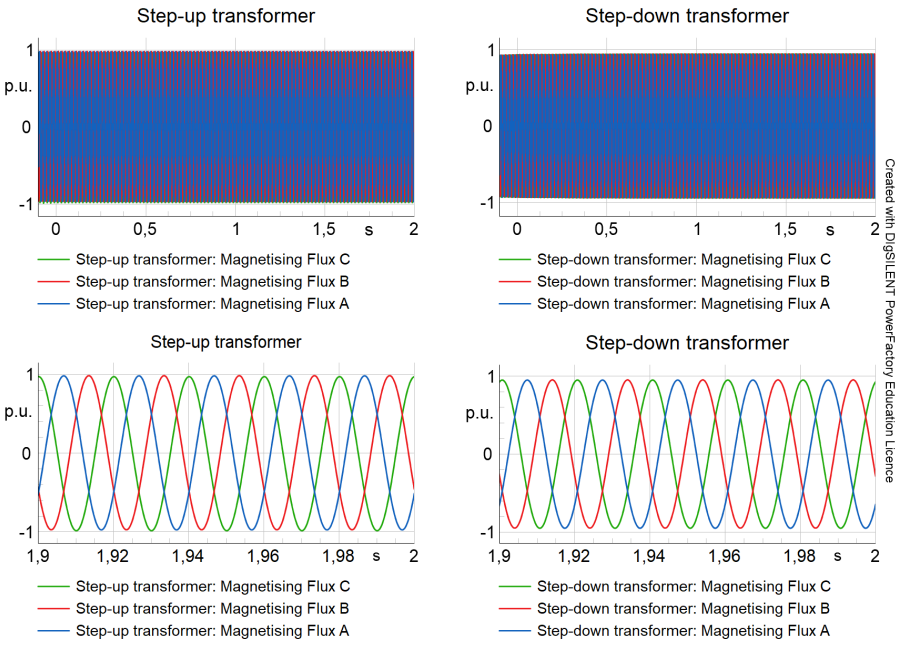

Figure 34: Magnetizing flux of step-up and step-down transformers under full load operation.

At 100% load, the magnetizing flux remains stable and balanced across all phases while maintaining a sinusoidal waveform which indicates that the V/f control works. With the transformers operating under ideal conditions at full load, the cable behavior is also evaluated to see how effectively the power is being delivered through the cable. Figure 35 shows the cable parameters at 100% load flow.

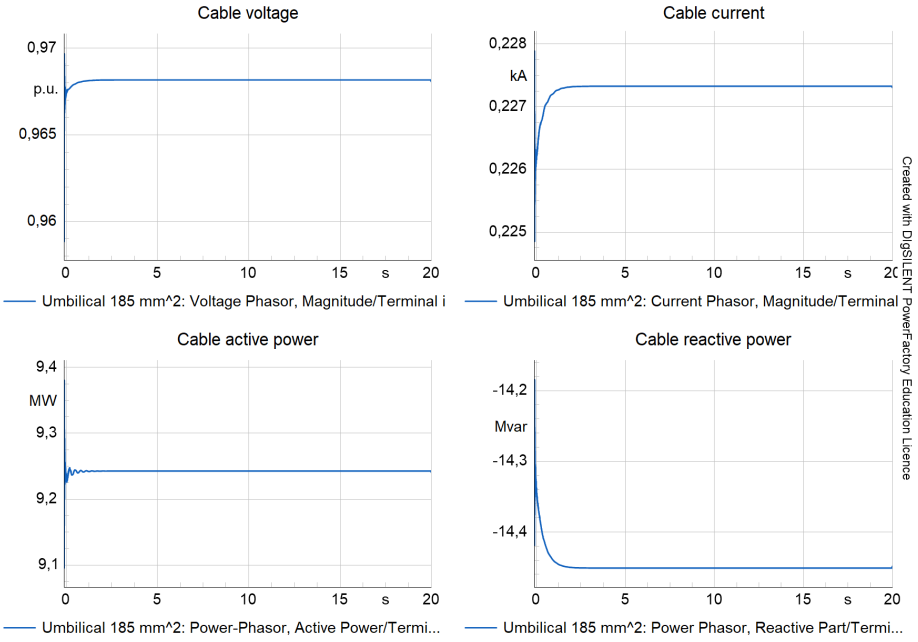

Figure 35: Cable voltage, current, and power results at 100% load

The voltage in the cable in Figure 35 shows a quick settlement just above 0.965 comparing closely with the load flow result of 0.97 p.u. from Table 11. The current stabilizes just above 0.227 kA, aligning with cable input current noted in Table 11. The active and reactive power both align closely with compared with the load flow results around 9.24 MW and 14.5 MVAr, respectively.

4.3.2 75% load steady state

To evaluate the system's performance under partial loading, the operating condition at 75% of the rated load is analyzed. The input frequency to the power system is now 45.4 Hz and similarly with 100% load, the motor voltage and current responses are first presented.

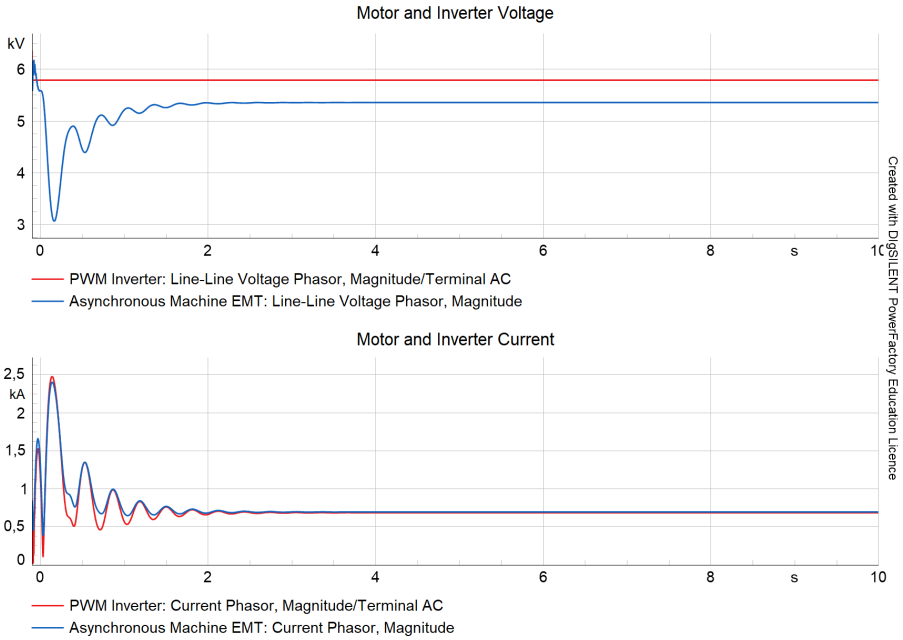

Figure 36: Motor and inverter voltage and current response at 75% load

At 75% load, the motor voltage stabilizes around 5.45 kV after two seconds, showing more variation than at 100% load in the initialization of the components. The current initially experiences a short transient of nearly 2 kA before settling at 0.685 kA. The steady state voltage and current also compares closely with the load flow results for 75% load shown in Table 15. To further understand motor performance at 75% load, the following plots in Figure 37 illustrate key motor parameters over time.

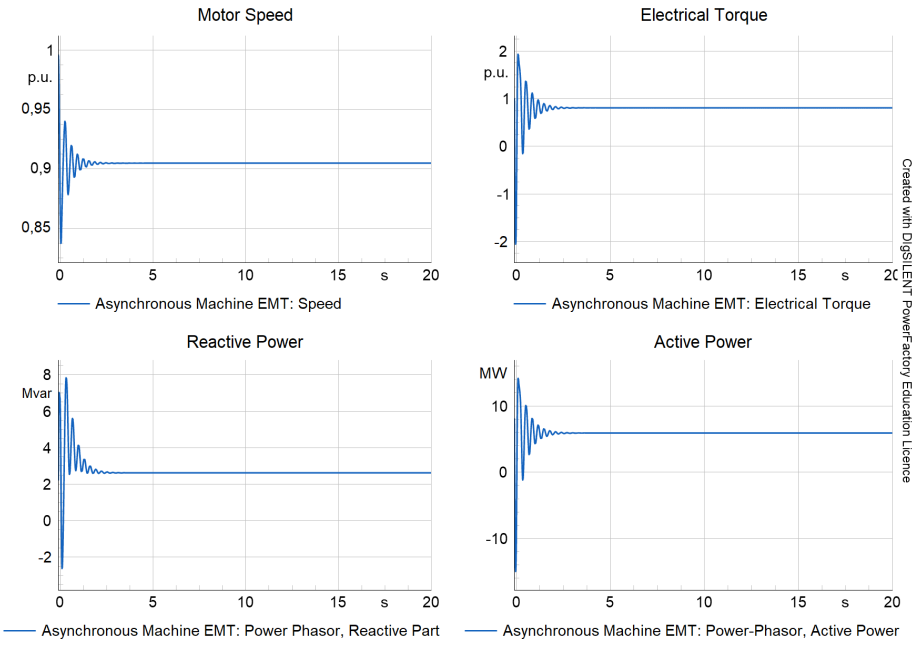

Figure 37: Time-domain simulation at 75% load, showing speed, torque, and power settling after initial transients.

The plots in Figure 37 show the motor's behavior as it transitions to steady-state at 75% load. The speed stabilizes around 0.91 p.u. which aligns with the expected speed at 45.4 Hz. Furthermore, the torque fluctuates briefly before settling at 0.8 p.u., corresponding to the mechanical load. The active power stabilizes near 6 MW, in line with the load. These values correspond to the load flow values in Table 15 and similarly, the reactive power initially peaks around 8 MVAr before stabilizing around 2.5 MVAr which is expected.

This also indicates that the dynamic model of the induction motor, along with the rest of the transmission system in PowerFactory, responds consistently across different frequencies. The simulated values align closely with the load flow results in Table 15, where system frequencies were manually adjusted to match the VSD output voltage.

To further assess the electrical behavior at the inverter side during this operating condition, the following plots illustrate the inverter voltage, current, and reference voltage response to the frequency change.

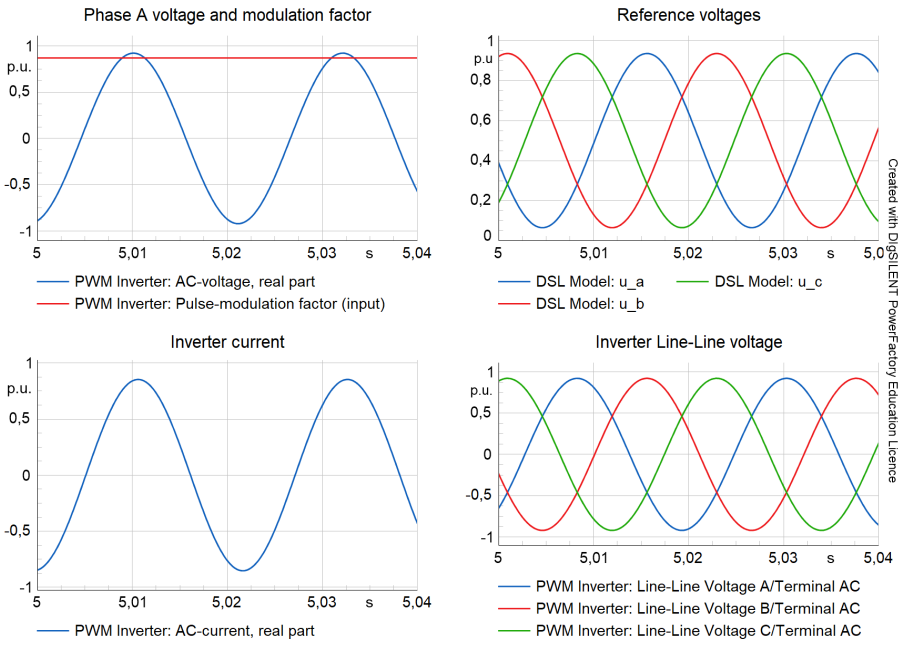

Figure 38: Inverter voltage, current, and reference voltages at 75% load and 45.4 Hz.

Figure 38 shows waveforms with a frequency of 45.4 Hz, confirming accurate frequency tracking by the control system. The output voltage maintains a clean sinusoidal shape despite the reduced frequency and load. The modulation index appears stable, and the waveform closely follows the reference, indicating effective voltage control at partial load. The current waveform remains sinusoidal but has a visibly lower amplitude compared to the 100% load case, reflecting the reduced torque demand. The waveform is clean, and no distortion is observed. The three-phase references remain balanced with a slightly longer period due to the 45.4 Hz setting, as mentioned above. Phase separation and amplitude are consistent throughout the simulation time. In addition to the inverter behavior, Figure 39 presents plots of the magnetic flux response of the transformers under 75% loading conditions.

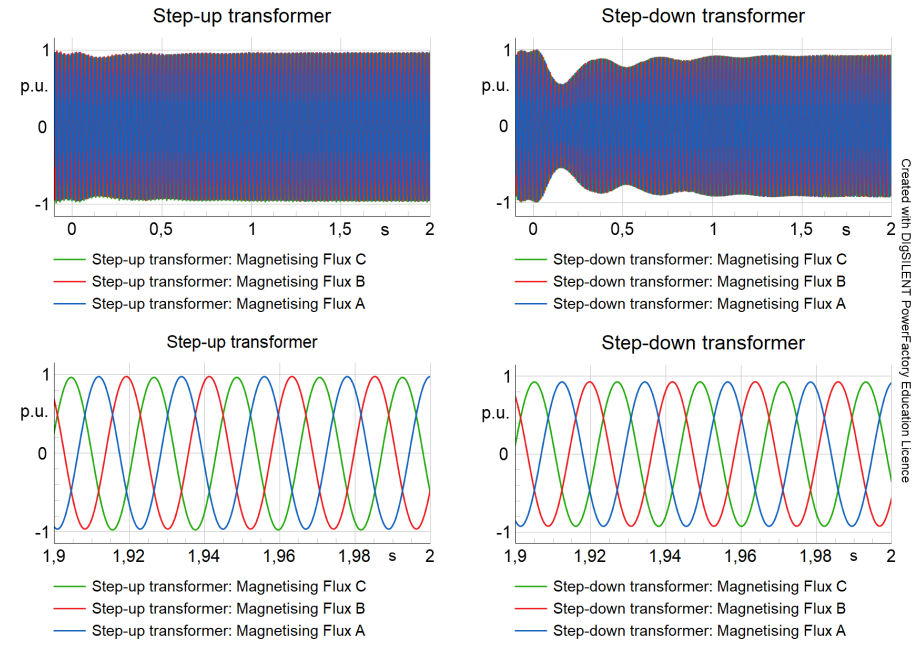

Figure 39: Magnetizing flux of step-up and step-down transformers under 75% load operation

For the partial load, the flux remains sinusoidal and fairly well balanced except in the beginning because of the initialization. After the initial oscillations, the magnetic flux stabilizes close to 1 p.u. for the step-up transformer and the step-down transformer magnetizing flux has decreased slightly and is therefore considered acceptable. The cable parameters at 75% load are also simulated and presented in Figure 40 below.

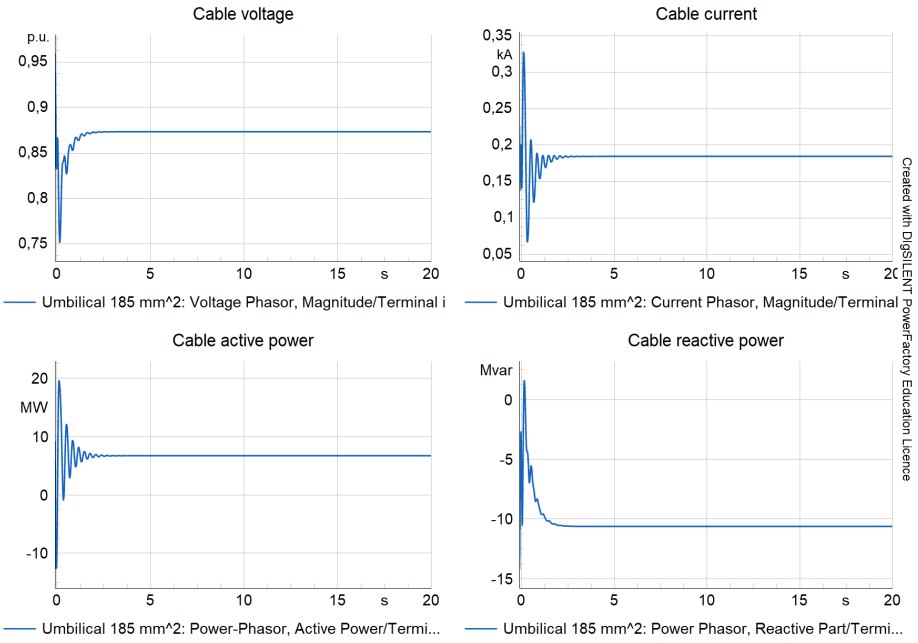

Figure 40: Cable voltage, current, and power results at 75% load

The cable voltage in Figure 40 settles around 0.875 p.u., closely matching the 0.87 p.u. value from the load flow results in Table 15. The current also aligns well, stabilizing near 0.84 p.u. which equals 0.19 kA, relatively consistent with the 0.184 kA value at the cable input from the load flow results. The active power settles just below 7 MW, closely matching the 6.755 MW at the cable input. Reactive power stabilizes around 10.5 MVAr, which corresponds well with the 10.524 MVAr reported in the load flow results.

4.3.3 50% load steady state

The 50% load case represents a further reduction in system demand and is analyzed to investigate the performance limits and potential inefficiencies at low-load conditions. This subsection aims to identify how the electrical parameters and transient dynamics change as the load drops to lower operating levels. The motor voltage and current are presented in Figure 41 below.

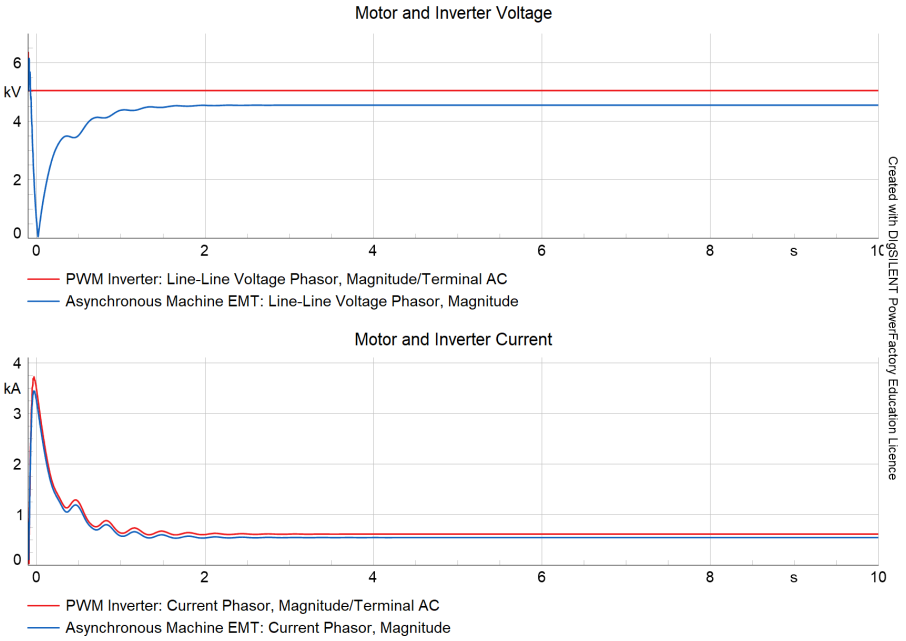

Figure 41: Motor and inverter voltage and current response at 50% load

The motor voltage in Figure 41 reaches a steady value of approximately 4.6 kV after a transient period in the beginning which is a small deviation from the expected 4,73 kV. The motor current initially peaks around 3.5 kA due then gradually settles around 0.53 kA, reflecting the reduced load torque at 50% loading. The current also corresponds well to the load flow results in Table 16. Compared to the 100% and 75% load case, the current at 50% load is lower which is to be expected. Similarly with previous loading points, the motor's behavior during the transition to steady-state at 50% load are presented using the four subplots in Figure 42 below.

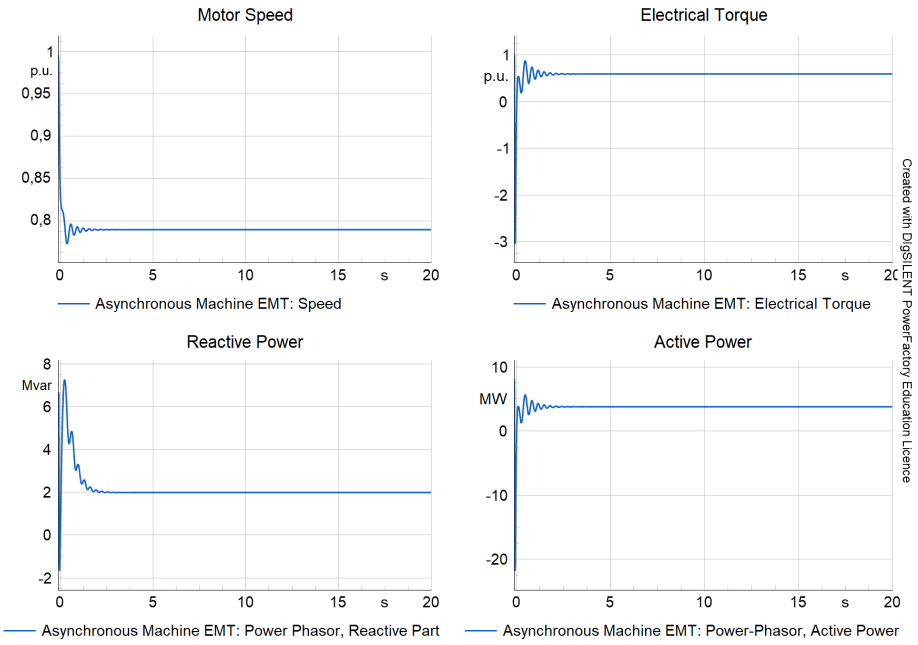

Figure 42: Time-domain simulation at 50% load, showing speed, torque, and power settling after initial transients

The speed stabilizes at approximately 0.79 p.u., indicating reduced load torque compared to nominal. The torque initially oscillates before settling around 0.6 p.u., matching the mechanical load. The active power stabilizes around 3.8 MW, which is a small deviation from the load flow results in Table 16. Similarly, the reactive power peaks initially at over 7 MVAr before decreasing and stabilizing just below 2 MVAr. The inverter parameters are also shown in Figure 43 below.

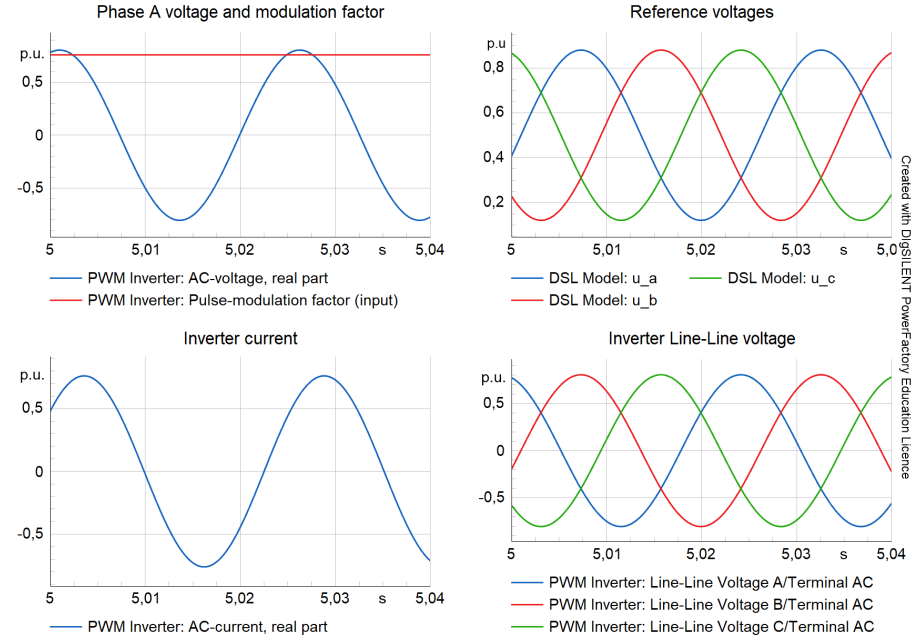

Figure 43: Inverter voltage, current, and reference voltages at 50% load and 39.6 Hz.

The inverter parameters for 50% load indicate that the output voltage remains clean and sinusoidal. The period is longer and it yields a frequency of about 39,6 Hz which is expected. The voltage amplitude appears consistent with the modulation index, indicating effective voltage regulation even at 50% load. The current magnitude is reduced as expected due to the lower load. It retains a smooth sinusoidal form, again confirming proper functioning of open loop V/f control strategy at half load. The reference signals are well-balanced, phase-shifted by 120°, and follow the reduced frequency setting closely. Following the inverter parameters, the three-phase magnetizing flux waveforms for the step-up and step-down transformers under 50% load conditions are shown in Figure 44.

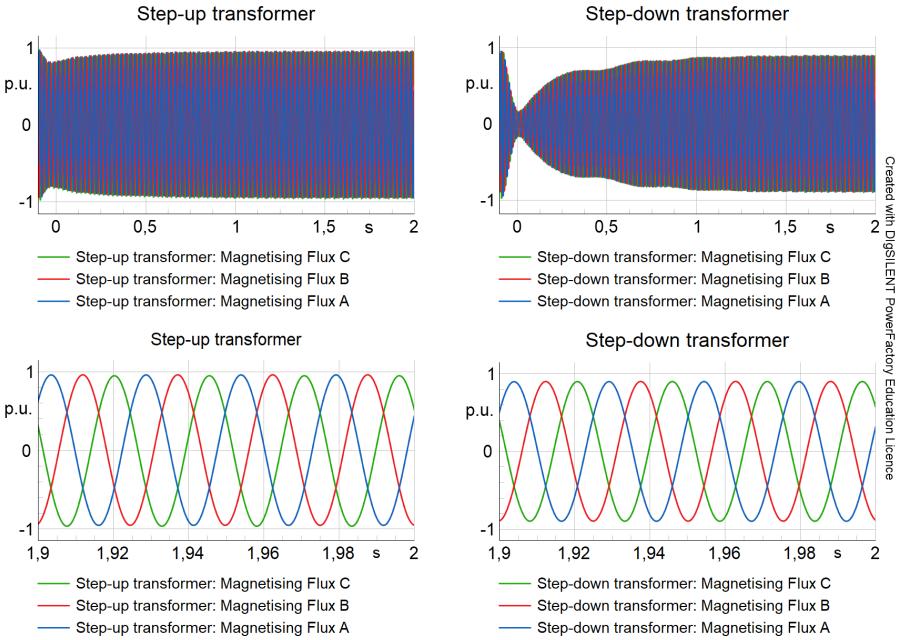

Figure 44: Magnetizing flux of step-up and step-down transformers under 50% load operation

Similar to the 75% load case, at t = 0 the flux oscillates. Furthermore, a slight reduction in flux amplitude in steady state is visible for the step-down transformer compared to the 100% load and 75% load cases. The magnetic flux amplitude still adheres closely to the expected 1 p.u. amplitude, indicating that that the V/f ratio has been maintained. Lastly, the cable parameters are shown in subplots in Figure 45 below.

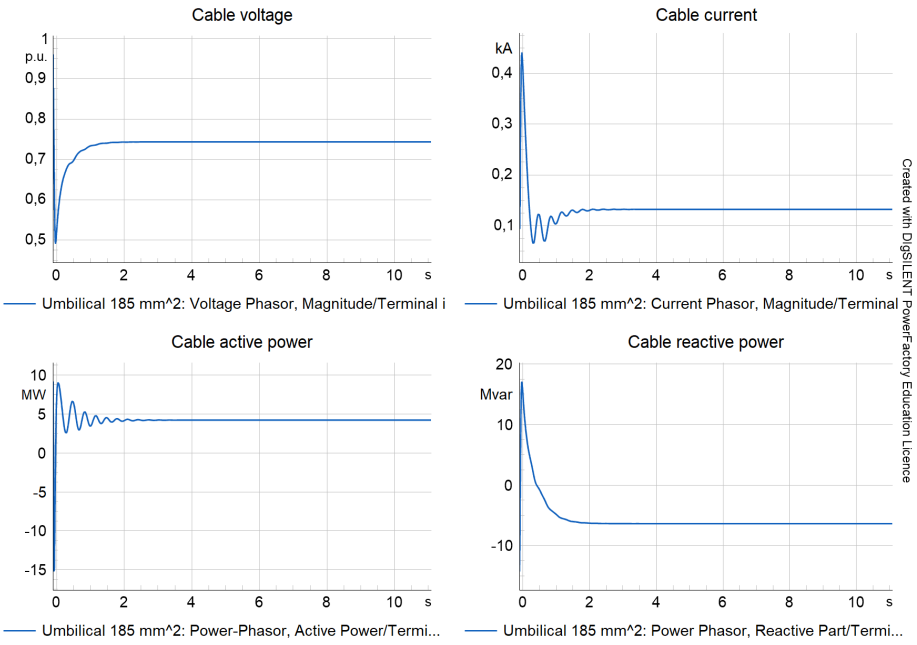

Figure 45: Cable voltage, current, and power results at 50% load

The voltage in Figure 45 ramps up and settles around 0.75 p.u. after two seconds, closely matching the 0.76 p.u. from the load flow results in Table 16. The current stabilizes near 0.132 kA, relatively consistent with the 0.140 kA cable input current. Active power settles around 4.5 MW, aligning well with the 4.437 MW load flow value. Reactive power also exhibits a transient peak before stabilizing around 7 MVAr, which matches the 6.976 MVAr in the load flow, confirming accurate modeling of the steady-state behavior.

4.3.4 Dynamic Response of the System to a Frequency Reduction

To evaluate the dynamic behavior of the system under open-loop V/f control, a frequency step was introduced, similar to the one in Section 4.2. At t = 2.5 s, the frequency was reduced from 50 Hz to 45.4 Hz. This test also served to assess the performance of the dynamic models during a dynamic frequency change. The corresponding system response is illustrated in Figure 46.

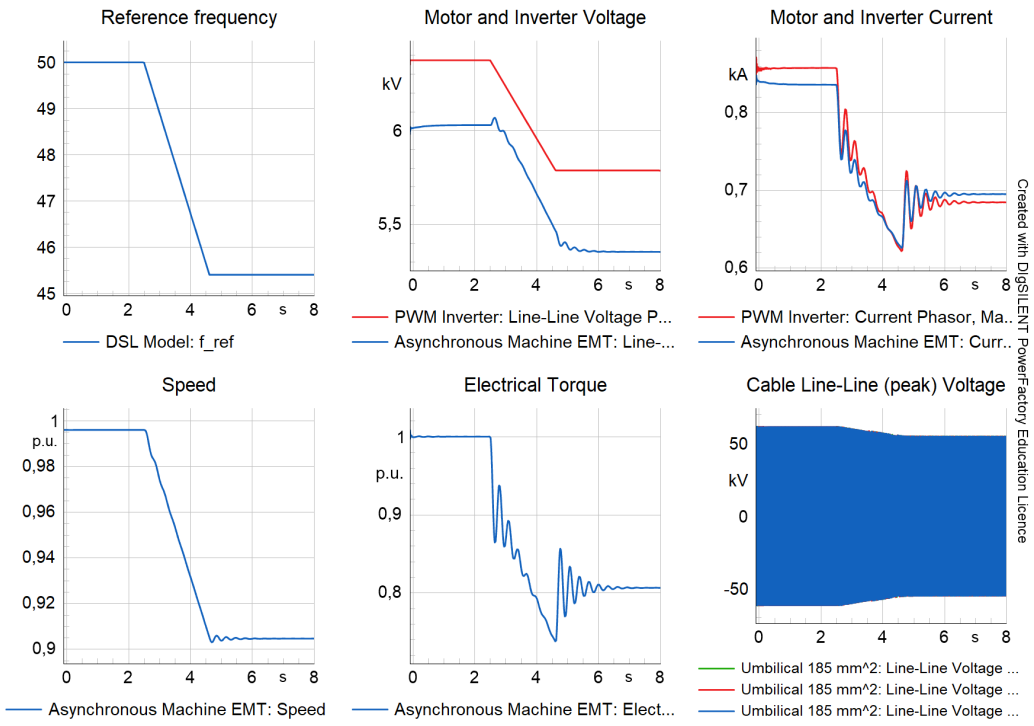

Figure 46: System response to frequency change from 50 to 45,4 Hz

As shown in the figure, the system responded as expected. Following the frequency reduction at t = 2.5 s, both torque and speed decreased, eventually stabilizing around the steady-state values: approximately 0.9046 p.u. for speed and 0.8066 p.u. for torque. Oscillations in the torque are visible, likely caused by the lack of damping in the open-loop control strategy.

Despite these oscillations, the inverter and motor currents remain within their rated limits. Notably, the motor current exceeds the inverter current after the frequency step, which may be attributed to the reduced power demand of the motor and the increased influence of the cable's capacitive effect. Lastly, the line-to-line peak voltage at the motor terminal stays within the specified voltage limits throughout the event.

Similarly, the frequency step 50 to 39.6 Hz was also tested and the results can be seen in below Figure

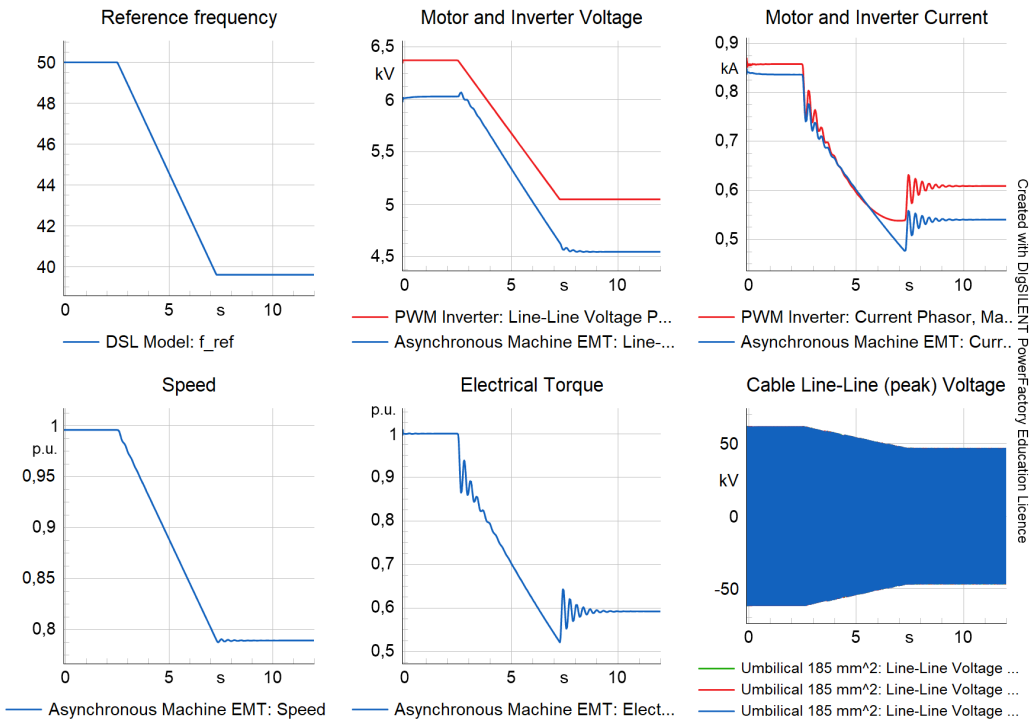

Figure 47: System response to frequency change from 50 to 39.6 Hz

As expected, the speed reduces to around 0.79 p.u. and torque settles around 0.6 p.u. aligning with the previous simulations. The values are within rated limits and there are still visible oscillations due to the lack of damping. Overall, the system behaves as expected when decreasing the frequency from 50 to 39.6 Hz.

4.4 SPWM simulations

To test the SPWM model in PowerFactory, the inverter input is connected to a DC source terminal, while the output is connected directly to the induction machine terminal, as shown in Figure 22. This setup is used because PowerFactory does not provide a dedicated RL load element. Therefore, to observe the inverter's performance under realistic operating conditions, it is connected directly to the motor and the used inverter parameters are as follows.

Table 19: Inverter parameters used for SPWM simulation in PowerFactory

Two-level SPWM DC-voltage	V_{dc}	10000	V
Voltage reference	V_{ref}	6000	V
Amplitude modulation index	m_a	0.98	
Switching frequency	f_{sw}	2000	Hz
Fundamental frequency	f_0	50	Hz
Frequency modulation index	m_f	40	

4.4.1 PWM Inverter testing

The two-level inverter uses the detailed model in PowerFactory. The value of 10 kV V_{dc} was chosen to get the amplitude modulation index as close as possible to 1 without reaching overmodulation.

The switching frequency was set to 2 kHz, a value chosen to balance performance and efficiency. The simulation test results for the inverter testing is shown below.

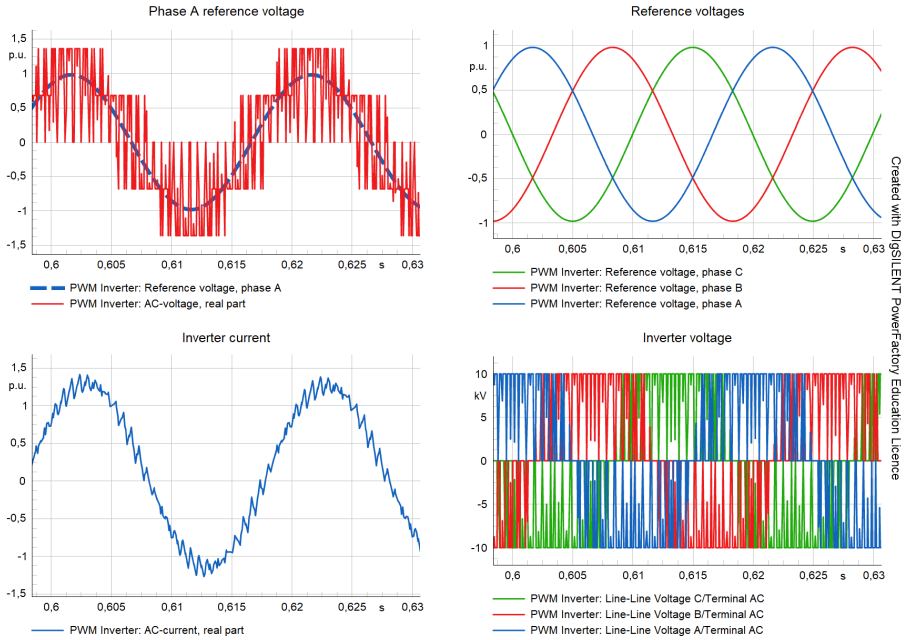

Figure 48: PWM inverter reference voltages, output voltages, and current

Figure 48 presents PWM inverter behavior during steady-state operation. The top-right plot shows the reference voltages for all three phases, each remaining within ±1 p.u. spaced 120° apart, consistent with the balanced three-phase operation. The top-left plot focuses on one phase, where the blue curve represents the reference voltage and the red curve shows the real part of the AC output voltage. Noticeable ripple is present due to the high frequency switching, while still following the reference voltage. The inverter line voltage in the bottom-right plot switches between ±10 kV, corresponding to the DC input voltage. The inverter current in the bottom left appears mostly sinusoidal with apparent ripples. Figure 49 below shows the PWM inverter's performance across all three phases, where the top plots shows the sinusoidal phase voltage and the line-line voltage and the bottom plots shows the phase currents.

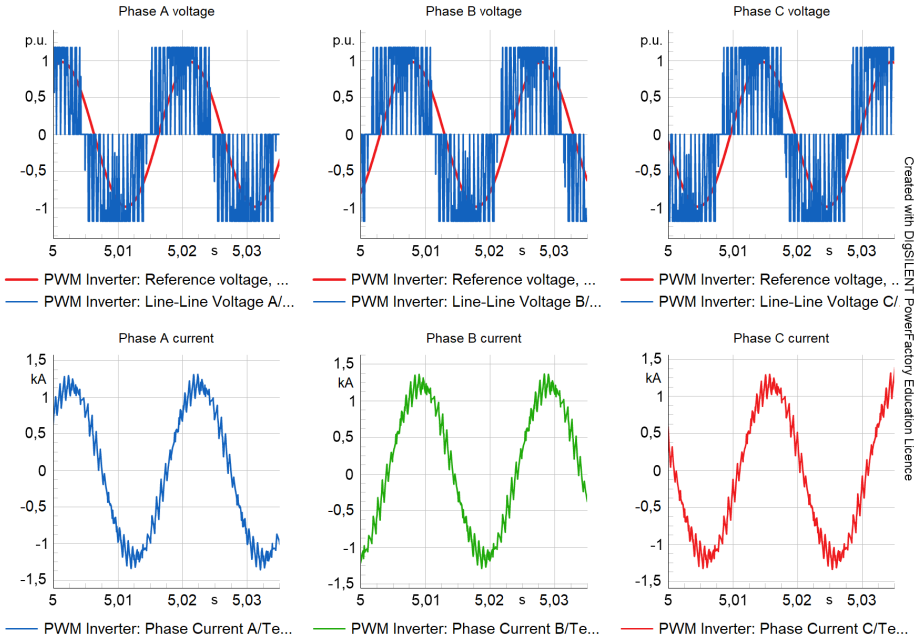

Figure 49: PWM inverter voltages and output currents for phases A, B, and C showing balanced and sinusoidal output behavior

The top row displays the line-to-line voltages compared to the respective sinusoidal phase reference voltages. The sharp PWM switching behavior is evident, and the line-line voltage signals are highly modulated. There's approximately 30° phase shift between the line-line voltage signals and the phase reference signals for all three phases. The bottom row plots illustrate the output currents for phases A, B, and C where each current waveform has quite a lot of ripple but the shape is sinusoidal and relatively clean. Minor ripples are visible due to switching effects but are within reasonable limits.

4.4.2 PWM Inverter full system

The next step of the simulation evaluates the PWM inverter integrated within the entire power system. The setup is similar to Figure 30 where the VSD is represented with a DC voltage source and the PWM inverter. Figure 50 shows the PWM inverter's output voltages and phase currents.

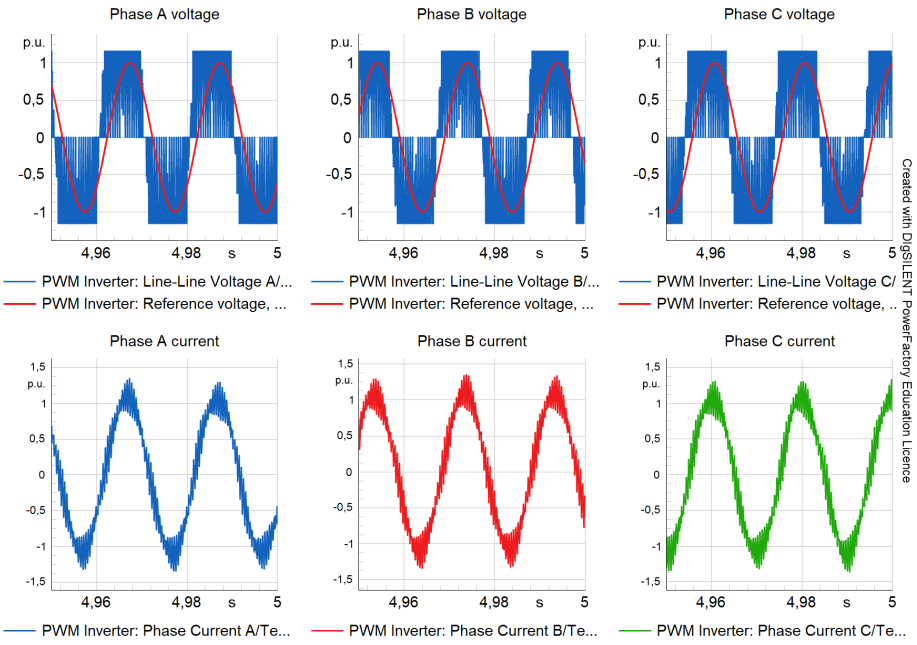

Figure 50: PWM inverter output voltages and phase currents showing balanced, sinusoidal performance

The line-line voltages follow the sinusoidal references with a 30° phase shift, all within ±1 p.u. The phase currents in the bottom row follow a sinusoidal shape and also contains ripple that goes above 1 p.u. The ripple has increased compared to the testing of the PWM inverter. However, the phase shift remains 120°. Otherwise performance is still similar to the testing of the PWM switching.

Furthermore, to asses how the cable behaves when implementing the PWM inverter, the voltage, current, active power and reactive power at the cable input and output is plotted in Figure 51 below.

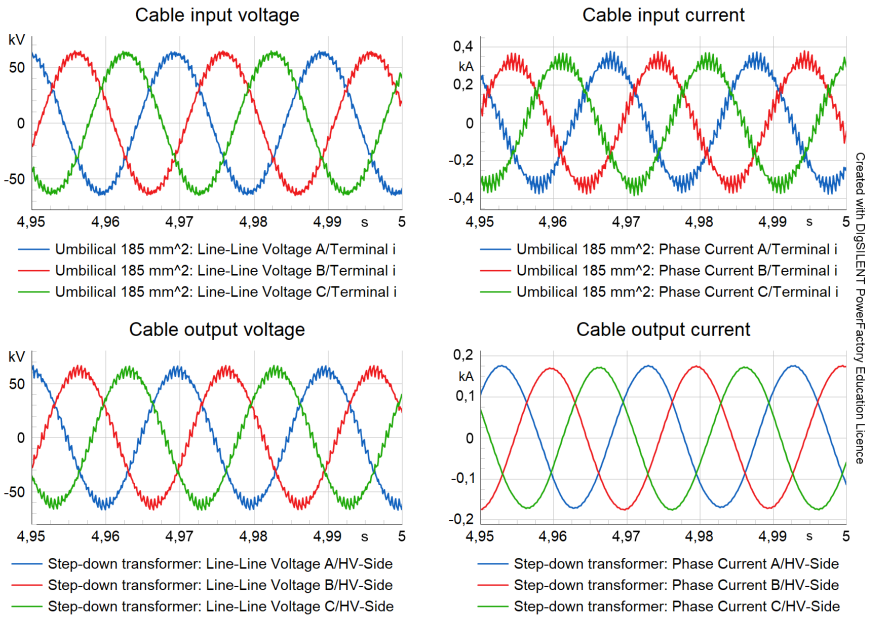

Figure 51: Cable input and output voltage and current

The voltage plot shows the system's peak line-line voltage level for one phase, which shows approximately 62 kV. The corresponding RMS line-line voltage is 43.8 kV which is within the rated operating values. The input phase current waveforms also display sinusoidal waveforms, still showing some ripple. However, the ripple in the cable's output current has been significantly reduced, resulting in waveforms that are almost perfectly sinusoidal. In contrast, the output voltage still maintains a similar level of ripple as the input, although its amplitude is slightly lower. Moreover, below Figure 52 shows how the magnetic flux of the transformers behave when the PWM switching is implemented.

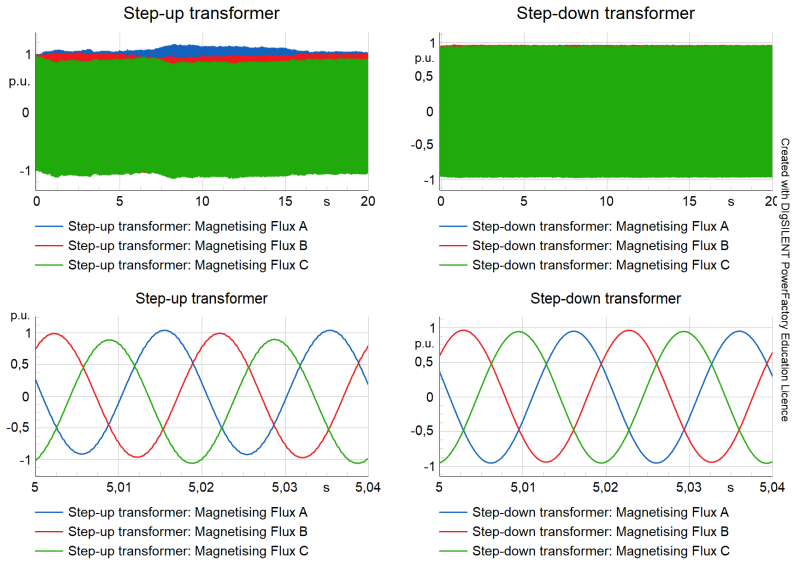

Figure 52: Magnetizing flux waveforms of step-up and step-down transformers under full-load conditions

The step-up transformer shows a less uniform waveform compared to the step-down transformer. The magnetic flux for the different phases have an offset which is not desired. However, it could possibly be due to flux initialization. Moreover, the phase shift between the phases remain 120°. In contrast, the step-down transformer maintains the magnetizing fluxes consistently within ±1 p.u. The bottom-right plot confirms the sinusoidal and symmetrical waveforms across all three phases for the step-down transformer with less ripple compared to the step-up transformer. Lastly, the motor voltage and current was evaluated and the results are shown in below Figure 53 where the top plot shows the motor peak current and he bottom plot shows the motor line-line peak voltage.

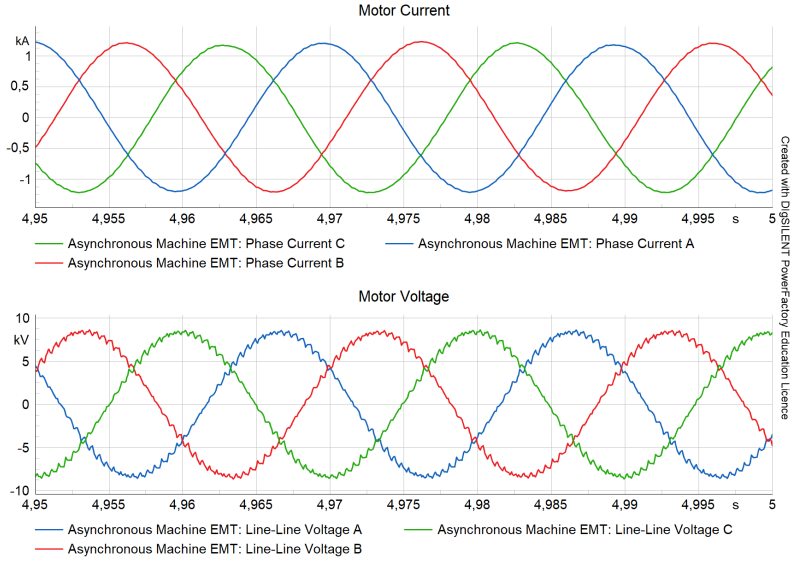

Figure 53: Motor voltages and currents confirming balanced operation and clean waveform delivery

The peak phase currents remain balanced and almost purely sinusoidal with 120° degree phase shift. Showing that the ripple from the PWM switching has almost been completely removed. The line-to-line peak voltages are also symmetrical and maintain a steady waveform, while exhibiting the expected peak amplitude and frequency. However, some ripple is still visible in the waveforms. The peak values from the plot shows 1.186 kA and 8.724 kV which corresponds to 0.826 kA and 6.168 kV as RMS line-line values, which are relatively close to the rated values of the motor but still exceeding them.

5 Discussion

This section discusses the main findings from the modeling, simulation, and analysis of the subsea drive system. Key aspects such as transmission system sizing, motor parameter estimation, control strategy performance, and the system's dynamic behavior are examined. The results are evaluated in the context of both steady-state load flow and dynamic EMT simulations, with additional focus on inverter performance, resonance effects, and overall system stability.

5.1 Transmission System Sizing

The use of the PQ-load was relevant in early stages of the modeling process to establish the baseline for the system's steady-state performance before connecting the VSD and the motor. By representing the motor as fixed active and reactive power load, it simplified the analysis and enabled straightforward load flow calculations. This approach was particularly useful for preliminary sizing of major components such as the transformers, cables and shunt reactor. For example, it allowed quick estimations of voltage drops, current levels, and required reactive compensation under full load conditions. However, because the PQ-load is not dynamic, it could not represent the time-dependent behavior of the motor during dynamic simulations. As a result, it was later replaced by a detailed motor model to more accurately simulate current waveforms, torque response, and inverter interaction under different loading conditions.

Without proper sizing of the major components, several unwanted issues could have arisen, including voltage instability, overheating, increased reactive power demand and poor dynamic responses. Undersized cables or transformers would cause excessive voltage drops, which in return could lead to under-voltage at the motor terminal. This can reduce motor torque and overall efficiency. Components that are too small may also carry more current than their thermal rating allows, resulting in overheating, insulation degradation, and reduced lifespan. As a result this can trigger protection systems or cause irreversible damage. Incorrect sizing could also lead to an imbalance in reactive power, potentially destabilizing voltage levels. Lastly, overestimation of components leads to increased unnecessary costs.

5.2 Induction Machine Parameters

The equivalent circuit parameters for the induction machine were important for the time-domain simulations because they directly affect the accuracy of the results at different load points. Most of the estimated parameters worked well for the rated variables when using the equivalent circuit. However, the starting torque showed a noticeable deviation. This might be due to errors in the calculation or inaccuracies in the estimated reactances. It could also be linked to the assumptions made during the estimation process, which naturally affects accuracy. Ideally, the equivalent circuit wouldn't be the first choice for validating the parameters, but since the actual parameters weren't available, it had to be done this way.

Normally, equivalent circuit parameters are determined during the design of the motor or through no-load and locked rotor tests. In this case, estimation was the only option because the technical specifications didn't provide the necessary information, and the physical motor wasn't accessible. For instance, the NEMA rating had to be assumed, and it was estimated that the current decreases linearly with shaft power. These are just approximations that impact all the equivalent circuit parameters. Even with that, most of the calculated values ended up being quite close to the expected ratings, with only minor deviations.

One good way to validate the parameters was by plotting the torque-speed curve of the motor. The main issue was the low starting torque, which led to that the electrical torque couldn't overcome the load torque after a certain point, causing the motor to stall, as seen in Figure 18. As a result, the motor wouldn't start properly unless the load torque was lowered, which wouldn't match the rated

conditions. The motor's high inertia made it even harder to start without enough torque. Still, the estimated parameters was deemed good enough for steady-state analysis at different loads. This is due to that steady-state simulations don't require the motor to overcome the load torque, and the starting torque does not affect those results.

5.3 Load Flow

The load flow results provided valuable insights into the performance of the system under steady state conditions for different cable sizes, before testing the system under varying operating points. One notable parameter that wasn't included in the datasheet was the AC resistance. Although typical AC resistance values are available in many datasheets, they did not match the specific dimensions of the cables in this study. Therefore, the AC resistance was estimated based on the actual cable dimensions to improve accuracy. Larger cables exhibited a more pronounced Ferranti effect, with noticeable voltage rise at the receiving end of the cable as shown in Figure 25. As mentioned earlier, this is due to the increased cable capacitance, which results in higher charging currents and a higher reactive power injection along the cable. As a result, the reactive power demand at the motor terminal decreases, lowering the required voltage output from the VSD to maintain nominal voltage.

Power factor varied noticeably between the different cable sizes. As reactive power increases, the power factor tends to decrease because the proportion of active power relative to apparent power is reduced. This is influenced by lower resistive losses and changes in reactive demand at the receiving end. In the case of the 300 mm^2 cable, the reactive effects became excessive, which negatively impacted system stability.

Figures 25 and 26 illustrates the Ferranti effect clearly, where larger cables result in lower current due to reduced resistance and voltage drops are less severe. However, the 300 mm^2 cable showed signs of high reactive power generation and voltage rise, leading to reduced operational stability. Overall the results are consistent with theoretical expectations and either of the cables except for the 300 mm^2 could be used for this application.

The frequency for each operating point was manually adjusted to reflect the conditions for 75% and 50% load, since the reactance of the cable and transformers depends on frequency. This was done by changing the nominal frequency settings within the components, which may have introduced some error and could have been the wrong approach. However, this method may introduce some inaccuracies, as it does not fully capture how the voltage is regulated by the VSD at the sending end, nor how voltage drops across the step-up transformer, transmission cable, and step-down transformer affect the motor terminal voltage. In a true V/f control scenario, the VSD adjusts both voltage and frequency proportionally, but due to impedance in the transmission path, the motor may receive a slightly lower voltage than intended. This could result in deviations from the ideal V/f ratio at the motor terminals. Despite this, the majority of the results aligned with expectations and remained within rated limits. Notably, both active power and current decreased as the load was reduced, confirming that the system responded appropriately to the adjusted operating points.

5.4 V/f control performance

The open-loop V/f control strategy implemented in the system functioned as intended, achieving the desired voltage and frequency adjustments when the input frequency of the DSL model was modified. This was reflected in the corresponding changes to the motor's speed and torque, demonstrating that the open-loop control correctly followed the predefined V/f ratio. The primary objective of this control method was to reach specific operating points where the motor's torque-speed characteristic intersects with the load torque curve, as illustrated in Figure 19. However, it is important to consider the potential impact of parameter estimation errors in components such as transformers and cables. A small percentage error (below 10%) in impedance values could cause discrepancies in the actual

voltage seen at the motor terminals due to inaccurate modeling of voltage drops. This would distort the effective V/f ratio at the motor, potentially resulting in torque mismatches, inefficient operation, or failure to reach the intended operating point. In practical applications, such deviations are typically corrected using feedback mechanisms or fine-tuning strategies. For open-loop control, one common mitigation approach is adjusting the frequency or voltage setpoint slightly based on measured motor performance, or even performing offline tuning based on real system response. This objective was achieved successfully after the parameter event step was triggered, indicating that the V/f control was capable of accurately setting the desired operating conditions.

However, during the frequency step change, oscillations were observed in the torque response. This behavior is typical for open-loop control since there is no feedback to compensate for sudden changes. In closed-loop V/f control, these oscillations would typically be mitigated by real-time adjustments based on feedback signals from the motor. In contrast, the open-loop setup simply follows the predefined V/f curve, leading to transient overshoots when the frequency is adjusted. However, due to practical reasons, it is difficult to implement closed-loop control for subsea systems with step-outs as long as 150 km because of maintenance and the long signal traveling distance.

The absence of a damping function in the control strategy further contributed to these oscillations. A damping mechanism would have allowed for a smoother transition by reducing overshoot and settling time. Implementing such a feature in future iterations could enhance system stability during oscillations. Despite this, the system eventually stabilized at the expected values for speed and torque, confirming that the open-loop V/f strategy is capable of reaching target operating points relatively quickly even with its limitations. Overall, while the open-loop V/f control method was sufficient for achieving steady-state operation at the intended points, it needs further development for dynamic operation.

5.5 EMT

The EMT simulations at 100%, 75% and 50% load levels showed system behavior that was mostly in line with expectations. The motor consistently reached steady-state operation, and the speed, torque, voltage and current values matched the calculated load-flow targets fairly well. The simulations also confirmed that the system responded appropriately under each load condition.

Some minor oscillations in voltage, current, torque and power were observed during the start of the simulations and frequency changes. These are likely due to PowerFactory initializing the model at the beginning of each simulation and carrying over previous results. Despite this, the deviations are short and do not significantly affect overall system performance. The system remained stable across all load conditions and frequencies. The motor's dynamic model responded as expected to frequency changes at different loads, confirming that the VSD setup works as expected. While minor improvements could enhance accuracy, the results are sufficient to validate the model for further use.

At 50% load, the step-down transformer shows noticeably lower magnetic flux during initialization, as seen in Figure 44. This is most likely due to the initial oscillations in voltage, since it directly influences the magnetic flux.

The load flow results and the EMT simulations demonstrated a high degree of congruence as displayed in sections 4.1 and 4.3. This indicates that the steady-state approximations provided by load flow analyses closely matched the dynamic behavior captured in EMT simulations. These similarities indicate that the load flow approach effectively captured the overall system performance under steady-state conditions and the V/f control works as expected.

5.6 SPWM

The SPWM results from the PowerFactory simulation showed that the PWM inverter operated as expected. The switching patterns closely followed the reference control signals from the DSL model, resulting in reasonably good current waveforms. However, during the full system tests, there was noticeable ripple, especially in the inverter's output current. This ripple also influenced the step-up transformer's magnetic flux, as seen in Figure 52, where the flux is offset. This imbalance is likely due to the LV side of the step-up transformer being connected directly to the inverter output, exposing it to the raw PWM voltage. Since the inverter generates high switching noise, it can create sharp spikes in the flux waveform. This could lead to saturation in the transformer due to imbalance between the phases. This could be improved by adding a multilevel inverter like a five or six-level, reducing the harmonics. Moreover, an LC filter could be added at the inverter's output. This would smooth out the high-frequency components and reduce the ripple before the voltage reaches the transformer. Although, in real life systems, the step-up transformer can be directly connected to the inverter.

The step-down transformer, on the other hand, displayed much more uniform magnetic flux waveforms. This is likely due to the cable acting as a low-pass filter. The cable's distributed inductance and capacitance naturally attenuate high-frequency harmonics as the signal propagates over the 150 km length. This filtering effect results in smoother current reaching the step-down transformer.

At the motor input, the voltage was measured at 6.168 kV, which is slightly higher than the expected 6 kV. While part of this deviation may stem from the lack of damping and high-frequency switching harmonics introduced by the PWM inverter, the voltage at the VSD frequency also appears slightly elevated. This could result from imperfect modeling of the system impedance and reactive power compensation. The elevated voltage also causes the RMS line current to be lower than expected, at 826 A. In a real-life system, the skin effect in the cable would result in better harmonic damping due to increased cable resistance at higher frequencies.

6 Conclusions and Future Work

6.1 Conclusions

The thesis presented the design and optimization of a subsea drive system configured for long step-out power transmission, with a primary focus on voltage stability, power delivery, and steady-state performance. A comprehensive model of a 150 km distributed parameter cable was developed to accurately simulate voltage drops and charging currents. The results from load flow analyses and EMT simulations demonstrated that the transmission system effectively delivered the required voltage and power to the subsea induction motor. This also ensured maintaining operational limits of the system components during steady-state conditions. The study highlighted the critical importance of proper cable sizing and reactive power compensation in preserving voltage stability across long transmission distances. Among the four cable sizes analyzed, the two smaller cables exhibited a voltage drop across the cable, which is preferable to the voltage rise seen in the larger cables. Between the two smaller cables, the 185 mm^2 cable offered the best balance between voltage profile, reactive power draw, and active losses.

An open-loop V/f control strategy was implemented for regulating the speed of the induction motor. The control method successfully achieved the desired operating points of the motor, validating its effectiveness for long-distance transmission. However, transient oscillations were observed during frequency steps due to the lack of real-time feedback. The addition of a damping mechanism or filters is recommended to improve stability and reduce overshoot during such transitions.

The effects of SPWM inverter switching on the system was also examined. While the inverter successfully generated sinusoidal current waveforms, the directly connected step-up transformer exhibited significant flux imbalance and phase ripple. These effects could possibly be linked to the switching noise introduced by the switching operation. In contrast, the step-down transformer displayed much smoother flux waveforms, a result of the low-pass filtering effect provided by the long subsea cable, which attenuated high-frequency harmonics before they reached the transformer. To mitigate flux imbalances and reduce harmonic content, the implementation of an LC filter at the inverter output can be used, which could enhance the stability of the power transmission. A five or six level inverter could also be implemented to reduce harmonics.

Overall, the findings confirm the feasibility of long step-out subsea power transmission in steady state using open-loop V/f control, provided that proper filtering and reactive power compensation are implemented to address voltage stability and harmonics. These measures are essential to ensure reliable motor operation, maintain voltage stability, and protect system components in real-world applications. The insights gained are particularly applicable to offshore oil and gas operations and emerging deep-sea renewable energy systems. While some simplifications were made in the modeling process, the results offer a solid foundation for further refinement and real-world implementation. Ultimately, this thesis contributes to advancing the design of robust subsea electrical systems capable of supporting the growing demands of remote underwater applications.

6.2 Future Development

One potential area for future work is the implementation of a V/f ramp in the control system to improve the motor start-up process. This would involve gradually increasing the voltage and frequency during start-up to reduce inrush current and mechanical stress. To design this ramp accurately, detailed motor parameters would be needed—particularly to determine the required starting torque and corresponding starting currents at different frequencies. With this information, an appropriate voltage boost can be applied at low frequencies to ensure smooth acceleration. Additionally, the control system could be enhanced with current feedback from the VSD output, allowing it to detect and respond to motor stall conditions. This would improve reliability and make the system more robust under varying load and start-up scenarios.

Another area for future work is a more detailed investigation of harmonic distortion in the system. The use of PWM and long subsea cables introduces high-frequency components that can affect voltage quality and increase losses. To address this, harmonic analysis could be performed to identify dominant frequencies and evaluate their impact on system performance. Based on these findings, appropriate filtering solutions, such as passive LC filters, could be implemented to reduce distortion and protect sensitive equipment like transformers and motors.

Another possible direction for future work is to explore the use of a motor with higher rated frequency and its impact on system stability over long transmission distances. Higher operating frequencies increases motor speed and improves power density. Investigating how a high-frequency motor interacts with long cables would help determine if additional compensation or filtering is needed to maintain stable and efficient operation.

6.3 Ethics

The thesis aims to minimize energy consumption and improve efficiency of long step-out subsea drive systems, aligning with efforts to reduce environmental impact. Cautions were taken in order to not cause 'greenwashing' or promoting the oil and gas industry as greener and more environmentally friendly than it actually is.

Another key consideration is the environmental impact of installing large subsea equipment such as transformers, cables, and pumps. These installations can disturb seafloor habitats and pose risks to marine life, including noise pollution that may interfere with species reliant on sound for navigation and communication. To mitigate these effects, the project emphasizes compact, efficient system designs that reduce the physical footprint of subsea infrastructure. Additionally, it encourages the use of installation methods and technologies that minimize noise and ecological disruption.

References

[1] S. Demmig, J. Andrews, and R.-D. Klug, "Control of subsea motors on multi-km cable lengths by variable frequency drives," in *Petroleum and Chemical Industry Conference Europe Electrical and Instrumentation Applications*, 2011, pp. 1–10.

[2] Nexans, "Subsea interconnection: High-performance subsea power transmission solutions," https://www.nexans.com/markets/activities/markets/power-transmission/subsea-interconnection/, 2025, accessed: 2025-01-21.

[3] ABB, "Subsea electrical solutions: Driving energy to greater depths," https://library.e.abb.com/public/17cf838a05f8c24c852575590078d7a1/brochure_SubseaElec_final.pdf, 2025, accessed: 2025-01-21.

[4] T. R. Brinner, R. H. McCoy, and T. Kopecky, "Induction versus permanent-magnet motors for electric submersible pump field and laboratory comparisons," *IEEE Transactions on Industry Applications*, vol. 50, no. 1, pp. 174–181, 2014.

[5] F. Mahmouditabar, A. Vahedi, and N. Takorabet, "Robust design of bldc motor considering driving cycle," *IEEE Transactions on Transportation Electrification*, vol. 10, no. 1, pp. 1414–1424, 2024.

[6] A. Leonard, "Network and complex systems overview of losses and solutions in power transmission lines," 10 2020.

[7] A. L. Sheldrake, *Handbook of Electrical Engineering: For Practitioners in the Oil, Gas and Petrochemical Industry*. John Wiley & Sons, Ltd, 2003. [Online]. Available: https://onlinelibrary.wiley.com/doi/book/10.1002/0470013893

[8] S. Lundberg, "Enm076 electric drive systems, lecture 7 and 8," Lecture, Dept. of Electrical Engineering, Chalmers University of Technology, Gothenburg, Sweden, 2025, jan. 24, 2024.

[9] A. C. Md. Inoon Nishat, "Implementation of discretized vector control strategies for induction machines," Master's thesis, Chalmers University of Technology, Gothenburg, Sweden, September 2012, published Master's Thesis.

[10] W. Zhou, Y. Wang, and Z. Chen, "Impedance-based modelling method for length-scalable long transmission cable for stability analysis of grid-connected inverter," in *2018 IEEE 4th Southern Power Electronics Conference (SPEC)*, 2018, pp. 1–8.

[11] J. Faiz and S. M. B. Islam, "A review on transformer losses," *Energy Reports*, vol. 7, no. 1, pp. 1049–1069, 2021. [Online]. Available: https://ietresearch.onlinelibrary.wiley.com/doi/full/10.1049/elp2.70009

[12] A. J. Pansini, *Electrical Transformers and Power Equipment*. Lilburn, GA: The Fairmont Press, Inc., 2005.

[13] Voltech International Ltd., "Transformer basics," https://www.voltech.com/support/technical-articles/transformer-basics/, n.d., accessed: 2025-05-13.

[14] T. Worzyk, *Submarine Power Cables: Design, Installation, Repair, Environmental Aspects*,

1st ed., ser. Power Systems. Springer Berlin, Heidelberg, 2009. [Online]. Available: https://link.springer.com/book/10.1007/978-3-642-01270-9

[15] C. Altin, *Comparative Analysis of Transmission Line Models Across Varying Lengths: A Comprehensive Study on Relative Comparison in Terms of Current, Voltage, Power, Loss, Regulation and Efficiency*, 07 2024, pp. 51–63.

[16] Ansys, "Transmission line theory," Online, 2020, accessed: Feb. 19, 2025. [Online]. Available: https://innovationspace.ansys.com/courses/wp-content/uploads/sites/5/2020/06/TransmissionLineTheory.pdf

[17] S. Klyapovskiy, "Subsea motor drives with long subsea cable," *NTNU Open*, 2014, master's thesis, Norwegian University of Science and Technology. [Online]. Available: https://ntnuopen.ntnu.no/ntnu-xmlui/handle/11250/258007

[18] T. Instruments, *Sensorless Field Oriented Control of 3-Phase Induction Motors*, March 2013, accessed: 2025-02-11. [Online]. Available: https://www.ti.com/lit/an/sprabq8/sprabq8.pdf

[19] M. Vijayakumar and R. Manikandan, "An efficient bidirectional sensorless induction motor drive using slip estimation," *International Journal of Engineering Research & Technology*, vol. 3, no. 1, pp. 1136–1140, 2014. [Online]. Available: https://www.ijert.org/research/an-efficient-bidirectional-sensorless-induction-motor-drive-using-slip-estimation-IJERTV3IS10446.pdf

[20] E. Monmasson, Ed., *Power Electronic Converters: PWM Strategies and Current Control Techniques*, 1st ed. Hoboken, NJ, USA: John Wiley & Sons, 2011, [Online]. Available: https://ebookcentral.proquest.com/lib/chalmers/detail.action?docID=1143638&query=power%2520electronic%2520converters.

[21] ABB, "Abb drives - technical guide book," 2016, accessed: 2025-03-02. [Online]. Available: https://search.abb.com/Library/Download.aspx?DocumentID=3AFE64514482&DocumentPartId=1&

[22] P. T. Finlayson, "Output filters for pwm drives with induction motors," *IEEE Industry Applications Magazine*, vol. 4, no. 1, pp. 46–52, 1998.

[23] K. Ahmed, S. Finney, and B. Williams, "Passive filter design for three-phase inverter interfacing in distributed generation," in *2007 Compatibility in Power Electronics*. Gdansk, Poland: IEEE, May 2007, pp. 1–8. [Online]. Available: https://ieeexplore.ieee.org/document/4296511

[24] J. Tang, "Control of a subsea pmsm with a very long feeding cable using a top-side converter – design and performance evaluation," Master of Science Thesis, Chalmers University of Technology, Gothenburg, Sweden, 2016.

[25] N. Mohan, T. M. Undeland, and W. P. Robbins, *Switch-Mode dc-ac Inverters: dc-sinusoidal ac*. John Wiley & Sons, Inc., 2003, pp. 200–248.

[26] T. Foqha, S. Alsadi, S. S. Refaat, and K. Abdulmawjood, "Experimental validation of a mitigation method of ferranti effect in transmission line," *IEEE Access*, vol. 11, pp. 15 877–15 886, 2023. [Online]. Available: https://uhra.herts.ac.uk/bitstream/handle/2299/26820/Experimental_Validation_of_a_Mitigation_Method_of_Ferranti_Effect_in_Transmission_Line.pdf?sequence=1

[27] A. Singh and R. Ahuja, "Reactive power compensation in power systems," *IEEE Transactions on Power Delivery*, vol. 34, no. 2, pp. 456–468, 2019.

[28] X. Zhao, Y. Wang, and J. Liu, "Voltage stability of long-distance offshore power transmission systems," *Electric Power Systems Research*, vol. 196, p. 107223, 2021.

[29] N. G. Hingorani and L. Gyugyi, *Understanding FACTS: Concepts and Technology of Flexible AC Transmission Systems*. IEEE Press, 2000.

[30] P. R. Pajic, D'Aquila, "Variable shunt reactors with on-load tap-changers for the efficient compensation of over-voltages caused by capacitive loads," *e-CIGRÉ Publications*, 2015. [Online]. Available: https://www.e-cigre.org/publications/detail/ish2015-20-variable-shunt-reactors-with-on-load-tap-changers-for-the-efficient-compensation-of-over-voltages-cau html

[31] DIgSILENT GmbH. (2021) Powerfactory - power system analysis software. Accessed: 2025-03-25. [Online]. Available: https://www.digsilent.de/en/powerfactory.html

[32] F. Gonzalez-Longatt and J. Rueda, *PowerFactory Applications for Power System Analysis*, 01 2015.

[33] U.S. Department of Energy, "Technical support document: Energy efficiency program for consumer products and commercial and industrial equipment: Distribution transformers," U.S. Department of Energy, Technical Support Document, 2012, accessed: 2025-04-07. [Online]. Available: https://www1.eere.energy.gov/buildings/appliance_standards/pdfs/dt_nopr_tsd_complete.pdf

[34] G. M. Vecchione, M. M. C. Merlin, M. S. S. Ravera, and M. M. M. Sforna, "Shunt reactor compensation for subsea cables in industrial plants," in *2022 IEEE Industry Applications Society Annual Meeting (IAS)*, 2022, pp. 1–8. [Online]. Available: https://ieeexplore.ieee.org/document/10321639

[35] ABB, "High voltage engineered induction motors technical catalog," PDF document, available from ABB, 2025, accessed: 2025-03-31. [Online]. Available: https://search.abb.com/library/Download.aspx?DocumentID=9AKK103508&DocumentRevisionId=M

[36] J. Silva and R. Oliveira, "Estimation of three-phase induction motor equivalent circuit parameters from manufacturer catalog data," *Journal of Microwaves, Optoelectronics and Electromagnetic Applications*, vol. 16, no. 1, pp. 73–85, 2017. [Online]. Available: https://www.scielo.br/j/jmoea/a/8w93K5PpcgjYtvx76djjXjq/?lang=en

[37] M. H. Haque, "Estimation of three-phase induction motor equivalent circuit parameters," *Electric Power Systems Research*, vol. 26, no. 3, pp. 187–193, 1993. [Online]. Available: https://doi.org/10.1016/0378-7796(93)90012-4

[38] Y. Zhang and X. Wang, "Optimization and improvement of ac resistance calculation method considering skin and proximity effects," *Energy Reports*, vol. 7, pp. 1901–1909, 2021.

[39] ABB, "Xlpe submarine cable systems," PDF document, available from ABB, 2023, accessed: 2025-03-31. [Online]. Available: https://new.abb.com/docs/default-source/ewea-doc/xlpe-submarine-cable-systems-2gm5007.pdf

Department of Electrical Power Engineering
CHALMERS UNIVERSITY OF TECHNOLOGY
Gothenburg, Sweden
www.chalmers.se

CHALMERS
UNIVERSITY OF TECHNOLOGY